ABSTRACT

Title of Document: STUDY OF SOLITON SPACE CHARGE WAVES IN INTENSE ELECTRON BEAMS

Yichao Mo, Doctor of Philosophy, 2013

Directed By: Professor Rami Alfred Kishek
Professor Patrick Gerald O'Shea
Department of Electrical and Computer Engineering

High brightness electron beams have wide applications in accelerator-driven light sources, X-ray, free-electron lasers (FELs), spallation neutron sources and intense proton drivers. Advanced accelerators demand superior beam quality for such intense beams, where the non-linear space charge force will introduce collective effects and limit the maximum beam current and quality. Near the cathode, all beams of interest begin as space-charge dominated beams. Density fluctuations can naturally occur and lead to space charge waves. Therefore, it is crucial to understand and control how these beam modulations develop in an intense beam.

This dissertation addresses the longitudinal beam dynamics of large-amplitude perturbations on electron beams. I report on the first systematic characterization of solitons in electron beams. Solitons are localized persistent waves that behave like particles, preserving their properties (shape, velocity, etc.) over long distances and through collisions with other solitons. They have practical applications and are of

interest to many disciplines such as condensed matter physics, plasma physics, beam physics, optics, biology and medicine. Whereas solitons in electron beams have been predicted on theoretical grounds decades ago in the form of longitudinal space charge waves, they were never experimentally observed until recently in the University of Maryland Electron Ring (UMER).

By introducing a pulsed laser beam on a thermionic cathode, an electron beam with a narrow density perturbation from photoemission is generated. The perturbation then evolves into longitudinal space charge waves that propagate along the beam. For large-amplitude initial perturbations, a soliton wave train is observed. The soliton's properties are confirmed experimentally. The results are compared with cold fluid model in theory and the WARP particle-in-cell (PIC) code in simulation. Reasonable agreement is achieved.

This reproducible nonlinear process provides an alternative for a tunable, coherent radiation sources without wigglers/undulators. The soliton pulse spacing is therefore investigated, which is found dependent on the pipe radius (g-factor) and beam plasma frequency.

STUDY OF SOLITON SPACE CHARGE WAVES IN INTENSE ELECTRON BEAMS

By

Yichao Mo

Dissertation submitted to the Faculty of the Graduate School of the
University of Maryland, College Park, in partial fulfillment
of the requirements for the degree of
Doctor of Philosophy
2013

Advisory Committee:
Professor Rami A. Kishek, Co-Chair
Professor Patrick G. O'Shea, Co-Chair
Professor Ed Ott
Professor Thomas Antonsen
Professor James Drake, Dean's representative

Dedication

To my beloved family, Fengfei Mo, Guolian Zhu and Kai-Wen Wang.

.

Acknowledgements

I am grateful to my advisors Professor Rami Kishek and Patrick O'Shea for their guidance and financial support of my study. Prof. O'Shea recruited me into the UMER group, inspired me to work hard in accelerator physics and to develop entrepreneurship and leadership skills. Prof. Kishek is a great mentor, helped me on almost every aspect of doing research, from theoretical study, simulation work, to presentation and writing skills, and the direct assistance on the revision of this thesis.

I would like to thank the all UMER staffs. First, I am especially grateful to Dr. Donald Feldman, who involved in every step of my experimental setup and operation, not to mention the numerous helpful discussions. He also teaches me the way to live a fruitful life and treat me like a family. Dr. Irving Haber is a theoretical physicist and simulation expert. I wouldn't have worked out the simulation and theoretical derivations without his instructions and encouragement. Dr. Brian Beaudoin is extremely knowledgeable, helpful and friendly. I could always turn to him when having problems, no matter it's about experiment or theory. I thank Dr. Timothy Koeth, Dr. Santiago Bernal, Dr. Ralph Fiorito, Dave Sutter for their discussions and guidance. I'm also thankful to the UMER students Hao Zhang, Kamal Rezaei, William Stem and Kiersten Ruisard for the discussions. We share our knowledge with each other and develop ourselves into better accelerator physicists.

In addition, I would like to thank Professor Thomas Antonsen, Professor Ed Ott and Professor James Drake for serving in the examination committee. I thank R. Davidson, E. Startsev, H. Qin and I. Kaganovich from PPPL for helpful discussions. I also thank A. Friedman, D. Grote, and J. L. Vay for their support of WARP.

Last but not least, I thank my parents and girlfriend, who is always there for me during the years of hard work. I thank Prof. Fan-Yi Lin in National Tsing Hua University, who encouraged me to pursue a graduate degree in the US and explore the world. I never regret making the decision.

This work is supported by the U.S. Department of Energy Offices of High Energy Physics and Fusion Energy Sciences, and the Dept. of Defense Office of Naval Research and the Joint Technology Office.

Table of Contents

Dedication ii
Acknowledgements iii
List of Tables vii
List of Figures viii
Chapter 1: Introduction 1
1.1 Motivation 1
1.2 History and Background 2
1.2.1 Space Charge Waves 2
1.2.2 Solitons 3
1.3 Focus of Thesis 4
1.4 Organization of Thesis 5
Chapter 2: Theoretical Work on Space Charge Waves and Solitons 6
2.1 Linear Perturbation in Coasting Beams 6
2.2 Wave Dispersion and Kinetic Model 11
2.3 Korteweg-de Vries (KdV) Equation 18
2.3.1 KdV Equation Introduction 18
2.3.2. KdV Equation Derivation 20
2.4 KdV Equation Scaling 24
2.5 Summary 26
Chapter 3: Experimental Setup and Diagnostic Tools 27
3.1 The University of Maryland Electron Ring (UMER) 27
3.2 Electron Gun (Thermionic Emission) 30
3.3 Laser Setup (Photoemission) 35
3.4 Beam Modulation Methods 38
3.4.1 Induction Cell 38
3.4.2 Q-switching for Beam Slicing 41
3.4.3 DMD Mirrors for Transverse Beam Distribution Modification 43
3.5 Beam Diagnostics 45
3.6 Summary 47
Chapter 4: Experimental Observation and Characterization of Solitons 48
4.1 Single Large-Amplitude Initial Perturbation 48
4.2 Data Analysis for Soliton Properties 51
4.3 KdV Model Prediction and Comparison with Experiments 54
4.4 Soliton Dependence on Beam Parameters 61
4.5 Soliton Interactions and Two-Perturbation Experiments 63
4.6 Improved Beam Injection and Steering Solution 66
4.7 Solitons from Velocity Perturbation 69
4.8 Summary 72
Chapter 5: Simulation of Soliton Formation and Spacing 73

5.1 Soliton Simulation and Comparison with Experiments 73
5.2. Soliton Propagation in Same Direction 84
5.3 Study of Soliton Pulse Spacing 87
5.3.1 Dependence on Pipe Radius 88
5.3.2 Dependence on Plasma Frequency 91
5.4 Summary 93
Chapter 6: Conclusion and Future Plans 94
6.1 Summary 94
6.2 Future Plans 95
Appendix A: Laser Alignment Procedure 97
Appendix B: Matlab Code for Heater Voltage Feedback Control 98
Appendix C: Matlab Code for Integrating KdV Equation 101
Appendix D: WARP Code for Soliton Simulation 104
Bibliography 111

List of Tables

Table 2.1 Symbols and quantities used in 1-D cold fluid model. ……...4

Table 3.1: Beam Parameters of UMER…….……..29

Table 3.2: Aperture Radius and Exiting Beam Current, Emittance…….…….....29

Table 3.3 Beam current decreases with time……...32

Table 3.4 Cathode heater voltage vs temperature……34

Table 3.5: Nd:YAG Laser Parameters…….37

Table 3.6: Key features of DMD Discovery 1100……...44

Table 4.1: Compare experimental results with KdV model for the 5th and 7th turn..49

Table 5.1 Variable sensitivity to beam dynamics in WARP……...83

List of Figures

Figure 2.1: The dispersion relation for a linear space charge waves……...…6

Figure 2.2: Illustration of how the nonlinear perturbation leads to beam steepening. 10

Figure 2.3: A long electron beam bunch model for axial electric field calculation. ...11

Figure 2.4: A short electron beam bunch model for axial electric field calculation. ..12

Figure 2.5: The dispersion and steepening effects of a wave……..…16

Figure 2.6: The dispersion relation for space charge waves at various perturbation levels……18

Figure 2.7: A numerical example of KdV Integration of an initial profile……..20

Figure 3.1: UMER layout. …….…….28

Figure 3.2: Photograph of the aperture wheel for beam selection...……28

Figure 3.3: Simplified schematic of UMER gun for thermionic emission. ...……30

Figure 3.4: Beam current vs heater voltage for the UMER gun (80mA aperture). …31

Figure 3.5: Diagram for cathode heater voltage feedback design……..…….33

Figure 3.6: Cathode temperature as a function of heater voltage……35

Figure 3.7: Experimental setup of beam perturbation by photoemission. ……..36

Figure 3.8: Temporal profile of the 355nm laser for photoemission. …….……37

Figure 3.9: Pulse widening by combination of two pulses with a time delay….....38

Figure 3.10 : Equivalent RLC circuit of the glass gap……...……..39

Figure 3.11: The glass gap structure of the induction cell……...……39

Figure 3.12: Induction cell voltage versus time…….…….…….40

Figure 3.13: The density perturbation fast/slow wave pair induced by a velocity perturbation using induction cell…….40

Figure 3.14: Phase dynamics of the focusing/defocusing electric field……..41

Figure 3.15: The pulse focusing effect by a saturable absorber……..42

Figure 3.16: The updated laser perturbation experimental setup with Q-switch…….43

Figure 3.17: DMD mirrors for transverse distribution modification of a laser beam..44

Figure 3.18: Setup of pyrometer for cathode temperature measurement……..…46

Figure 3.19: An example output from the Bergoz coil for a beam with and without the perturbation…..…….47

Figure 4.1: Initial beam profile at the Bergoz, 22 mA beam with 50% perturbation..50

Figure 4.2: Turn-by-turn plot of beam propagation at wall current monitor. ……..…50

Figure 4.3: 3D Turn-by-turn plot of beam propagation at wall current monitor...…..51

Figure 4.4: Soliton width and amplitude at different turns, with 22mA 25% perturbation…….….52

Figure 4.5: Plot of solitary wave's width2 vs 1/Amplitude. ……..…….……53

Figure 4.6: Plot of soliton velocity vs Amplitude. ……..……...…….53

Figure 4.7: Beam current loss profile. ……..……...54

Figure 4.8: Beam evolution for 22mA, 25% perturbation turn by turn……..55

Figure 4.9: KdV integration results before scaling to lab parameters……..…..59

Figure 4.10: Soliton wave train comparison between experiments and theory …..…60

Figure 4.11: Soliton dependence on beam current.....……..……..…61

Figure 4.12: Soliton dependence on perturbation strength…….…62

Figure 4.13: Soliton dependence on perturbation width. ……..…63

Figure 4.14: Initial condition for one and two perturbations. ...……..64

Figure 4.15: Two soliton interaction experiment. …..…….65

Figure 4.16: The old and new data for 22 mA initial beam pulse evolution……...68

Figure 4.17: Comparison of beam loss profiles before and after beam improvement.69

Figure 4.18: Velocity soliton wave train generated by induction cell…….70

Figure 5.1: Initial beam condition measured at Bergoz and the smoothed profile for simulation. ……..…..….75

Figure 5.2: Comparison of first turn between experiment and simulation, with initial conditions from Fig.5.1. …….……75

Figure 5.3: A numerical example of how beam energy modulation affects the pulse width……..…….….77, 78, 79

Figure 5.4: Initial beam condition measured at Bergoz and the modified profile for simulation. ……...…….80

Figure 5.5: Comparison of the 1st, 2nd, 5th and 8th turns between experiment and simulation, with initial conditions from Fig.3.15…….…….81, 82

Figure 5.6: Nonlinear wave interaction process at different time instants……..……84

Figure 5.7: Simulation for two large perturbations propagating in same direction.....85

Figure 5.8: Comparison between simulations of two perturbations and one perturbation…….…….86

Figure 5.9: Comparison between simulations of two perturbations and one perturbation (overlap the two results for better comparison)…… ……..87

Figure 5.10: Comparison of two soliton wave trains with different pipe radius at 7th turn……...88

Figure 5.11: Comparison of three soliton wave trains with different pipe radius at 8th turn…….……..……89

Figure 5.12: Soliton spacing for different g-factors…….……...90

Figure 5.13: Soliton spacing frequency VS g-factor, for 6 ns and 12 ns wide perturbations at the 20^{th} turn, with 23.05m per turn…….…..….91

Fig. 5.14: Comparison of soliton wave train evolution for different plasma frequency……..…92

Fig. 5.15: Soliton pulse spacing frequency vs Plasma frequency for perturbations with 6ns and 12 ns width…….…....93

Chapter 1: Introduction

1.1 Motivation

Particle accelerators physics have traditionally focused on the high energy frontier for colliding particles, in facilities such as the Large Hadron Collider (LHC) [1], Tevatron [2], and the Stanford Linear Collider (SLC) [3]. Nowadays, there is a shift to a different type of accelerator where beam quality is important, measured by a high phase space density. Example applications are the 4th-generation light sources [4], free electron lasers [5], spallation neutron sources [6] and so on. Such high-quality beams have low emittance and high current, meaning space charge forces are dominant, especially near the source and low-energy part of the machine. Since the space charge force is generally nonlinear for a non-uniform beam distribution, it is important to understand how much it will contribute to beam quality degradation. Any beam degradation from space charge at low energy will be frozen in as the beam is accelerated to relativistic energies, which may cause emittance growth and reduce application performance. Longitudinal energy or density perturbations at low-energy will propagate as waves along the beam, and the modulations thus generated can lead to beam instabilities and microbunching [7]. Meanwhile, more instability occurs when the transport pipe is resistive [8]. Studies of space charge waves [9-10] suggest that small initial perturbations will split into two space charge waves, a slow wave and a fast wave, going opposite directions in the beam frame. When the perturbation is large, it is theoretically predicted that solitary waves, evolving according to the Korteweg-deVries (KdV) equations (see sec. 2.4), can be generated on the beam [11-12]. The nonlinear longitudinal dynamics is complex since in the experiment it encounters beam loss, beam mismatch, pulse geometry change, different transverse beam distribution and etc. The goal

is to do a thorough study on this nonlinear process by experimental approach, theoretical modeling and Particle-in-Cell code simulations.

1.2 History and Background

1.2.1 Space Charge Waves

The study of space charge waves could be traced back to Simon Ramo and W. C. Hahn in the 1930s [13-14], Birdsall and Whinnery in the 1950s [15].

At the University of Maryland, J. G. Wang and D. X. Wang [9, 16] initiated pioneering studies in which they generated controllable perturbations on an electron beam to induce space charge waves In 1990s. The perturbation was generated by modulating the cathode grid pulse of the thermionic gun. Suk [17] extended those studies to explore the effect of a resistive pipe on the wave propagation. He observed the growth of slow wave and decay of fast wave, consistent with analytical calculations. Inspired by the observation of large-amplitude waves, Suk also performed a theoretical analysis of possible solitary wave formation in electron beams, and designed and experiment to test that, but did not carry it out. Zou [18] continued resistive wall effect studies on space charge waves when the perturbation is large , which turns out not consistent with theoretical predictions. Kai [19] measured the energy profiles of longitudinal space-charge waves for the first time.

Subsequently, at the University of Maryland Electron Ring (UMER), Huo [20] demonstrated a new way of generating perturbations by combining thermionic and photoemission. The long-pulse (~100ns) main beam is produced by thermionic emission, while a short-pulse (~5ns) ultraviolet laser aimed at the cathode produces an additional population of

electrons that forms the perturbation. Harris and Neumann [21] extended the work to multiple perturbations using a beam splitter and an interferometer on the drive laser. Thangaraj [22] continued this work, studying the evolution of one or two perturbations over multiple turns around the ring, a distance of over 100 m. Towards the end of his Ph.D. research, Thangaraj experimented with large-amplitude perturbations and was the first to observe solitary waves on electron beams. Beaudoin [23] developed the induction cell in the UMER ring for generating energy perturbations, which turns out similar evolution with the space charge wave pair from density perturbations.

1.2.2 Solitons

Solitons are localized persistent waves that behave like particles, preserving their properties (shape, velocity, etc.) over long distances and through interactions and collisions with other solitons. They are of interest to many disciplines such as condensed matter physics, plasma physics, particle physics, optics, biology and medicine. First observed in water waves by John Scott Russell in Scotland in 1834 [24], the unchanged propagating wave was named "solitary wave", and was later described by the Korteweg and deVries equation in 1898. In 1965, Zabusky and Kruskal solved the KdV equation numerically and observed that the solitary waves behave like stable particles [25], naming it "soliton" afterwards. In 1970, Ikezi, Taylor and Baker observed ion-acoustic solitons in plasma experimentally [26]. Intense charge particle beams are known to have collective effects similar to plasmas [27], such as the ability to support waves. However, the beam system, a bounded nonneutral plasma, can behave in ways that differ fundamentally from an unbounded plasma. Since 1980s, solitons have been investigated in

charged particle beams, both theoretically and in simulations [11-12, 28-31]. Experiments on proton beams exhibited longitudinal single-soliton hole structures [32-35].

More recently, at the University of Maryland Electron Ring (UMER), Thangaraj [19] observed the development of a solitary wave train from large-amplitude perturbations in electron beams, and Y. C. Mo [36] continued with a systematic experimental study of the soliton wave train, with strong proof of soliton existence, as well as the soliton characteristics under varying beam parameters.

1.3 Focus of Thesis

In this thesis, we systematically study soliton wave formation and evolution in intense electron beams. We take advantage of UMER's long propagation distance, and the capability to generate pure density perturbations using the laser photoemission technique first developed by Huo [20]. Since the pioneering work by Thangaraj, several improvements have taken place, including a reduction in the amount of beam loss over multiple turns, which provides more reliable data. Whereas Thangaraj focused on a proof-of-principle experiment for soliton formation, I studied soliton evolution as a function of beam and perturbation parameters, such as beam current and width. I am also the first to perform two-soliton interaction experiment, demonstrating their particle-like behavior. I initiate the soliton pulse spacing study, which has potential applications for new radiation sources. Finally, I compare the experimental results with the KdV model and self-consistent particle-in-cell simulations to understand more about the experiment.

1.4 Organization of Thesis

The remainder of the thesis is organized as follows.

In Chapter 2, we discuss the theoretical work on space charge waves using the cold fluid model. The KdV equation and its scaling technique are derived.

In Chapter 3, we introduce the experimental setup, including the UMER gun, the drive laser and induction cell for perturbation generation, and the beam diagnostics tools.

In Chapter 4, we present the detailed experimental results and analysis, where density soliton wave trains are observed and proved. We also explored the soliton dependence on beam parameters such as beam current, perturbation and width. The experimental results are also compared with the theoretical KdV model. Velocity solitons generated by induction cell are also presented.

In Chapter 5, we perform simulations of nonlinear perturbations on electron beams with Particle-in-Cell code WARP. A good agreement with experiments is achieved. The soliton pulse spacing, which can be potentially useful for a new radiation source, is also studied by simulation with varying pipe radius and beam plasma frequency.

In Chapter 6, we conclude the work in the thesis and suggest future work that can help better understand solitons in electron beams and their potential applications.

Chapter 2: Theoretical Work on Space Charge Waves and Solitons

In this chapter, we discuss the theory of longitudinal space charge waves. In section 2.1, we discuss the perturbation theory using the cold fluid model in section 2.1. In section 2.2, we study the dispersion effect and generalized kinetic model. In section 2.3, we present a detailed derivation of the Korteweg deVries (KdV) equation from the cold fluid model. In Section 2.4, we illustrate how this KdV model scales to UMER beam parameters, assisting with the comparison between theory and experiment/simulation in the later chapters.

2.1 Linear Perturbation in Coasting Beams

This section reviews the generation of linear space charge waves by a small perturbation using the one-dimensional cold fluid model, followed by the discussion of nonlinear perturbation. The beam is assumed infinitely long in a cylindrical conducting pipe.

The Vlasov equation [12] is applied to the coasting electron beam for analyzing its evolution, where the beam has an energy distribution. To simplify the kinetic model, a cold fluid assumption is made, i.e., that the thermal velocity spread is negligible compared with the space charge wave velocity. By taking the moments of the Vlasov equations, we obtain the one-dimensional cold fluid model as follows.

Continuity equation: $\frac{\partial \lambda}{\partial t} + \frac{\partial (\lambda v)}{\partial z} = 0$ (2.1)

Momentum equation: $\frac{\partial v}{\partial t} + v\frac{\partial v}{\partial t} = \frac{qE_z}{\gamma_0^3 m}$ (2.2)

We can linearize the continuity and momentum equations under the assumption that the perturbation amplitude is small compared to the unperturbed beam current. The symbols used are shown in Table 2.1.

Table 2.1 Symbols and quantities used in 1-D cold fluid model.

Symbol	Quantity
λ	Line charge density (C/m)
t	Time (s)
v	Velocity (m/s)
z	Distance (m)
q	Charge of an electron (-1.6 x10^{-19} C)
m	Electron mass (9.1 x10^{-31} kg)
Ez	Longitudinal electric field (V/m)
β	Ratio of velocity to the speed of light
γ	Lorentz factor, $\gamma = 1/\sqrt{1-\beta^2}$

The linearization by writing λ, v and I as the sum of a constant and small perturbation quantities, be expanded using the Fourier transform. Thus,

$$\lambda = \lambda_0 + \lambda_1 e^{i(\omega t - kz)}$$

$$v = v_0 + v_1 e^{i(\omega t - kz)} \tag{2.3}$$

$$I = I_0 + I_1 e^{i(\omega t - kz)} = \lambda_0 v_0 + \left(\lambda_0 v_1 + \lambda_1 v_0\right) e^{i(\omega t - kz)}$$

Where the subscript 0 represents the unperturbed beam, and subscript 1 is the small perturbation term that varies with time and space.

Plug (2.3) into the cold fluid equations, use the axial electric field approximation [11] in the long wavelength limit, when the perturbation wavelength is much bigger than the pipe radius.

$$Ez \approx -\frac{g}{4\pi\varepsilon_0\gamma_0^2}\frac{\partial\lambda}{\partial z} \tag{2.4}$$

After the linearization and ignoring the high order terms (a more generalized derivation could be referred to sec. 2.2), we obtain the dispersion relation:

$$\left(w - kv_0\right)^2 - c_s^2k^2 = 0 \tag{2.5}$$

With C_s defined as the longitudinal wave velocity, which is the phase velocity of the wave moving within the beam frame: $C_s = \sqrt{\frac{qg\lambda_0}{4\pi\varepsilon_0\gamma_0^5 m}}$ (2.6)

Where g is the geometry factor [37], $g = \alpha + 2\ln\frac{b}{a}$ (2.7)

b and a are the wall radius and beam radius, respectively. α is the correction term, when the beam is space charge dominated, α=0; when the beam is emittance dominated, α=1/2. It is constant only in the long wavelength limit. A thorough discussion on the g-factor is presented in section 2.3.

From the dispersion relation in eqn (2.5), we obtain the phase velocity of the space charge wave in the lab frame, which is $\frac{\omega}{k} = v_0 \pm c_s$ (2.8)

Therefore, under the linear perturbation theory and long wavelength limit, the group velocity $v_g = \frac{\partial w}{\partial k}$ is independent of frequency [Fig. 2.1], in other words, the wave is propagating

in a non-dispersive medium and the shape of perturbation is preserved.

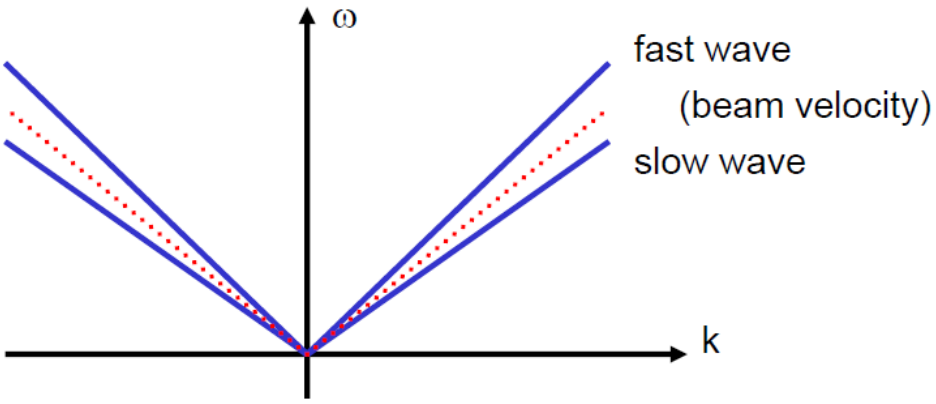

Figure 2.1: The dispersion relation for a linear space charge waves.

The analytical solution for the perturbed line charge density, velocity and beam current are shown as follows:

$$\lambda_1(z,t) = \mp \left[\qquad \mp \qquad \right] \left(t - \frac{z}{v_0 \mp} \right) \tag{2.9}$$

$$v_1(z,t) = \frac{v_0}{2} \left[\delta \mp \qquad \right] p\left(t - \frac{z}{v_0 \mp} \right) \tag{2.10}$$

$$I_1(z,t) = \mp \left[\qquad \mp \qquad \right] p\left(t - \frac{z}{v_0 \mp} \right) \tag{2.11}$$

Where $\delta = \dfrac{v_1(z=0,t=0^+)}{v}$ is the velocity perturbation, and $\eta = \dfrac{\lambda_1(z=0,t=0^+)}{\lambda_0}$ is the density perturbation. The perturbation profile is normalized as $p\left(t - \dfrac{z}{v_0 \mp} \right)$. A few immediate conclusions could be drawn from Eqn. (2.9-2.11): the perturbation splits into a fast wave and slow wave, with half of the initial perturbation amplitude; a pure density perturbation (or

velocity perturbation), i.e., σ=0 (or η=0) could significantly simplify the analytical process, which is realized in the experimental setup; From Eqn. (2.10), with a pure density perturbation ($\sigma = 0$), we get $\frac{v_1}{c_s} \propto \eta$, i.e., the phase velocity depends on the perturbation level. Therefore, a nonlinear density perturbation leads to varying phase velocity and causes beam steepening.

A numerical nonlinear analysis from the inviscid Burgers Equation [22], where no dispersion effect is counted, is shown in Fig. 2.2. It illustrates how the apex of the wave overtakes the base of the wave and leads to steepening at various times during the propagation (A, B and C). When the pulse narrows down to the scale of the pipe radius, it involves the beam dispersion and will be discussed in section 2.2.

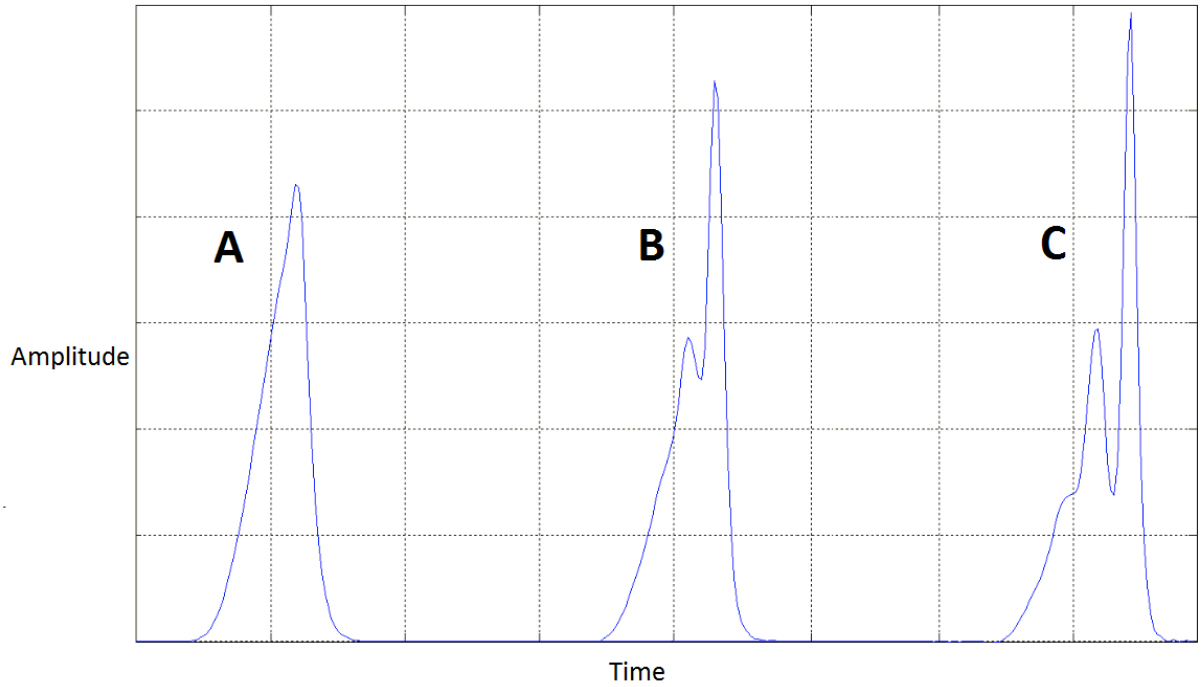

Figure 2.2: Illustration of how the nonlinear perturbation leads to beam steepening.

2.2 Wave Dispersion and Kinetic Model

From the previous section, we observe the nonlinear steepening effect which makes the initial perturbation break into a couple of narrower pulses. The beam dispersion, an effect that widens the pulse as it propagates, becomes non-negligible when the pulse width is comparable to the pipe radius [11]. The dispersion could balance the nonlinear steepening at a certain point and maintain the pulse shape, eventually leading to soliton formation. In this section, we will discuss the wave dispersion from the modified axial electric field E_z and generalized g-factor kinetic model.

In the long wavelength limit, the overall beam bunch is much longer than the conducting pipe radius. In this case, the self-electric field from space charge is proportional to the derivative of line charge density [Eqn. 2.3] and wave dispersion is negligible.

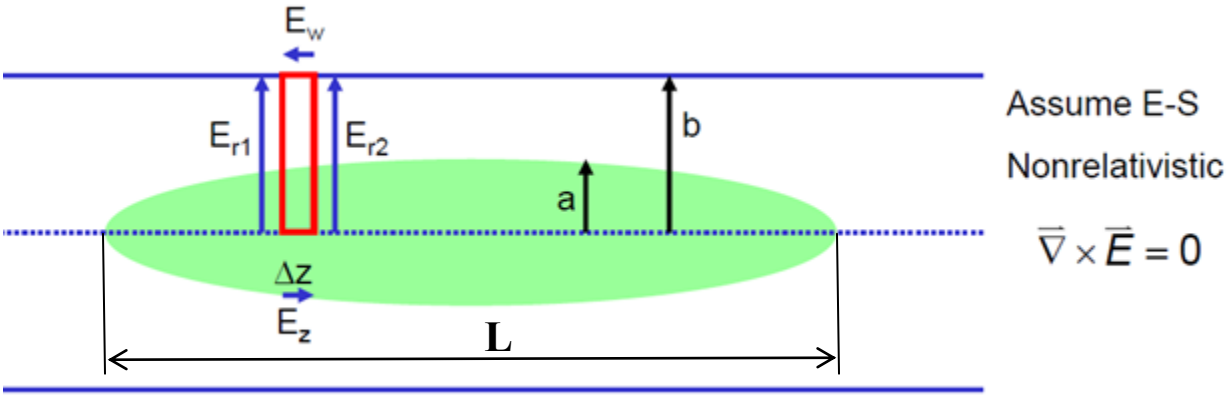

Figure 2.3: A long electron beam bunch (L>>b) model for axial electric field calculation. It is assumed to be nonrelativistic and electrostatic (E-S).

From Gauss's theorem: $E_r = \dfrac{\lambda}{2\pi\varepsilon_0 r}$ (outside the beam) (2.12)

Apply Stokes' theorem: ○ $\Delta z + \int_0^b E_{r2}dr + E_w\Delta z + \int_b^0 E_{r1}dr$

$$E_z \approx -E_w + \frac{1}{\Delta z}\int_a^b (E_{r1} - E_{r2})dr = 0 + \frac{(\lambda_1 - \lambda_2)}{(\Delta z)2\pi\varepsilon_0}\ln\left(\frac{b}{a}\right) = -\frac{\partial\lambda}{\partial z}\left(\frac{1}{4\pi\varepsilon_0}\right)2\ln\left(\frac{b}{a}\right) \quad (2.13)$$

Where $2\ln\left(\frac{b}{a}\right)$ is the g-factor.

However, when the pulse width narrows down to the short wave length limit (L~b), the derivation no longer applies, because Er_1 and Er_2 will have extra longitudinal components due to the rapid change of the beam profile [Fig. 2.4]. It eventually introduces an additional term for axial E-filed, which is proportional to the 3rd derivative of the line charge density [38]. The derivation will be shown below.

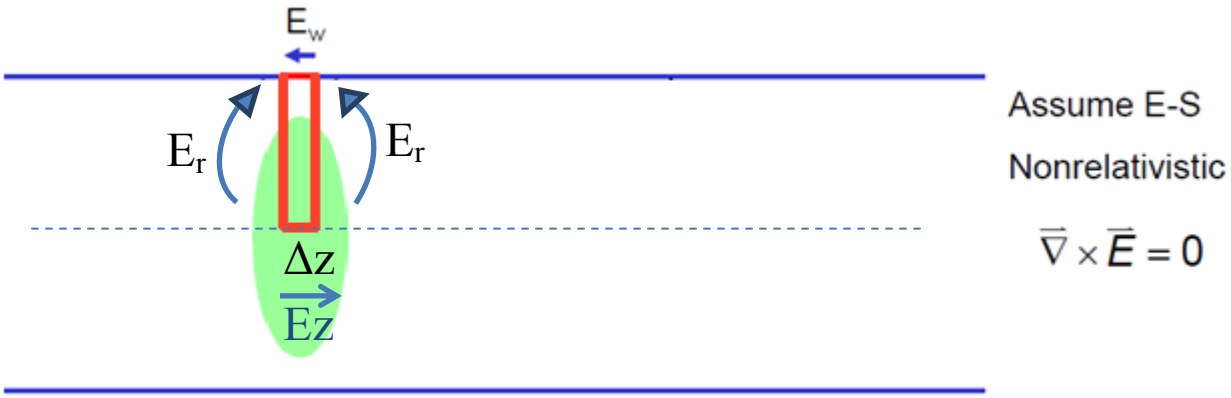

Figure 2.4: A short electron beam bunch (L~b) model for axial electric field calculation. It is also assumed to be nonrelativistic and electrostatic (E-S).

From [38], we have the final form of the nonlinear Vlasov-Maxwell equations that describe the evolution of the longitudinal distribution function $F_b\left(z,\, p_z, t\right)$ and line density $\lambda_b\left(z,\, t\right)$ as the following Eqn (2.14-2.17). Note the Gaussian units here.

$$\frac{\partial}{\partial t}F_b + v_z\frac{\partial}{\partial z}F_b + e\left\langle E_z^s\right\rangle\frac{\partial}{\partial p_z}F_b = 0 \tag{2.14}$$

$$\left\langle E_z^s\right\rangle = 2\pi\int_0^{r_w} drr\frac{n_b\left(r,z,t\right)}{\lambda_b\left(z,t\right)}E_z^s\left(r,z,t\right) \tag{2.15}$$

Where $\langle E_z^s \rangle (z,t)$ is the longitudinal average self-electric field in terms of z and t, that corresponds to a transverse spatial average of $E_z^s(r,z,t)$ weighted by the beam density profile $\frac{n_b(r,z,t)}{\lambda_b(z,t)}$. r_w is the wall radius. $n_b(r,z,t)$ is the volume particle number density, and $\lambda_b(z,t)$ is the axial line density. Therefore, the ratio $\frac{n_b(r,z,t)}{\lambda_b(z,t)}$ gives the transverse beam density distribution.

$E_z^s(r,z,t)$ is determined in terms of $n_b(r,z,t)$ by Poisson's equation. Assuming it's axisymmetric $\left(\frac{\partial}{\partial\theta}=0\right)$, it can then be expressed as

$$\frac{1}{r}\frac{\partial}{\partial r}r\frac{\partial}{\partial r}E_z^s+\frac{\partial^2}{\partial z^2}E_z^s=4\pi e\frac{\partial}{\partial z}n_b \tag{2.16}$$

The line density $\lambda_b(z,t)$ can be related to the volume density $n_b(r,z,t)$ and distribution function $F_b(z,\,p_z,t)$ as

$$\lambda_b(z,t)=2\pi\int_0^{r_w}drrn_b(r,z,t)=\int dp_zF_b(z,\,p_z,t) \tag{2.17}$$

The above set of equations (2.14-2.17) has an important feature of being applicable to general radial dependence of particle density profile. Once $n_b(r,z,t)$ is specified (which actually can be measured by a fast camera), $E_z^s(r,z,t)$ can be calculated from Eqn. (2.16). Then we can determine the average axial electric field $\langle E_z^s \rangle (z,t)$ by substituting the expression of $E_z^s(r,z,t)$ into Eqn. (2.15). Thereafter, the evolution of the longitudinal distribution function $F_b(z,\,p_z,t)$ is

also determined by Eqn. (2.14), which in turn assists the KdV equation derivation in section 2.3 (but we will simplify that case by starting from cold fluid equations).

At this point, we focus on the electric field calculation. Assuming the pipe is perfectly conducting, we then have the boundary condition $E_z^s\left(r=r_w,z,t\right)=0$. The solution to Eqn. (2.16) can be expressed as

$$E_z^s\left(r,z,t\right)=-4\pi e\int_0^{r_w}\frac{dr}{r}\int_0^r drr\left(\frac{\partial n_b}{\partial z}-\frac{1}{4\pi e}\frac{\partial^2 E_z^s}{\partial z^2}\right) \tag{2.18}$$

Solving iteratively,

$$E_z^s\left(r,z,t\right)=-4\pi e\int_0^{r_w}\frac{dr}{r}\int_0^r drr\left(\frac{\partial n_b}{\partial z}+\int_r^{r_w}\frac{dr}{r}\int_0^r drr\frac{\partial^3 n_b}{\partial z^3}\right) \tag{2.19}$$

from which we see a first derivative and a third derivative terms of particle density. The second term (3rd derivative) is small compared with the first derivative in the long wavelength limit, where $\partial/\partial z\sim L\sim k_z$ and $k_z^2r_w^2\ll$. This explains why the 3rd derivative term for the electric field is always neglected until the pulse width becomes comparable with the pipe radius.

By substituting Eqn. (2.19) into Eqn. (2.15) and doing the integration, we end up with

$$\left\langle E_z^s\right\rangle=\left\langle E_z^s\right\rangle_1+\left\langle E_z^s\right\rangle_2=-eg_0\frac{\partial\lambda}{\partial z}-eg_2r_w^2\frac{\partial^3\lambda}{\partial z^3} \tag{2.20}$$

where we have a more generalized g-factor model,

$$g_0\left(\lambda_b\right)=2\int_0^{r_w}\frac{dr}{r}\left(2\pi\int_0^r drr\frac{n_b}{\lambda_b}\right)^2 \tag{2.21}$$

$$g_2\left(\lambda_b\right)=\frac{2}{r_w^2}\int_0^{r_w}\frac{dr}{r}\left(2\pi\int_0^r drr\frac{n_b}{\lambda_b}\right)\int_0^r drr\int_r^{r_w}\frac{dr}{r}\left(2\pi\int_0^r drr\frac{n_b}{\lambda_b}\right) \tag{2.22}$$

Below is a quick example. Assuming a bell-shaped density profile,

$$n_b(r,z,t)=\frac{\lambda_b}{\pi r_b^2}(n+1)\left[1-\frac{r^2}{r_b^2}\right]^n, \qquad \text{n=0, 1, 2, …} \tag{2.23}$$

We can obtain

$$g_0(\lambda_b)=\ln\left(\frac{r_w^2}{r_b^2}\right)+\alpha_n-\frac{1}{2}\frac{R_\lambda^2}{\left[R_\lambda^4+4R_\varepsilon^4\right]^{1/2}} \tag{2.24}$$

where $\alpha_n=\sum_{m=1}^{n+1}\frac{(n+1)}{m(m+n+1)}$ (2.25)

R_λ and R_z are proportional to the space charge force and emittance force in a matched beam solution.

Therefore, with a K-V distribution (n=0), we have α=0.5. For a space charge dominated beam, $R_\lambda >> R_\varepsilon$, the final term in Eqn. (2.37) is approximated to be -0.5, which makes the g_0 factor $g_0\approx\ln\left(\frac{r_w^2}{r_b^2}\right)$; For an emittance dominated beam, $R_\lambda << R_\varepsilon$, then the final term in Eqn. (2.24) becomes 0, and the g_0 facotr $g_0\approx\ln\left(\frac{r_w^2}{r_b^2}\right)+\frac{1}{2}$. This is consistent with the simplest case we mentioned in Eqn. (2.7). Meanwhile, the g-factor is only constant in the long wavelength limit. As can be seen from Eqn. (2.24), when there is a rapid change of beam radius along the beam axis, g-factor varies accordingly.

The space charge wave tends to widen by itself when propagating due to dispersion. When the pulse narrows down, the dispersion becomes larger. This is due to the additional axial electric field term (proportional to the 3rd derivative of the line charge density) becoming non-trivially small in the short wavelength limit ($L\sim r_w$) and is directly related to the beam dispersion term in the KdV equation, as will be shown in section 2.3. Another perspective to view this is

that the frequency bandwidth increases when the pulse narrows down. Waves with different frequencies travel at different velocities in a medium. A boarder frequency domain results in a greater velocity difference between the Fourier wave components. The upper part of Fig. 2.5 [39] shows the wave dispersion effect. The pulse widens and can even split into a few sub-pulses if the wave components travel long enough at their own speeds. The balance between dispersion and nonlinear steepening effect eventually leads to solitons, which will be shown by experiments and simulations in later chapters.

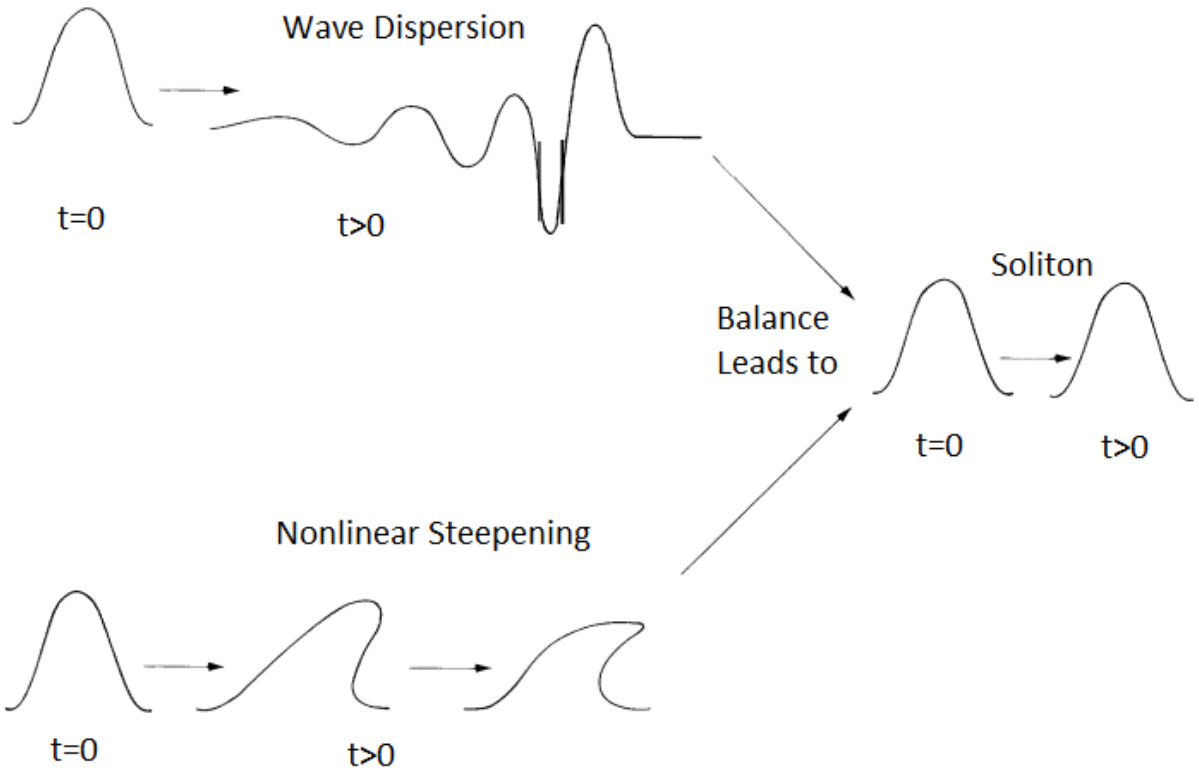

Figure 2.5: The dispersion and steepening effects of a wave, and their balance leads to solitons.

The dispersion relation can be obtained by repeating the nonlinear theory process in section 2.2 by replacing E_z in Eqn. (2.13) with

$$E_z = -\frac{c_s^2}{\lambda_0}\left(\frac{\partial \lambda}{\partial z} + \frac{g_2 r_w^2}{g_0}\frac{\partial^3 \lambda}{\partial z^3}\right) \tag{2.26}$$

which changes Eqn. (2.8) into

$$v_p = v_0 \pm c_s\sqrt{f(\eta)\bullet\left(\quad\quad\frac{r^2}{\quad}\right)} \tag{2.27}$$

Where f(η) is the nonlinear modification term on the space charge wave velocity, and

$$f(\eta) \sim \frac{\lambda_0 + \lambda_1}{\lambda_0} = 1 + \eta$$

Use the UMER setting (r_w=5mm), plot the phase velocity vs wave vector k in the beam frame for different perturbation levels [Fig. 2.6]. As can be seen in Fig. 2.6, when the perturbation density variation scale is much greater than pipe radius (rw*k<<1), the phase velocity equals sound speed Cs. When the beam perturbation narrows down (rw*k~1), the dispersion becomes non-negligible. The higher order frequency terms of the Fourier series slows down dramatically when the pulse width decreases further (rw*k<<1) in the short wavelength limit.

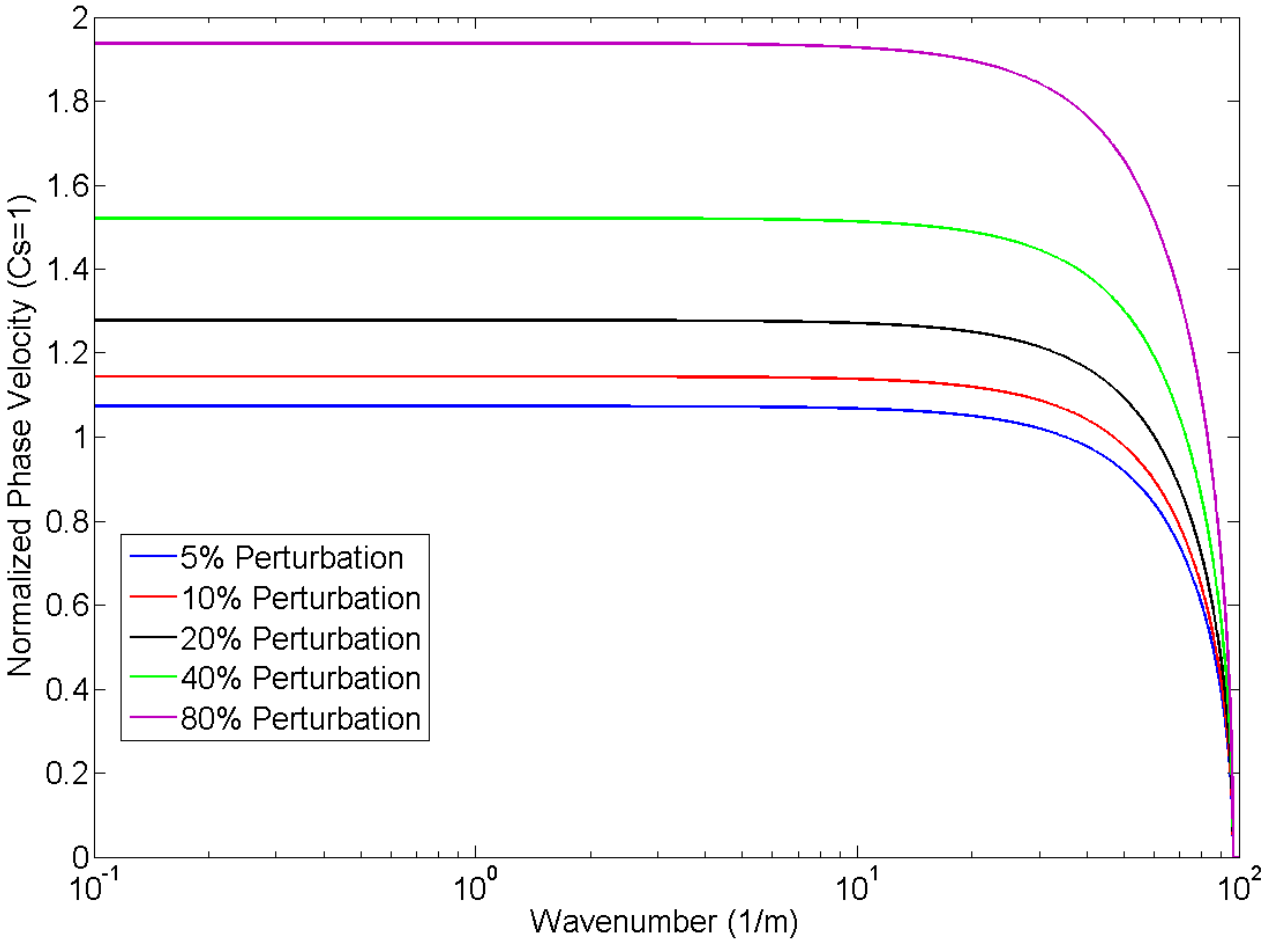

Figure 2.6: The dispersion relation for space charge waves at various perturbation levels.

2.3 Korteweg-de Vries (KdV) Equation

In this section, we first review the Korteweg-de Vries (KdV), then show the step-by-step KdV equation derivation from the cold fluid model for a coasting electron beam bunch.

2.3.1 KdV Equation Introduction

The KdV equation is a nonlinear, dispersive partial differential equation describing a function n of two variables, space z and time t.

$$\frac{\partial n}{\partial t} + n\frac{\partial n}{\partial t} + \frac{\partial^3 n}{\partial z^3} = 0 \tag{2.28}$$

where $n(z,t)$ can be the density or velocity perturbation amplitude, as a function of longitudinal distance z and propagation time t. The second term $u\frac{\partial u}{\partial z}$ represents the nonlinear effect that steepens the perturbation and results in several sub-pulses, while $\frac{\partial^3 u}{\partial z^3}$ is the dispersion term that tends to widen the pulse. The soliton results from the cancellation of these two terms. An analytical one-soliton solution is:

$$u(z,t) = \frac{c}{2} sech^2[\frac{1}{2}\sqrt{c}(z-ct)]. \tag{2.29}$$

The evolution of a known initial perturbation profile $n(z,t=0)$ can be found by integrating the KdV equation over a time period τ to obtain $n(z,t=\tau)$. A numerical example is shown in Fig. 2.7, where a soliton wave train forms from a single initial pulse. We expect similar perturbation evolution in experiments.

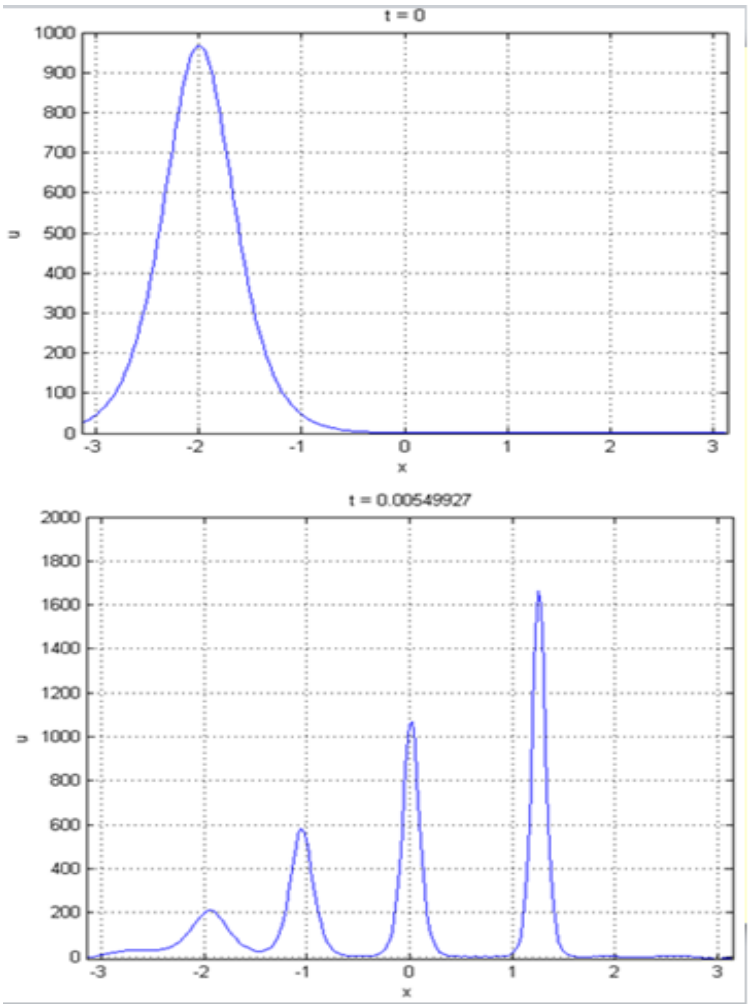

Fig. 2.7: KdV Integration of an initial profile $n(z,t=0)$ (top) from t=0 to τ =0.00549927 leads to the perturbation profile $n(z,t=\tau)$ (bottom), the units are arbitrary.

2.3.2. KdV Equation Derivation

We start from the 1-D cold fluid equations, and neglect the pressure term.

$$\frac{\partial \lambda}{\partial t}+\frac{\partial(\lambda v)}{\partial z}=0 \tag{2.30}$$

$$\frac{\partial v}{\partial t}+v\frac{\partial v}{\partial z}=-\frac{e^2 g_0}{m}\frac{\partial \lambda}{\partial z}-\frac{e^2 g_2 r_w^2}{m}\frac{\partial^3 \lambda}{\partial z^3} \tag{2.31}$$

Then introduce the constant velocities:

$$v_{b0}^2 = \frac{e^2 \lambda_0 g_0}{m} \ , \ v_{b2}^2 = \frac{e^2 \lambda_0 g_2}{m}$$

Do the normalization:

$$\eta = \frac{\lambda - \lambda_0}{\lambda_0} \ , \ U = \frac{v}{v_{b0}} \ , \ T = \frac{v_{b0}^2}{v_{b2}} \frac{t}{r_w} \ , \ Z = \frac{v_{b0}}{v_{b2}} \frac{z}{r_w}$$, where r_w is the pipe radius.

from which we have:

$$\lambda = \lambda_0 \eta + \lambda_0 \ , \ v = v_{b0} u$$

$$\frac{\partial}{\partial t} = \frac{v_{b0}^2}{v_{b2} r_w} \frac{\partial}{\partial T} \ , \ \frac{\partial}{\partial z} = \frac{v_{b0}}{v_{b2} r_w} \frac{\partial}{\partial Z} \ , \ \frac{\partial^3}{\partial z^3} = \left(\frac{v_{b0}}{v_{b2} r_w} \right)^3 \frac{\partial}{\partial Z^3}$$

Then Eqn. (2.30) and Eqn. (2.41) become:

$$\frac{\partial \eta}{\partial T} + (\eta + 1) \frac{\partial U}{\partial Z} + U \frac{\partial \eta}{\partial Z} = 0$$

$$\Rightarrow \frac{\partial \eta}{\partial T} + \frac{\partial}{\partial Z} (U + \eta U) = 0 \qquad (2.32)$$

$$\frac{\partial U}{\partial T} + U \frac{\partial U}{\partial Z} = -\frac{\partial \eta}{\partial Z} - \frac{\partial^3 \eta}{\partial Z^3}$$

$$\Rightarrow \frac{\partial U}{\partial T} + \frac{\partial}{\partial Z} \left(\eta + \frac{1}{2} U^2 + \frac{\partial^2 \eta}{\partial Z^2} \right) = 0 \qquad (2.33)$$

Then we do the coordinate transform to the wave frame, let $Z' = Z - MT$, where M is a constant normalized to sound speed v_{b0}.

Therefore, $\frac{\partial}{\partial T} = -M \frac{\partial}{\partial Z'}$ and $\frac{\partial}{\partial Z} = \frac{\partial}{\partial Z'}$

Integrate Eqn. (2.32): $-M \frac{\partial \eta}{\partial Z'} + \frac{\partial}{\partial Z'} (U + \eta U) = 0$

$$U(\eta + 1) = M\eta \ \Rightarrow \ U = \frac{M\eta}{\eta + 1} \qquad (2.34)$$

Integrate Eqn (2.33): $-M\frac{\partial U}{\partial Z'}+\frac{\partial}{\partial Z'}\left(\eta+\frac{1}{2}U^2+\frac{\partial^2}{\partial Z'^2}\eta\right)=0$

$$-MU+\eta+\frac{1}{2}U^2+\frac{\partial^2}{\partial Z'^2}\eta=0 \tag{2.35}$$

Replace U with Eqn. (2.34), then

$$-M\frac{M\eta}{\eta+1}+\eta+\frac{1}{2}\frac{M^2\eta^2}{(\eta+1)^2}+\frac{\partial^2}{\partial Z'^2}\eta=0$$

After manipulation,

$$\frac{\partial^2\eta}{\partial Z'^2}+\left[1-\frac{M^2}{\eta+1}+\frac{1}{2}\frac{M^2\eta}{(\eta+1)^2}\right]\eta=0 \tag{2.36}$$

For weakly non-linear limit, where $|\eta|\ll$, retaining terms to order η^2

$$\frac{\partial^2\eta}{\partial Z'^2}+\left(1-M^2\right)\eta+\frac{3}{2}M^2\eta^2=0 \tag{2.37}$$

Assume $\tilde{\eta}$ $M^2\eta(Z')$,

Eqn. (2.37) turns into $\frac{\partial^2\tilde{\eta}}{\partial Z'^2}$ $\left(1-M^2\right)\tilde{\eta}$ $\tilde{\eta}$ (2.38)

Eqn. (2.38) has the exact soliton solution when $M^2>1$

$\tilde{\eta}$ $-1)\sec h^2\left[\frac{1}{2}\left(M^2-1\right)^{1/2}(Z-MT)\right]$ (2.39)

Assume $\varepsilon=M-1$, then $0<\varepsilon\ll$

The argument in Eqn. (2.39) can be expressed as

$$\frac{1}{2}\left(M^2-1\right)^{1/2}(Z-MT)=\frac{1}{2}\varepsilon^{1/2}(M+1)^{1/2}\left[Z-(1+\varepsilon)T\right]\approx\frac{1}{\sqrt{2}}\left[\varepsilon^{1/2}(Z-T)-\varepsilon^{3/2}T\right]$$

Introduce $\xi = \varepsilon^{1/2}(Z - T)$, $\tau = \varepsilon^{3/2} T$

Then $\frac{\partial}{\partial Z} = \varepsilon^{1/2} \frac{\partial}{\partial \xi}$, $\frac{\partial}{\partial T} = \frac{\partial}{\partial \tau}\frac{\partial \tau}{\partial T} + \frac{\partial}{\partial \xi}\frac{\partial \xi}{\partial T} = \varepsilon^{1/2}\left(\varepsilon \frac{\partial}{\partial \tau} - \frac{\partial}{\partial \xi}\right)$

Expand Eqn. (2.32) and (2.33), according to the small nonlinearity expansions of η and U, where $\eta^{(1)}$ and $\eta^{(2)}$, $U^{(1)}$ and $U\eta^{(2)}$ are of order unity.

$\eta = 1 + \varepsilon * \eta^{(1)} + \varepsilon^2 * \eta^{(2)} + \ldots$ (2.40)

$u = \varepsilon * U^{(1)} + \varepsilon^2 * U^{(2)} + \ldots$ (2.41)

$$\Rightarrow \left(\varepsilon \frac{\partial}{\partial \tau} - \frac{\partial}{\partial \xi}\right)\left(\eta^{(1)} + \varepsilon \eta^{(2)}\right) + \frac{\partial}{\partial \xi}\left(U^{(1)} + \varepsilon U^{(2)} + \varepsilon \eta^{(1)} U^{(1)}\right) = 0 \tag{2.42}$$

$$\Rightarrow \left(\varepsilon \frac{\partial}{\partial \tau} - \frac{\partial}{\partial \xi}\right)\left(U^{(1)} + \varepsilon U^{(2)}\right) + \frac{\partial}{\partial \xi}\left(\eta^{(1)} + \varepsilon \eta^{(2)} + \frac{1}{2}\varepsilon U^{(1)^2} + \varepsilon \frac{\partial^2}{\partial \zeta^2}\eta^{(1)}\right) = 0 \tag{2.43}$$

Equate the coefficients of like powers of ε to zero,

$$\Rightarrow \frac{\partial \eta^{(1)}}{\partial \xi} = \frac{\partial U^{(1)}}{\partial \xi} = 0 \text{ , therefore, } \eta^{(1)}(\xi, \tau) = U^{(1)}(\xi, \tau) \tag{2.44}$$

In order ε, (2.42) and (2.43) become

$$\frac{\partial}{\partial \tau}\eta^{(1)} - \frac{\partial}{\partial \xi}\eta^{(2)} + \frac{\partial}{\partial \xi}\left(U^{(2)} + \eta^{(1)} U^{(1)}\right) = 0 \tag{2.45}$$

$$\frac{\partial}{\partial \tau}U^{(1)} - \frac{\partial}{\partial \xi}U^{(2)} + \frac{\partial}{\partial \xi}\left(\eta^{(2)} + \frac{1}{2}U^{(1)^2} + \frac{\partial^2}{\partial \xi^2}\eta^{(1)}\right) = 0 \tag{2.46}$$

From (2.45), we get

$$\frac{\partial}{\partial \xi}\left[U^{(2)} - \eta^{(2)}\right] = -\frac{\partial}{\partial \tau}\eta^{(1)} - \frac{\partial}{\partial \xi}\left(\eta^{(1)} U^{(1)}\right) \tag{2.47}$$

Plug (2.47) into (2.46),

$$\frac{\partial}{\partial \tau}U^{(1)} + \frac{\partial}{\partial \tau}\eta^{(1)} + \frac{\partial}{\partial \xi}\left(\eta^{(1)} U^{(1)}\right) + \frac{\partial}{\partial \xi}\left(\frac{1}{2}U^{(1)^2} + \frac{\partial^2}{\partial \xi^2}\eta^{(1)}\right) = 0 \tag{2.48}$$

Use (2.44) to replace $U^{(1)}$ with $\eta^{(1)}$,

$$\Rightarrow\ 2\frac{\partial}{\partial\tau}\eta^{(1)}+2\eta^{(1)}\frac{\partial}{\partial\xi}\eta^{(1)}+\eta^{(1)}\frac{\partial}{\partial\xi}\eta^{(1)}+\frac{\partial^3}{\partial\xi^3}\eta^{(1)}=0$$

$$\text{i.e.,}\ \frac{\partial}{\partial\tau}\eta^{(1)}+\frac{3}{2}\eta^{(1)}\frac{\partial}{\partial\xi}\eta^{(1)}+\frac{1}{2}\frac{\partial^3}{\partial\xi^3}\eta^{(1)}=0 \tag{2.49}$$

Eqn. (2.49) is the exact KdV equation. The cubic dispersive term can be traced back to the $\frac{\partial^3\lambda_b}{\partial z^3}$ term in Eqn. (2.31). Eqn. (2.49) could be solved by the inverse scattering techniques [40]. The solitons have the solution form of Eqn. (2.39), which illustrates that the velocity is proportional to the amplitude, and inversely proportional to the pulse width square. Utilizing this derivation process, we are able to get the relation between the nonlinear steepening effect and dispersive effect quantitatively (coefficients). Note that the assumption of a conducting pipe plays an important role for simplifying the derivation, otherwise the resistive wall effect [8] needs to be considered and an additional term (beam attenuation or amplification) will be added to Eqn. (2.49).

2.4 KdV Equation Scaling

When predicting the beam evolution from the KdV equation, we need to normalize the variables to the experimental settings such as the beam current, sound speed, pulse width, and etc. These characters may vary for different beam facilities and experiments. Therefore, it is important to know how the scaling affects the coefficients of the terms in the KdV equation.

Start with Eqn. (2.28): $\frac{\partial n}{\partial t}+n\frac{\partial n}{\partial z}+\frac{\partial^3 n}{\partial z^3}=0$

where n is the line charge density, t is time, x is the propagation distance in the beam frame.

Do the scaling as below:

$$z = a * \hat{z};\ t = b * \hat{t};\ n = c * \hat{n} \tag{2.50}$$

where x, t and n are the variables in the Matlab code [Appendix C] for KdV integration, while $\hat{z}$, $\hat{t}$ and $\hat{n}$ are normalized variables in lab.

Replace the n, t, and z in the KdV equation by the new variables:

$$\frac{c}{b} * \frac{\partial \hat{}}{\partial \hat{t}} \quad u \qquad \hat{z} \quad u \quad \hat{z} \tag{2.51}$$

Multiply b/c on both sides:

$$\frac{\partial \hat{}}{\partial \hat{t}} \quad u \qquad \hat{z} \quad u \quad \hat{z}$$

After further manipulation, we get:

$$- \frac{\partial \hat{}}{\partial \hat{t}} \left(\frac{}{a^3} \right) \qquad t^2 c * \hat{n} \quad \frac{}{\partial \hat{z}} \quad \hat{z} \tag{2.52}$$

Therefore, as long as we keep $a^2 c = 1$ and $\frac{b}{a^3} = 0$, Eqn. (2.52) has the same beam form as Eqn. (2.28). In other words, the beam profile n(z, t) from the simulation at time t and location z will be the same with the one in lab at time $\hat{t}$ and location $\hat{z}$. This scaling method simplifies the beam evolution prediction and will be applied in later chapters.

2.5 Summary

In this chapter, we went through the longitudinal space charge wave theory, both the linear and nonlinear cases using the cold fluid model. We explored the phase velocity dependence on the perturbation level and obtained an explicit expression. We expanded the theoretical work to a more generalized case using the kinetic model. The dispersive effect originates from the 3rd derivative term of line charge density in the axial electric field expression. It is also discussed how the transverse beam distribution affects the longitudinal dynamics. We later showed the step-by-step derivation of the KdV equation from the code fluid model and its scaling technique.

Chapter 3: Experimental Setup and Diagnostic Tools

This chapter reviews the experimental setup of the beam perturbation experiments and diagnostic tools. First (Sec. 3.1), we briefly introduce the machine used, the University of Maryland Electron Ring (UMER), a storage ring utilized for research on space-charge-dominated beams. Next (Sec. 3.2), we discuss the UMER electron gun used to generate thermionic beams, on top of which a narrow perturbation pulse of varying strength and width can be produced through photoemission. Section 3.3 discusses the setup of the photoemission drive laser. Sec. 3.4 reviews the beam modulation methods using an induction cell, q-switching and a DMD setup. We then review the beam diagnostics used in this experiment in Sec. 3.5, mainly on the Bergoz coil, pyrometer and wall current monitor. Finally, Sec. 3.6 summarizes the overall chapter.

3.1 The University of Maryland Electron Ring (UMER)

UMER [Fig. 3.1] is a scaled world-class facility designed for exploring the physics of space charge over a wide range of intensities. It is a circular machine with a circumference of 11.52m. The 10 keV electron beam is injected as a single long bunch, with a duration that we can vary from 25 to 140 ns. By means of apertures, [Fig. 3.2] downstream from the anode, we can vary the peak beam current and rms emittance over the range 0.5-100 mA and 0.3-3 μm (normalized), respectively. The basic beam parameters of UMER and aperture sizes are shown in Table 3.1 and 3.2.

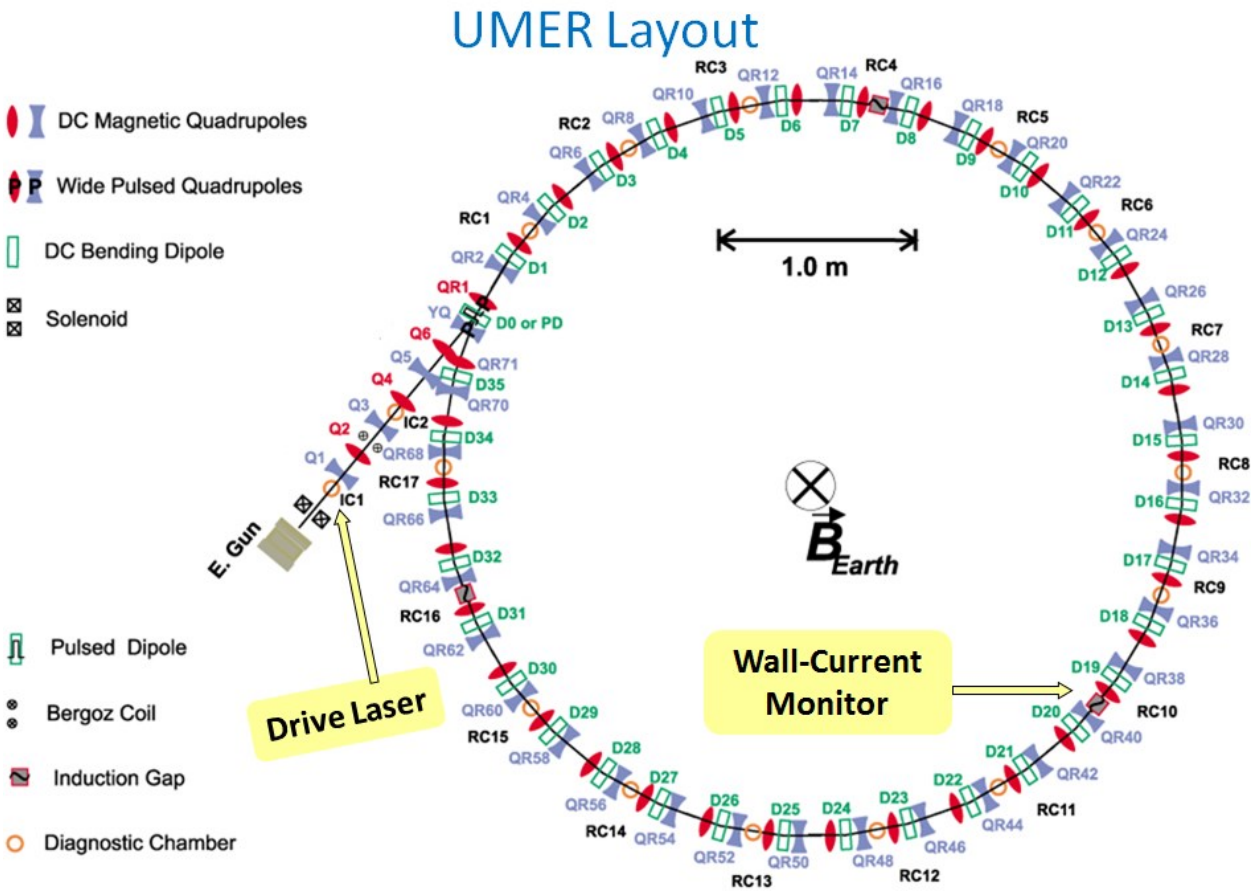

Fig. 3.1: Schematic illustrating the UMER layout (Top view). The arrows indicate the diagnostics used for the experiments described here.

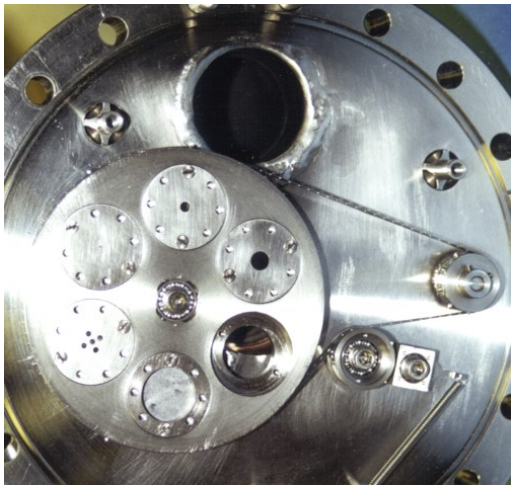

Fig. 3.2: Photograph of the aperture wheel for beam selection, downstream from the anode.

Table 3.1: Beam Parameters of UMER

Beam Energy	10 keV
Beam Velocity (β=v/c)	0.2
Beam Current	0.5-100 mA
Bunch Length (thermionic emission)	25 to 140 ns
Bunch Repetition Rate	10-60 Hz
Circulation Time	197 ns
Circumference	11.52 m
FODO Period	0.32 m
Zero-current Phase Advance	67°

Table 3.2 Aperture Radius and Exiting Beam Current, Emittance

Aperture Raius (mm)	Beam Current (mA)	Normalized Emittance (μm)
0.25	0.6	0.4
0.875	6	1.3
1.5	21	1.5
2.85	78	2.9
Full Beam	104	3.2

The ring consists of a 36-period FODO lattice with an injection section that uses 6 quadrupoles and a solenoid for matching. One of the FODO sections in the ring uses a fast pulsed dipole for injection, after which the polarity of that dipole switches for recirculation. The beam current is measured initially using a Bergoz current transformer located 64 cm downstream from the gun aperture wheel. Details of the transverse distribution are measured in the nearby Diagnostic chamber IC1, as well as at other chambers downstream. IC1 also houses a mirror we use to aim the drive laser onto the cathode. We use a wall-current monitor at RC10, 7.67 m downstream from the Bergoz, to measure the beam current profiles at each turn.

3.2 Electron Gun (Thermionic Emission)

The UMER gun is a gridded Pierce-type gun with a thermionic dispenser cathode [Fig. 3.3], made of porous tungsten (W), coated with barium oxide and calcium aluminate. The entire cathode/grid assembly as biased to -10 kV relative to the anode using a dc high-voltage power supply. Under normal operation, a negative bias (30 V) on the cathode grid suppresses electron emission. A larger negative, rectangular, pulse (51 V), applied on the cathode at a rep rate from 10-60 Hz, is used to extract the electron beam. A Pierce electrode (conical electrode surrounding the cathode with a cone angle of 67.7°) is applied to balance the transverse space charge force to make a uniform laminar beam. The A/K gap can be changed to vary the gun's perveance. For an A/K gap of 25 mm, the gun produces a space-charge limited current of 100 mA, which we can reduce using apertures downstream. For more description about the gun, refer to [41].

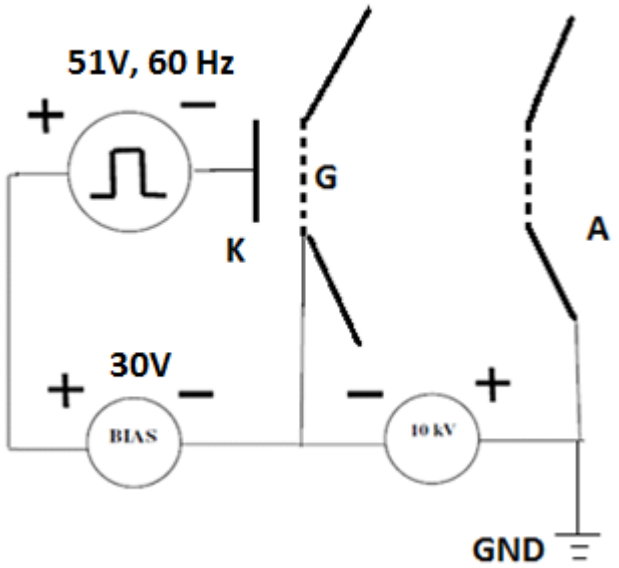

Fig. 3.3: Simplified schematic of UMER gun for thermionic emission.

The gun operates in two modes: temperature-limited mode (650-850 ℃) and space-charge limited mode (>1000 ℃). In the space-charge limited mode, which is used for normal operation,

the current is limited by the Child-Langmuir law, where any increase in the heater voltage doesn't affect the current output. For the perturbation experiments, I operated the gun in the temperature-limited mode so that the photo-emitted electrons generated by the drive laser lead to a perturbation in the beam density. Operating in the temperature-limited mode further allows us to easily adjust the peak beam current by simply changing the cathode temperature. As shown in Fig. 3.4, there is an exponential current growth in the temperature-limited mode (heater voltage between 40V to 50V), where any fluctuation in electron density also gets amplified at the cathode. Therefore, the beam pulse tends to be noisier than that in normal, space-charge-limited operation.

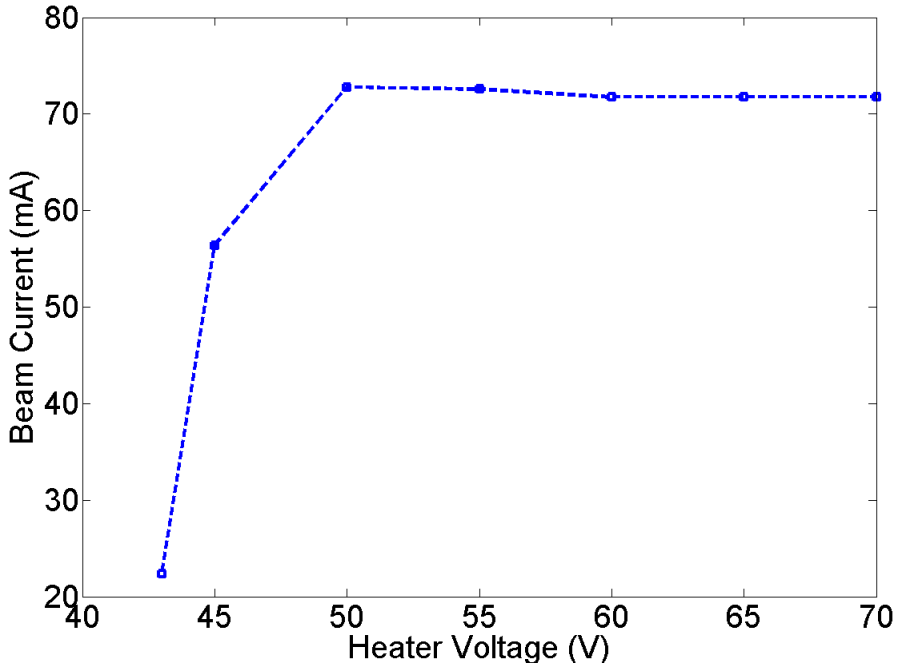

Fig. 3.4: Measured beam current vs heater voltage for the UMER gun (80mA aperture). After an exponential growth, the beam saturates. The displayed heater voltage is about 10 times the real voltage, see Table 3.4 for details.

In the experiments presented here, we used the 80mA beam aperture, and cool down the cathode (about 4-5V of heater voltage) to produce a beam with peak current in the range 20-40mA. The repetition rate is set to 15Hz to synchronize the gun with the laser for photoemission (see next section).

One problem that occurs while operating the gun in temperature limited mode, is that the cathode cools down after a long-period of data acquisition [42]. Table 3.3 shows how the cathode temperature decreases before the reading stabilizes. The beam current is stable in the space charge limited mode. However, it keeps decreasing slowly until almost 0 after one hour when the heater voltage is set to 40 V, which locates on the exponential growth curve Fig.3.4. Therefore, it is very important to ensure that the beam current is stable under the temperature limited mode.

Table 3.3 Beam current decreases with time.

Heater Voltage(V)	Beam Current(mA)	Waiting Time before Stabilization
60	72	10 mins
55	72.64	10 mins
50	73.92	10 mins
45	70.88	10 mins
40	2	1 hour

One solution to the cathode cooling problem is to build feedback automation on the cathode temperature by controlling the heater voltage [Fig. 3.5]. The cathode heater voltage driving module can communicate with computer user interface through GPIB cable connection. Compare the measured beam current with the value we set, and adjust the heater voltage accordingly by a certain step voltage ΔV every minute until the current difference between the

real and ideal values stays within an acceptable error ΔI. The controlling script for the temperature can be referred to Appendix B.

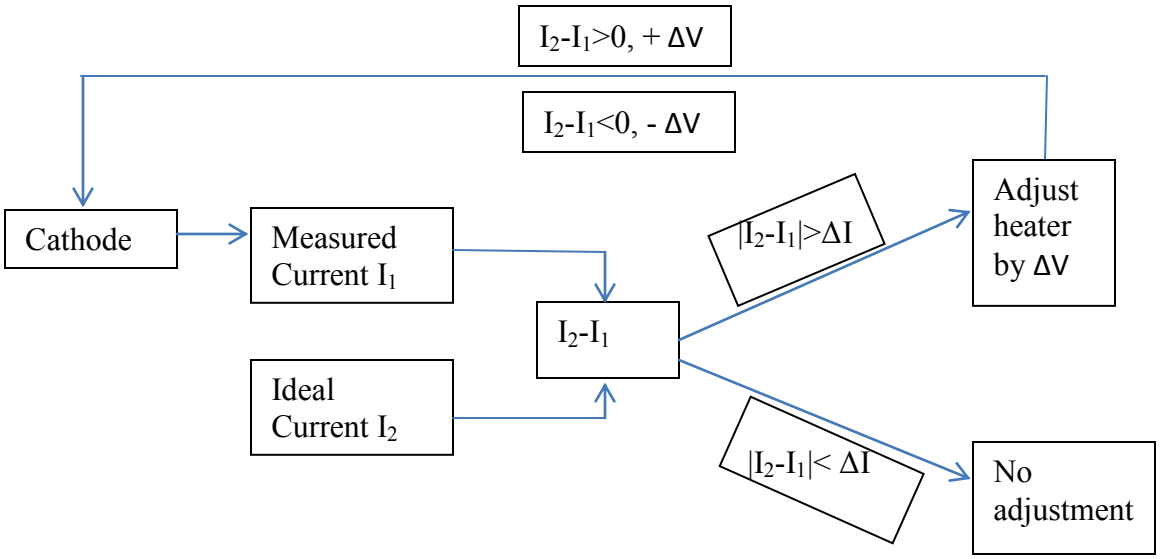

Fig. 3.5: Diagram for cathode heater voltage feedback design.

Another problem is the cathode aging. In some experiments, we observe that the cathode no longer emits as much current as it used to [43]. The emitted beam current grows with the cathode temperature, which can be measured by a pyrometer (see Sec. 2.5). A set of data on heater voltage vs temperature is shown in Table 3.4 and Fig. 3.6. It can be used as a future reference for cathode aging by comparing the temperatures at the same heater voltage.

Table 3.4 Cathode heater voltage vs temperature

Heater Controller(V)	Heater Voltage (V)	Temperature TU (℃)	Temperature TE (℃)
5	0.396	unreadable	unreadable
10	0.801	unreadable	unreadable
15	1.267	unreadable	unreadable
20	1.752	unreadable	unreadable
25	2.23	unreadable	unreadable
30	2.712	unreadable	unreadable
35	3.195	unreadable	unreadable
40	3.67	unreadable	unreadable
45	4.16	774	822
50	4.64	805	855
55	5.13	850	905
60	5.61	908	970
65	6.1	943	1008
70	6.59	1003	1075
75	7.07	1028	1103
80	7.56	1057	1135

Note: The beam emissivity (range from 0-1, depends on the cathode material) is assumed to be 0.4. There are two readings on the pyrometer, the TE (℃) term is the actually source temperature, which is a corrected value from TU (℃) and emissivity.

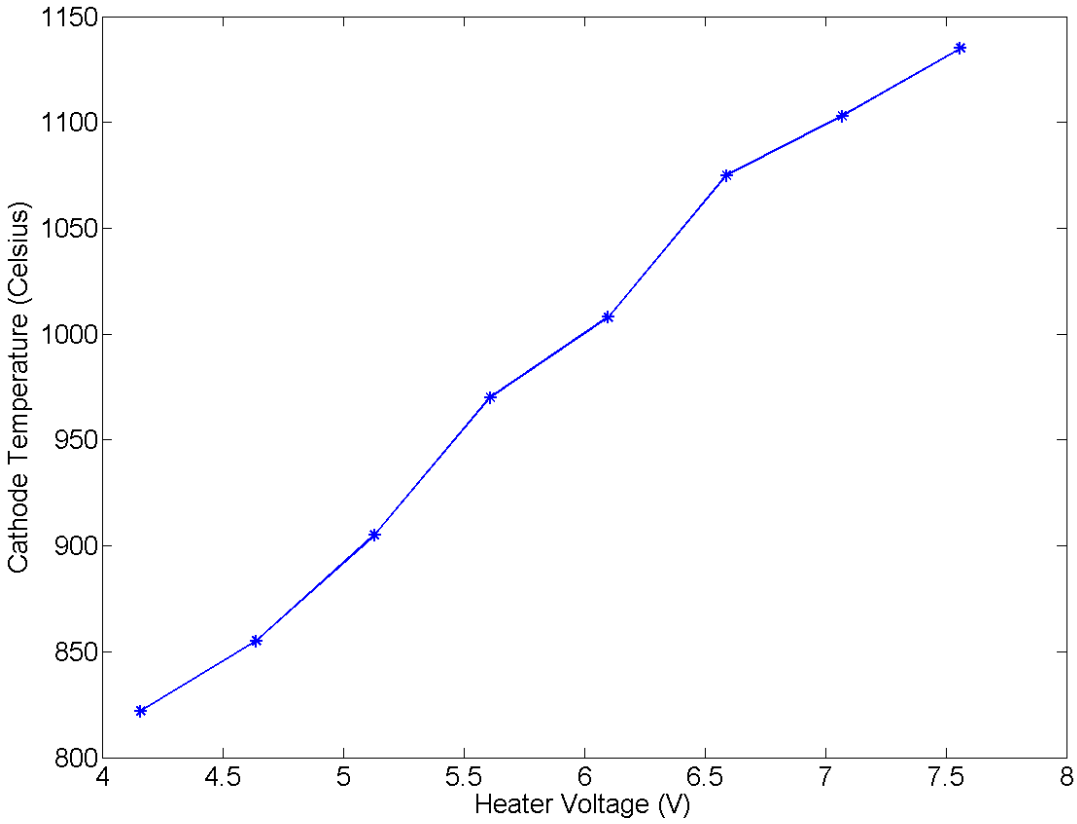

Fig 3.6: Cathode temperature as a function of heater voltage, it reaches beyond 1100℃ at the normal operating point as expected.

3.3 Laser Setup (Photoemission)

The UMER gun is also able to generate beams through photoemission [20], which can be applied to introduce perturbations on the beam. We use a 1064 nm-wavelength Nd-YAG drive laser and triple its frequency with two nonlinear crystals to a wavelength of 355 nm [Fig. 3.7], making the photon energy sufficient to generate photoemission from the cathode. The laser is injected into the chamber (IC1), where it is reflected by a mirror towards the cathode. The beam perturbation measured at the Bergoz is 6.5 ns +/- 1.5 ns ns wide.

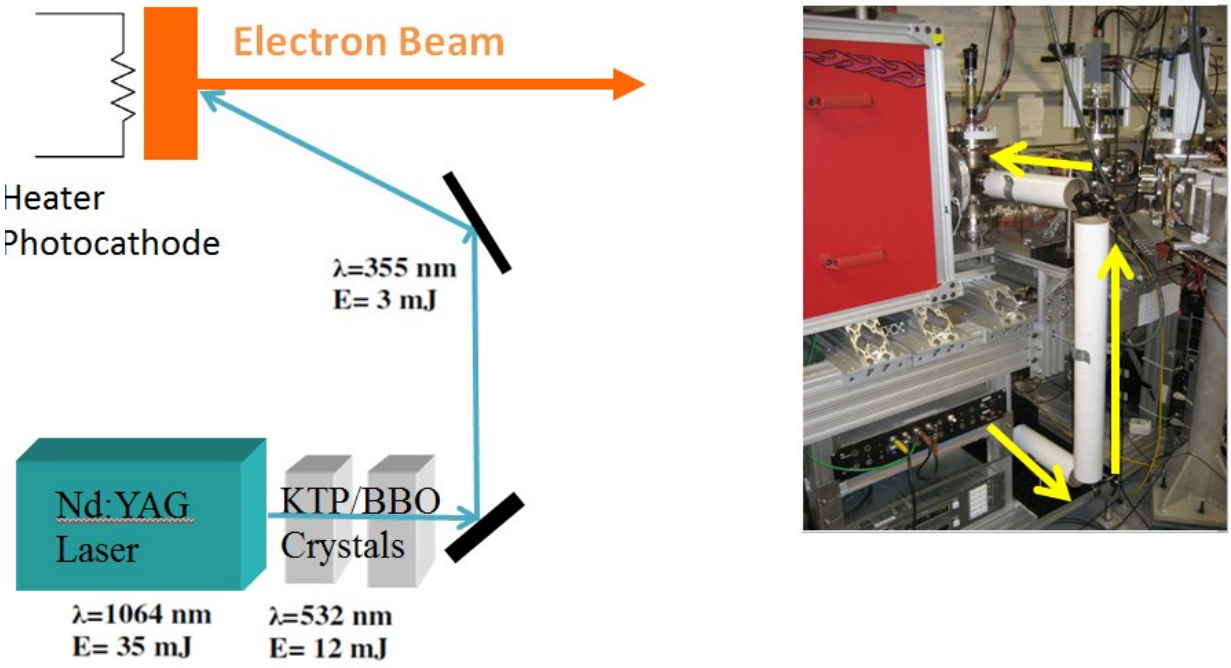

Fig. 3.7: Experimental setup of beam perturbation by photoemission.

We use a Nd YAG minilite II model laser [44]. Table 3.5 lists the basic parameters of this laser. The 3rd harmonic temporal profile was measured using a PIN diode, resulting in a Gaussian distribution, as shown in Fig. 3.8.

The optical alignment is an important process [Appendix A] which ensures that the laser hits right at the cathode. Due to the synchronization between the triggering source of the beam bunch and pulsed laser, the perturbation is introduced on every beam bunch. By changing the time delay of the laser Q-switch trigger, we can set the perturbation at different locations atop of the beam. The pulse width is also adjustable by changing the time separation between the triggers of Q-switch and flash lamp [44], however at the cost of intensity modulation. An alternative to widening the pulse is to combine two laser pulses with a slight time delay as shown in Fig. 3.9.

Table 3.5: Nd:YAG Laser Parameters

Wavelength	1064 nm	532 nm	355 nm	266nm
Energy	50 mJ	25 mJ	8 mJ	4 mJ
Peak Power	8.3 MW	6.3 MW	2.0 MW	1.0 MW
Average Power	750 mW	375 mW	120 mW	60 mW
Pulse width	5-7 ns	3-5 ns	3-5 ns	3-5 ns
Stability	2%	3%	4%	8%
Polarization	Horz.	Vert.	Horz.	Horz.
Jitter	< +/- 0.5 ns			
Beam Size	< 3 mm			
Divergence	< 3 mrad			
Repetition Rate	1-15 Hz			

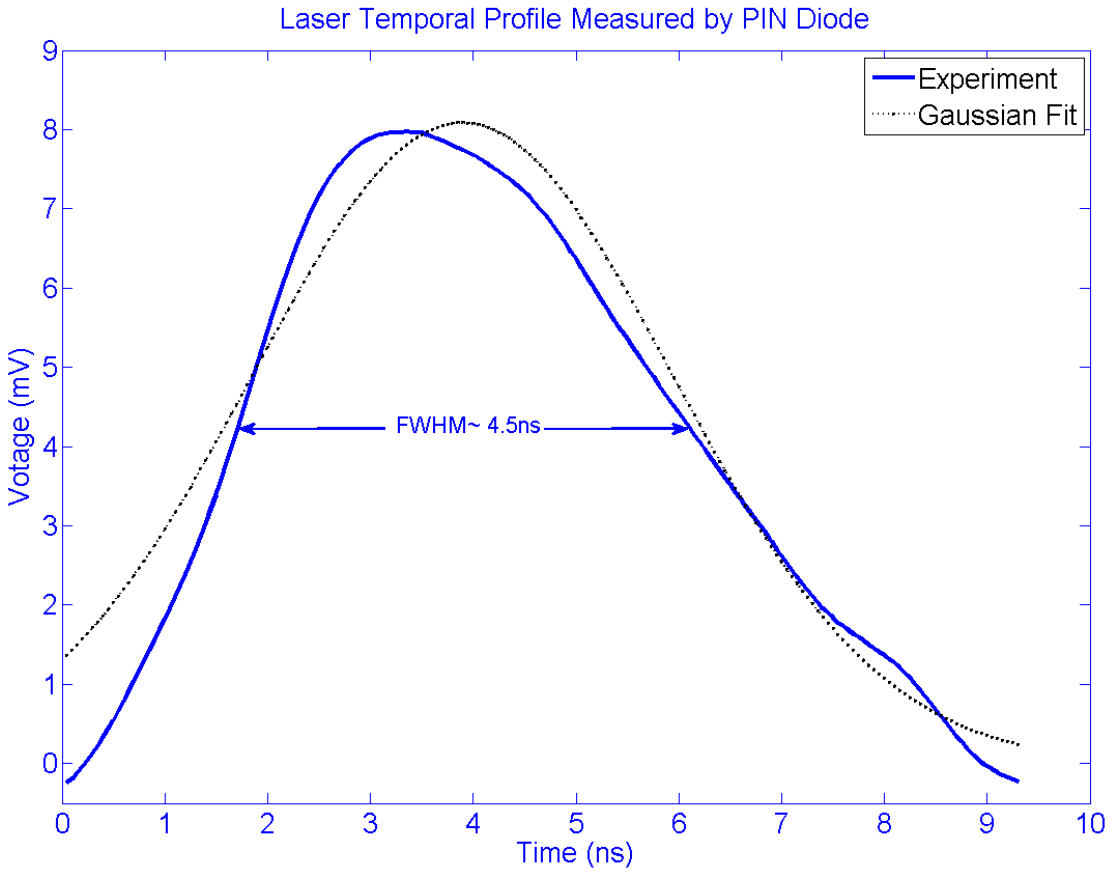

Fig. 3.8: Temporal profile of the 355nm laser for photoemission.

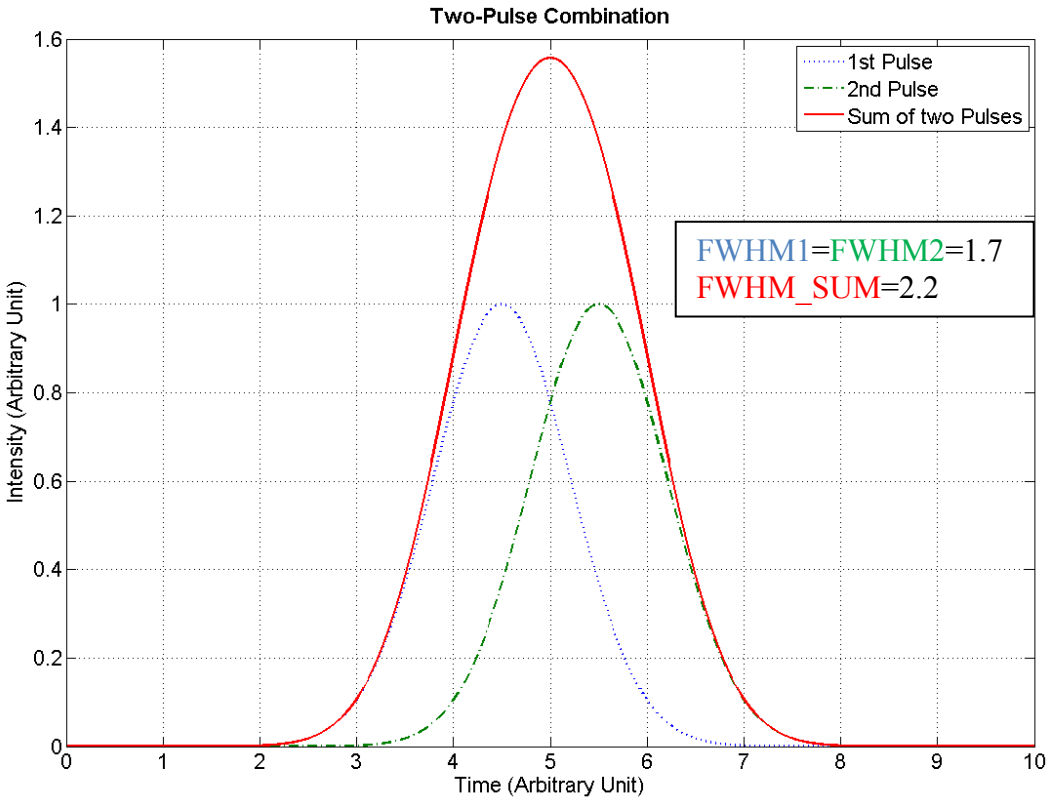

Fig. 3.9: Pulse widening by combination of two pulses with a time delay.

3.4 Beam Modulation Methods

This section discusses beam modulation methods other than photoemission, such as velocity modulation and pulse focusing/compression using the induction cell, pulse slicing by q-switches, and adjusting beam transverse distribution by DMD mirrors.

3.4.1 Induction Cell

The induction cell can be used to accelerate/decelerate the beam by applying a voltage pulse. Its equivalent circuit [Fig. 3.10] consists of a resistance, capacitance and inductance, plus a high-voltage modulator that is connected to the circuit to provide various pulsed electric fields. The real structure is shown in Fig. 3.11. It can also focus the beam longitudinally when one

negative pulse is applied at the beam head, and a positive pulse applied to the beam tail [Fig. 3.11]. In UMER, this technique helps the beam propagate up to 1000 turns. For more details, refer to [45].

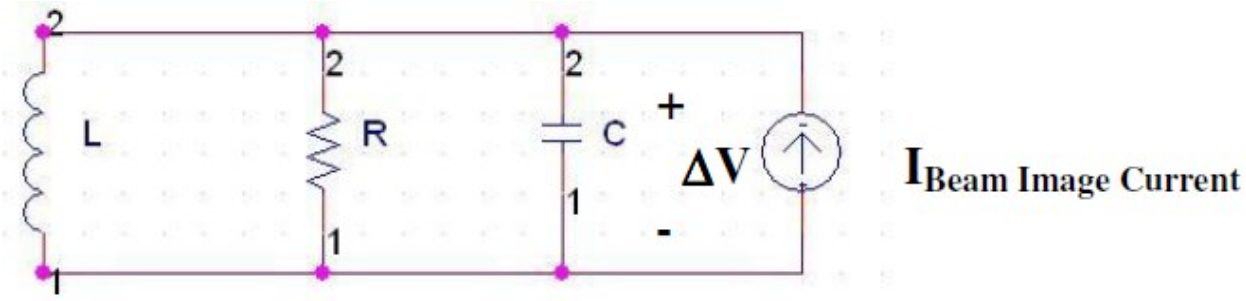

Fig. 3.10 : Equivalent RLC circuit of the glass gap. The overall impedance is jωL||R||1/jωC.

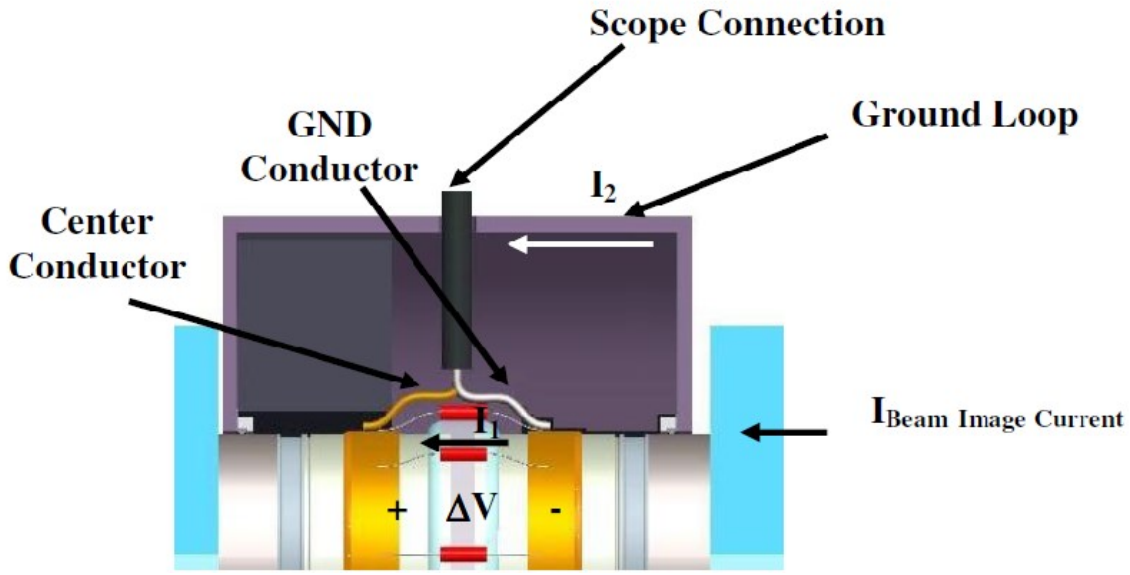

Fig. 3.11: The glass gap structure of the induction cell. For more information, refer to [23].

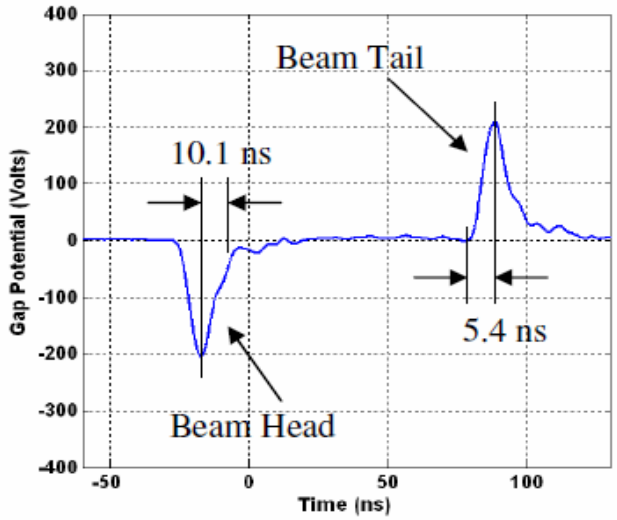

Fig. 3.12: Induction cell voltage versus time [23].

If the focusing fields are applied on top of the beam, an energy perturbation will be generated, which could further develop into a density perturbation and also lead to space charge wave pair despite a polarity difference [Fig. 3.12].

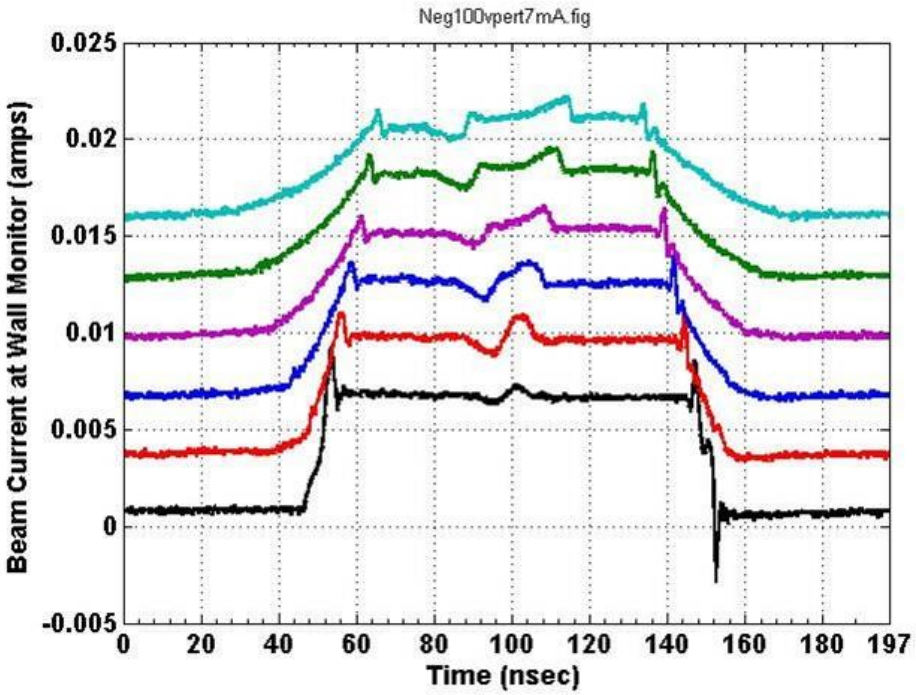

Fig. 3.13: The density perturbation fast/slow wave pair induced by a negative velocity perturbation using the induction cell.

Using the induction cell, we are able to decrease the spacing between the two energy perturbations [Fig. 3.12] and generate an energy tilt. This can be applied to compress a density perturbation. As shown in Fig 3.14, for electrons in the stable region, the head is slowed down while the tail gets accelerated, resulting in an overall compression of the perturbation. The focusing strength depends on the applied voltage tilt. Therefore, we can potentially narrow the perturbation width down to about 1 ns (6cm), which is comparable to the pipe radius. This is a practical technique for dispersion effect studies in UMER.

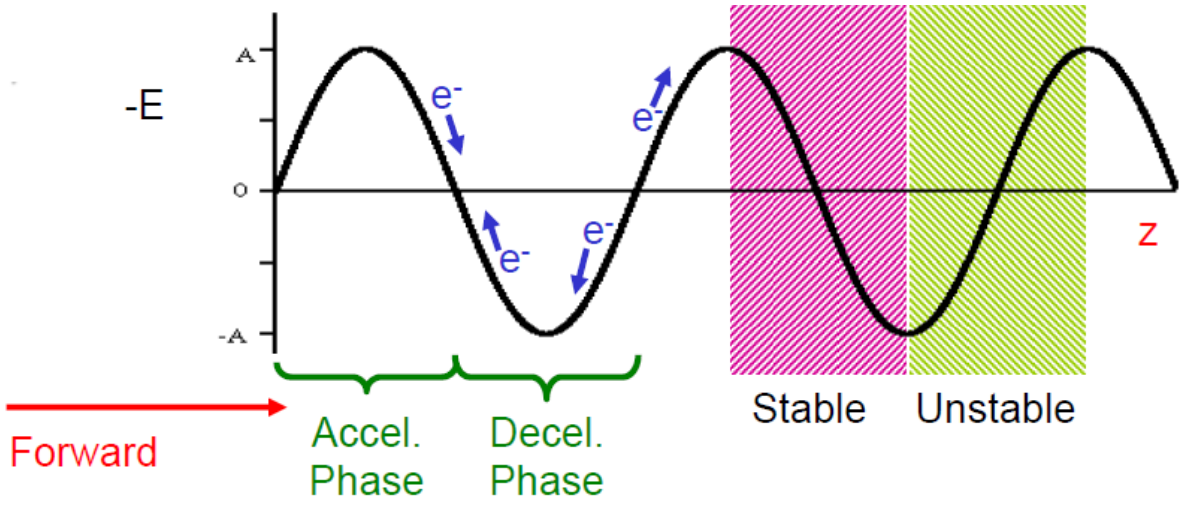

Fig. 3.14: Phase dynamics of the focusing/defocusing electric field [46].

3.4.2 Q-switching for Beam Slicing

Rather than looking for a class IV laser with a much narrower pulse, we can filter a portion of the Nd-YAG optical pulse to get a 1 ns scale using optical switches. Based on the laser setup for photoemission in Sec. 3.3, we add an active Q- switch such as a Pockels Cell and polarizer behind the laser. Due to the electro-optic effect, the Q-switch can change the device polarization to pass/block the laser beam with a triggering source. Therefore, by turning the Q-switch on and off within 1 ns, we can filter out a 1 ns wide laser pulse. Alternatively, a passive

Q- switch, i.e., a saturable absorber could also do the work as long as it has the right threshold intensity, above which it will allow beam transmission. The passive Q-switch is usually more cost-effective compared with its active counterpart, but it does not support external triggering. An example of passive Q-switch could be seen is Fig. 3.15, while Fig. 3.16 shows the updated laser perturbation experiment setup.

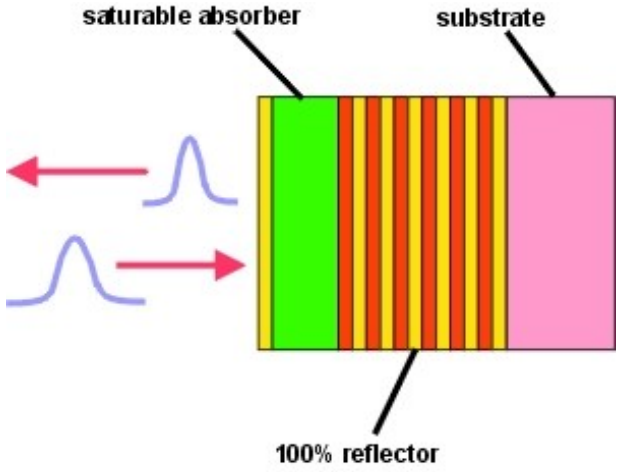

Fig. 3.15: The pulse focusing effect by a saturable absorber, such as Semiconductor Saturable Absorber Mirrors (SESAM).

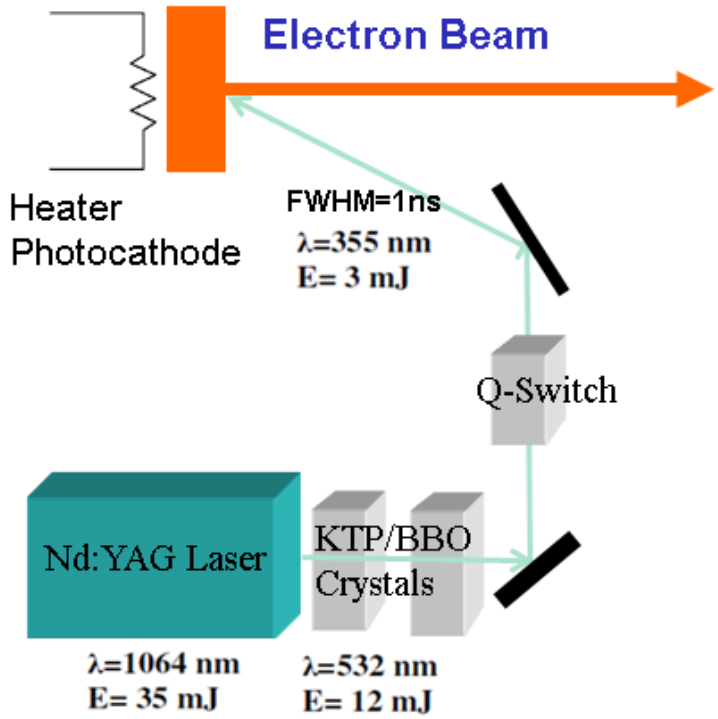

Fig. 3.16: The updated laser perturbation experimental setup with the introduction of Q-switch.

3.4.3 DMD Mirrors for Transverse Beam Distribution Modification

The digital micro-mirror array device (DMD) a digitally controlled MEMS device; where every pixel can be set to reflect the incoming light toward different directions. Therefore, it can be used as a spatial (transverse) light modulator when incorporated into the laser optical system [Fig. 3.17]. The specifications of the DMD mirror in UMER, the "DMD Discovery 1100" manufactured by Texas Instruments Inc. [47] are shown in Table 3.6. For more about DMD mirrors, refer to [48].

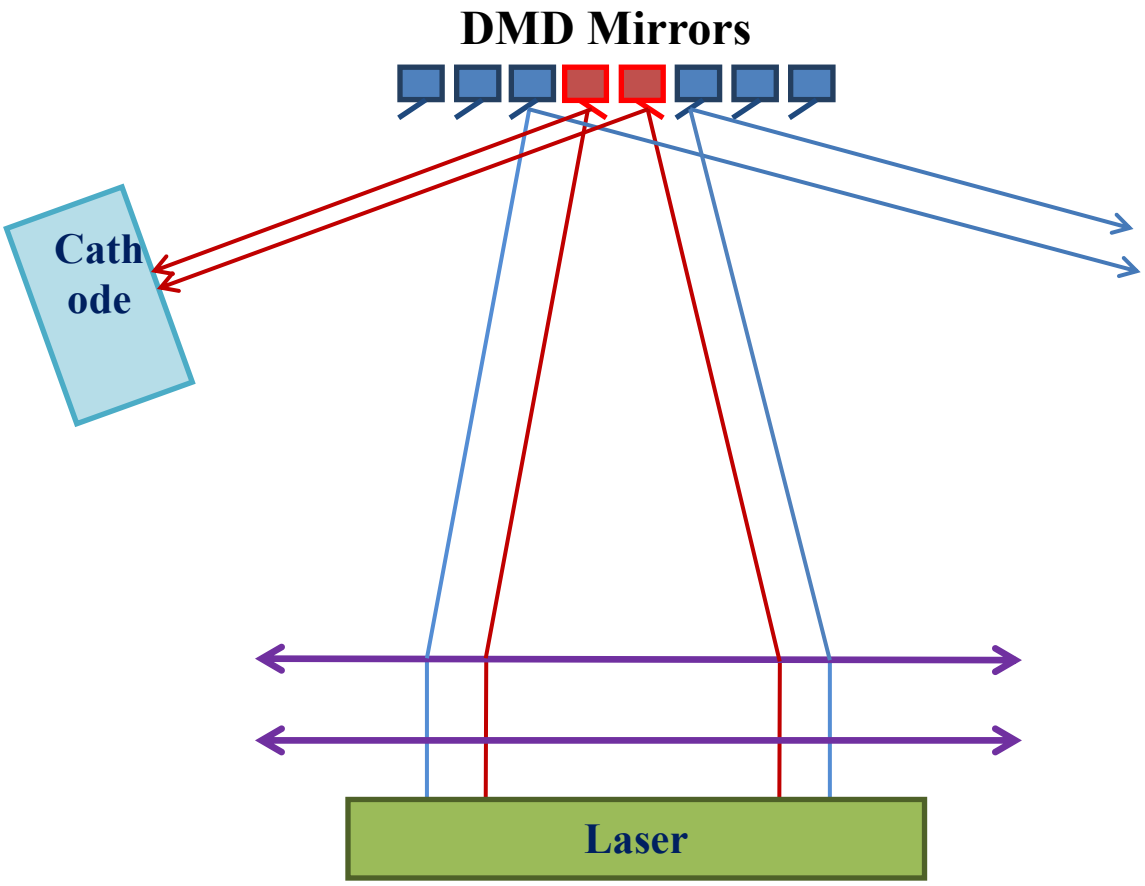

Fig. 3.17: DMD mirrors for transverse distribution modification of a laser beam.

Table 3.6: Key features of DMD Discovery 1100

Parameter	Value
Chip size	14.3 mm* 10.8 mm
Mirror size	13.68 µm*13.68 µm
Resolution	1024*768 pixels
Switching rate	9,600 frams/s
PC interface	USB 2.0
Control	GUI, ActiveX control

From Sec. 2.3, we know that the g-factor depends on the transverse beam distribution. Therefore, by adjusting the DMD mirror, we can obtain different g-factors, which affect the axial electric field, and eventually modify the space charge wave properties such as dispersion, phase velocity and etc. It is worthwhile to study the coupling between the transverse and the longitudinal beam dynamics with the DMD mirrors.

3.5 Beam Diagnostics

This section reviews the beam diagnostic tools that are directly related with our experiment. **The Bergoz coil** is a fast current transformer, model # FCT-082-20:1, with a rise time down to 200 ps, enabling fast and accurate measurements of the temporal beam current profile. Basically it is a transformer with the beam as the primary. After calibration, the initial beam current is: $I(mA) = 0.8 * U(mV)$, where $U(mV)$ is the output of the transformer.

The Wall current monitor (WCM) is an in-house device we use to give us accurate measurements of the temporal beam current profiles in the ring. It measures the voltage drop $U(mV)$ across the resistors cause by the image current excited by the beam. The beam current is: $I(mA) = U(mV) / 4.545$ for the UMER calibration.

The pyrometer is a type of thermometer for high temperature measurement. It consists of an optical system and detector. To measure the cathode temperature, we need to focus the cathode radiation to the detector, adjust the knob of the pyrometer to make the observed cathode match the reference color inside, then get the reading from the meter that is externally connected.

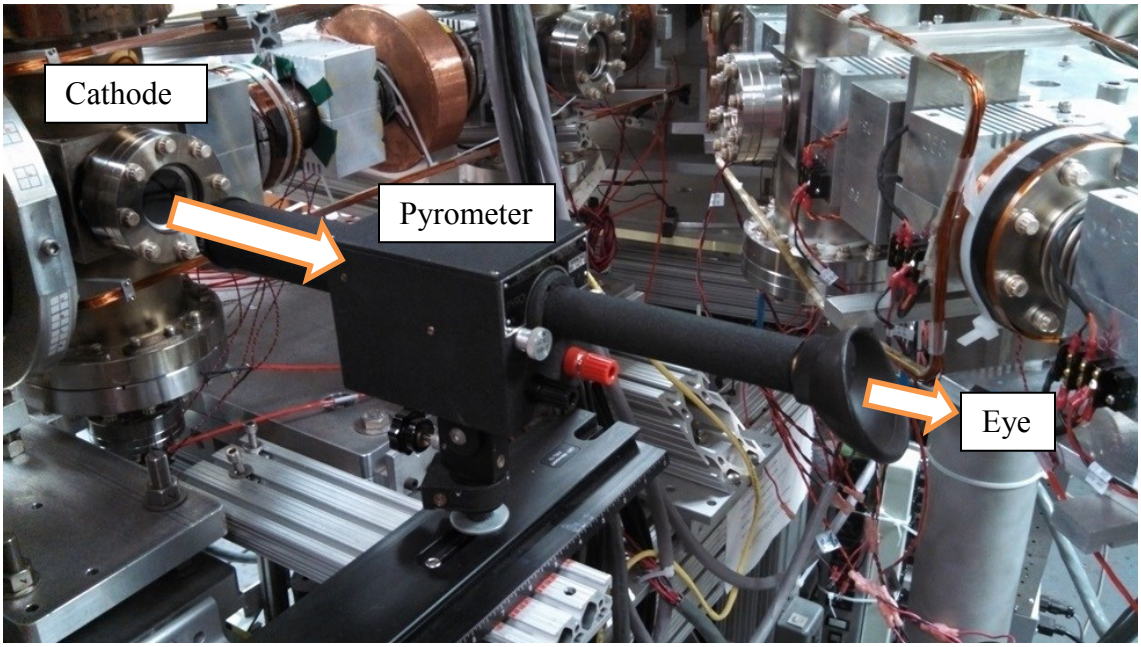

Fig. 3.18: Setup of pyrometer for cathode temperature measurement.

In addition, we also have **beam position monitor (BPM)** for beam centroid position diagnostics, and **(fast) phosphor screen** for beam imaging diagnostics, to measure the transverse profile and initial emittance [49]. For more details about the above diagnostic tools, refer to [23].

See Fig 3.19 for the difference the laser makes on the initial beam conditions. The perturbation is introduced at the edge because it maximizes the time duration of the wave propagation in the beam frame.

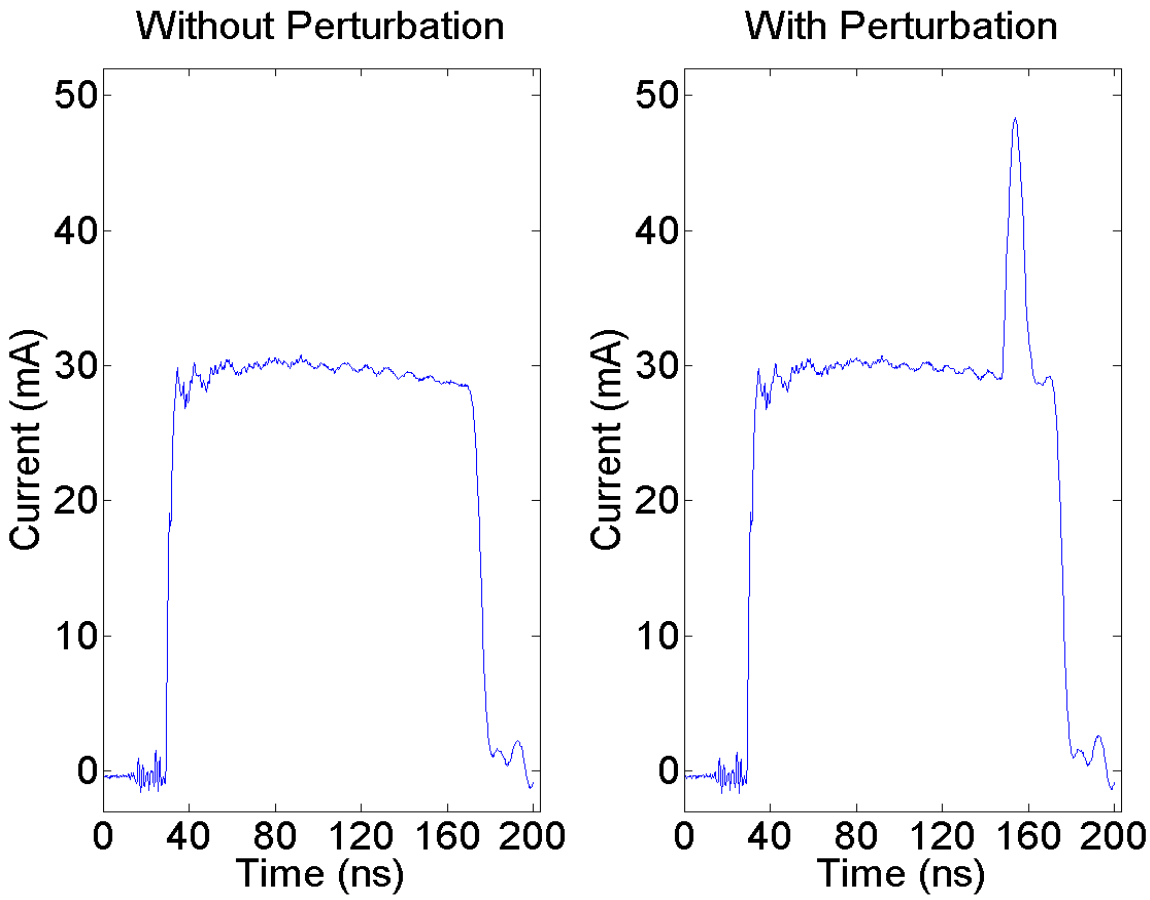

Fig. 3.19: An example output from the Bergoz coil for a beam with and without the perturbation.

3.6 Summary

We discussed the University of Maryland Electron Ring, the two mechanisms of generating electron beams from the gun and how the perturbation experiment is set up. Three different beam modulation methods are introduced. The beam diagnostics tools are shown lastly.

Chapter 4: Experimental Observation and Characterization of Solitons

In this chapter, we show our experimental observation of solitons on electron beams and compare the results with theory. We start (Sec. 4.1) with a representative soliton wave train formed from an initial large-amplitude perturbation. In Sec. 4.2, we discuss the properties of the waves thus formed and demonstrate they are solitons. In Sec. 4.3, we compare the experimental results with the theoretic KdV model. In Sec. 4.4, we investigate the soliton dependence on beam parameters such as beam current, perturbation strength and width. Sec. 4.5 shows the soliton interaction experiment by initiating two solitons from two initial large-amplitude perturbations. In Sec. 4.6, we discuss the improved beam injection with better matching and steering solutions. Sec. 4.7 shows the velocity soliton train generated by the perturbation from induction cell. Sec. 4.8 summarizes the chapter.

4.1 Single Large-Amplitude Initial Perturbation

Previous studies on the space-charge waves show from both the theoretical and experimental perspective that a small-amplitude initial perturbation launches into two space charge waves, a slow wave and a fast wave. In the beam frame, the two waves propagate with same phase velocity (or sound speed, Eqn. 2.6) but towards opposite directions. However, when the perturbation amplitude is large (normally >20%), the linear approximation for sound speed derivation no longer stands, and the phase velocity increases with the perturbation strength [11]. Therefore, the peak wave travels faster than the base, and the wave will eventually steepen and

develop into multiple sub-pulses. Meanwhile, when the pulse width is comparable to the pipe radius, the wave becomes dispersive and it can balance the steepening effect, to maintain the pulse shape and lead to solitary wave formation.

Figs. 4.1 and 4.2 are typical experimental results of a nonlinear density perturbation on the beam. In Fig. 4.1, the initial peak current measured at the Bergoz is 22 mA with an additional 11 mA perturbation (we will hence call it a 50% perturbation). The perturbation is introduced near the beam tail to allow the fast wave to propagate longer on the flat-top portion of the beam. Fig. 4.2 depicts the turn-by-turn beam current measured at RC10. The beam current in each turn is plotted on the same scale (centered on the beam pulse), with each turn shifted upward by 20 mA for clarity. For a different way of visualization, Fig. 4.3 is a 3D depiction of the same data in Fig. 4.2. The slow wave steps off the beam edge after the perturbation splits (in Turn 1). Meanwhile, the fast wave moves towards the beam head (to the left in Fig. 4.2) steepens, and develops into several sub-pulses. Starting from about the 4th turn, the sub-pulses maintain their shape in the beam frame (see Sec. 4.2), which is a basic property of solitons. Also, the sub-pulse width is measured to be ~1ns, which is 6 cm long, comparable to the pipe diameter of 5.08 cm.

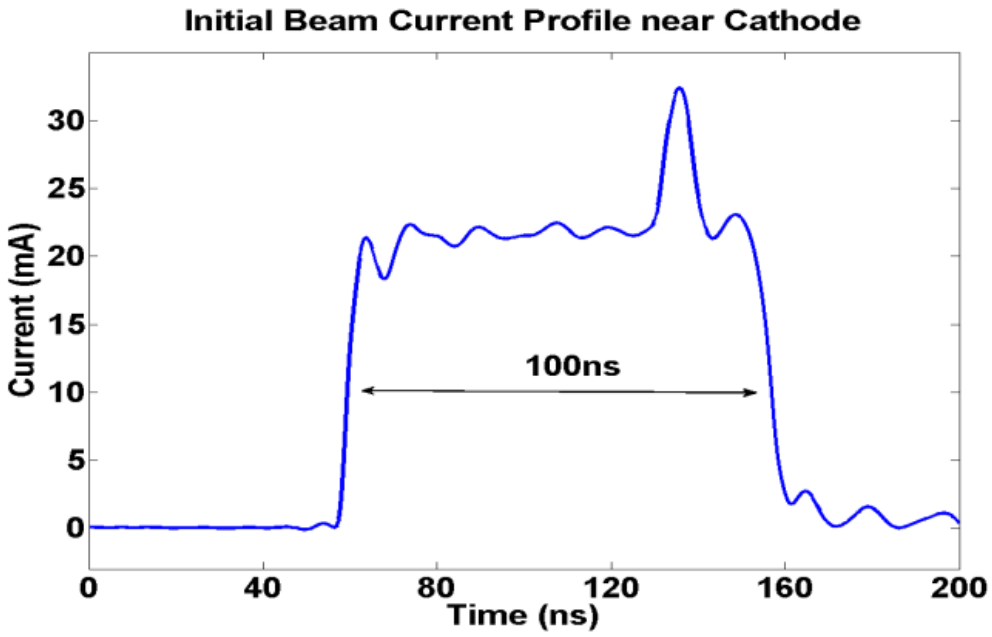

Figure 4.1: Initial beam condition measured at the Bergoz coil, for a 22 mA beam and a 50% perturbation.

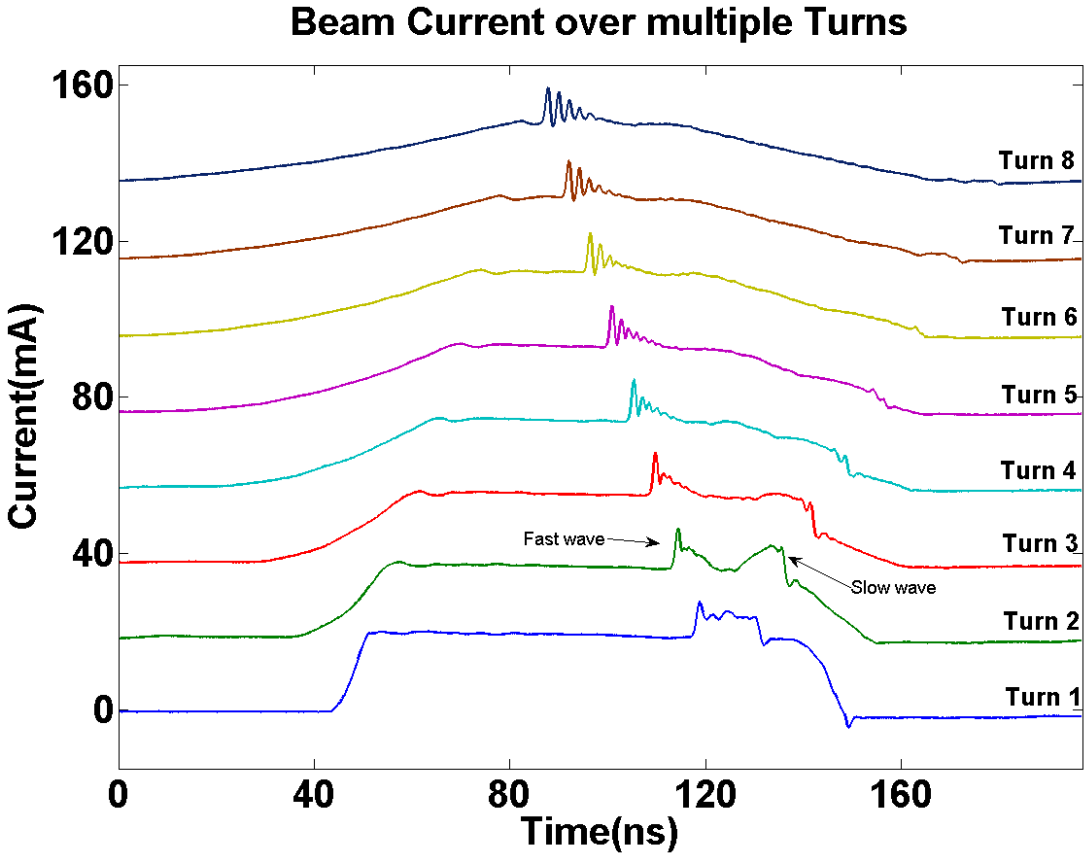

Figure 4.2: Turn-by-turn plot of beam propagation at wall current monitor (RC10), for a 22 mA beam and a 50% perturbation.

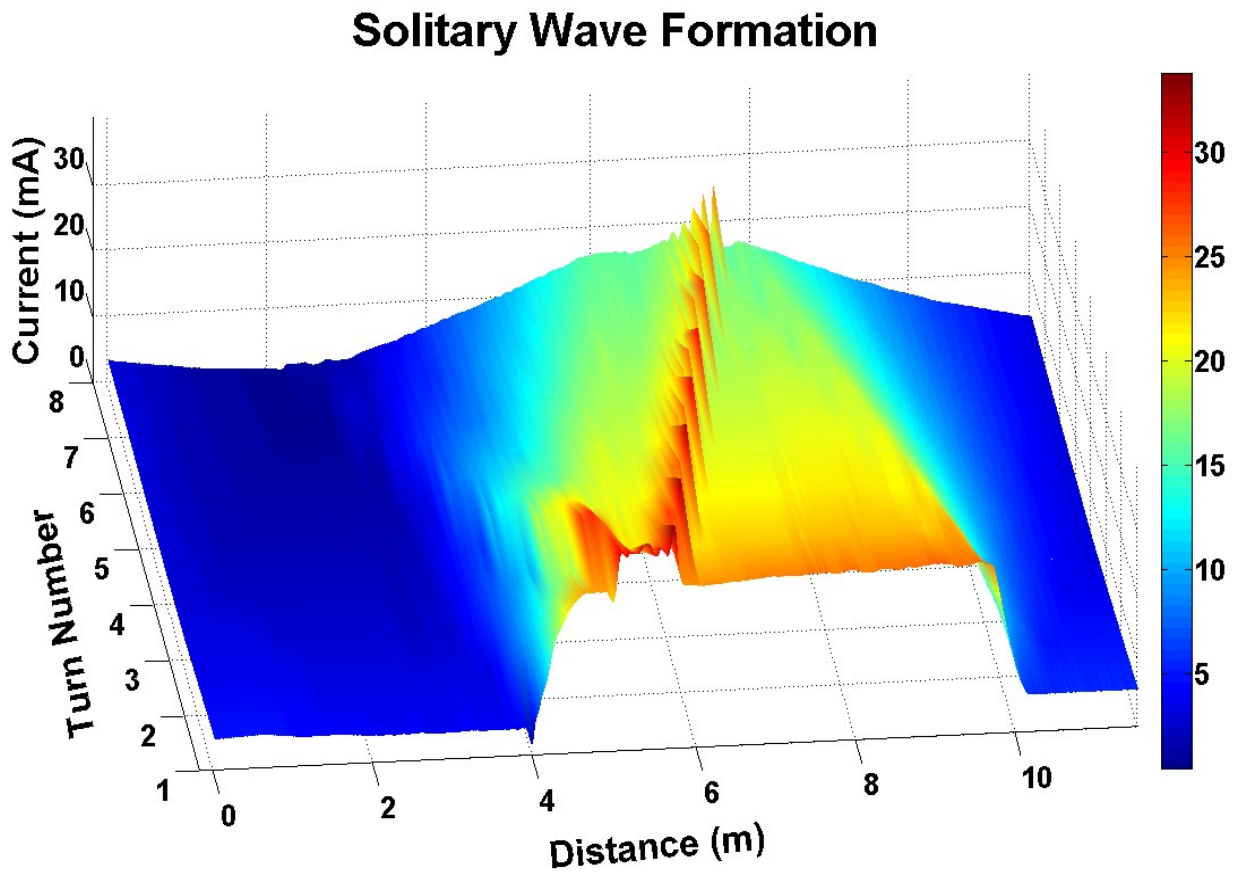

Figure 4.3: 3D Turn-by-turn plot of beam propagation at wall current monitor (RC10), for a 22 mA beam and a 50% perturbation.

4.2 Data Analysis for Soliton Properties

In this section, we analyze in detail the results of the experiment presented in Sec. 4.1 (22 mA, 50% perturbation). Results of the experiments presented in subsequent sections can be similarly analyzed and all show evidence of soliton behaviors. A solitary wave has the property that it maintains its shape over a long distance, i.e., constant width and constant amplitude. As we illustrate in Fig. 4.4, the sub-pulse maintain its shape, within the measurement errors.

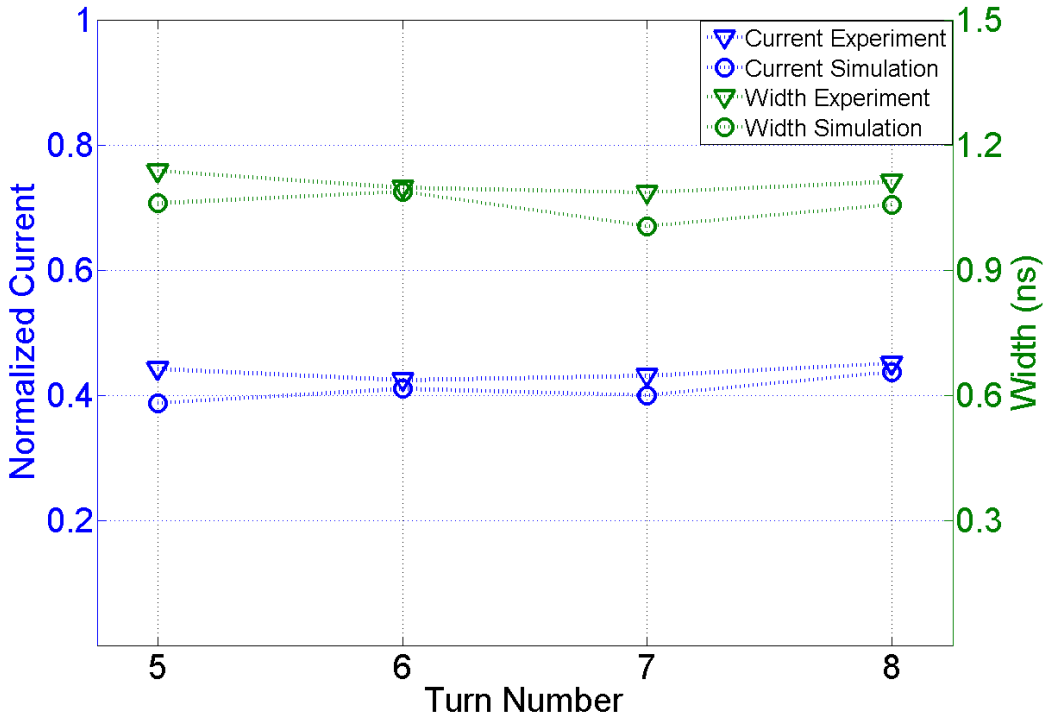

Figure 4.4: Soliton width and amplitude at different turns in the ring with both experimental and simulation data, from the 1st sub-pulse of the 22mA 25% perturbation experiment. Data points from turn 1-4 are dropped since the solitary wave train is not fully generated.

At the same time, the KdV solitons have a solution in the form of Eqn. 2.42, from which we can see that the width ($\propto 1/\sqrt{c}$) of the soliton is inversely proportional to the square root of its velocity (c), while the soliton velocity is proportional to the amplitude. From these two conditions we expect: **width^2 * amplitude = constant**. The experimental results agree with this relation, as shown in Figs. 4.5 and 4.6.

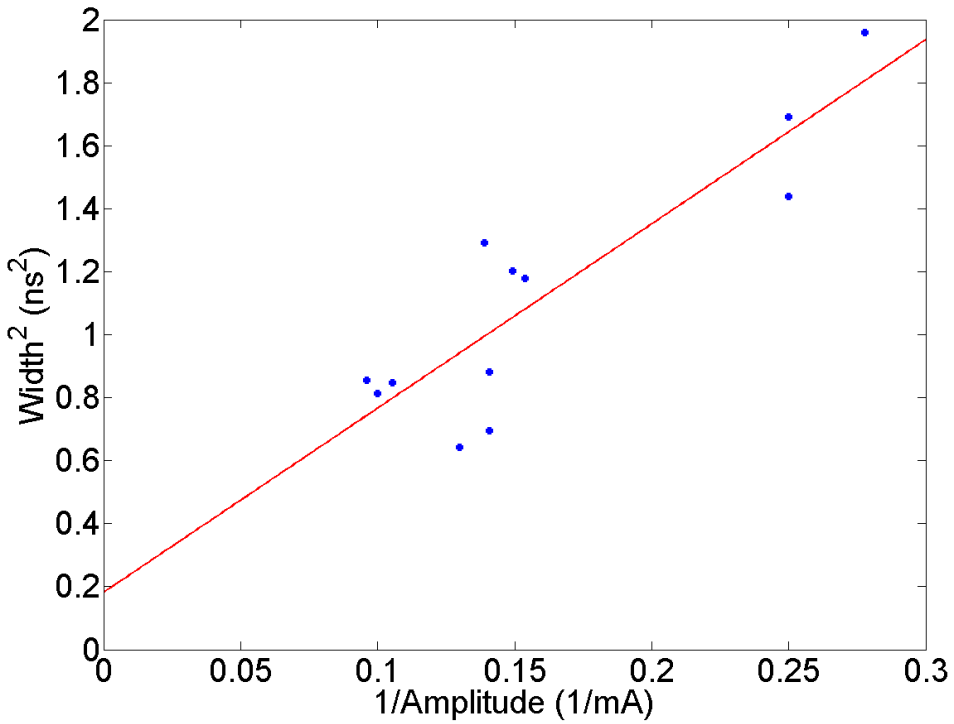

Figure 4.5: Plot of solitary wave's width^2 vs 1/Amplitude, along with its linear fit. The data points are from the 1st and 2nd sub-pulses of the wave train at 5th, 6th and 7th turn of the 22mA 25% perturbation, and 22mA 50% perturbation experiment, respectively.

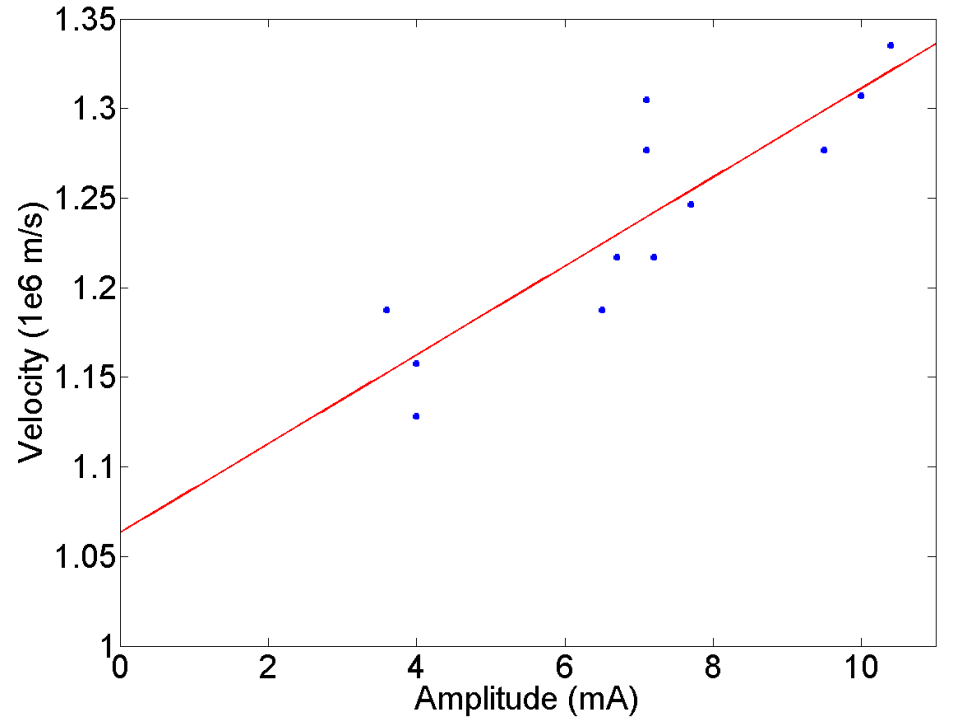

Figure 4.6: Plot of soliton velocity vs Amplitude, along with its linear fit. Same data points with the ones in Figure 4.5.

Due to the beam mismatch at the injection, there's about 10% beam loss from Bergoz to wall current monitor at the first turn, and 5% loss per turn thereafter. It will decrease the sound speed of the perturbation and may cause errors to its amplitude and width. Better beam matching and steering solution are expected, see discussion in Sec. 4.5. The beam loss profile is shown in Fig. 4.7.

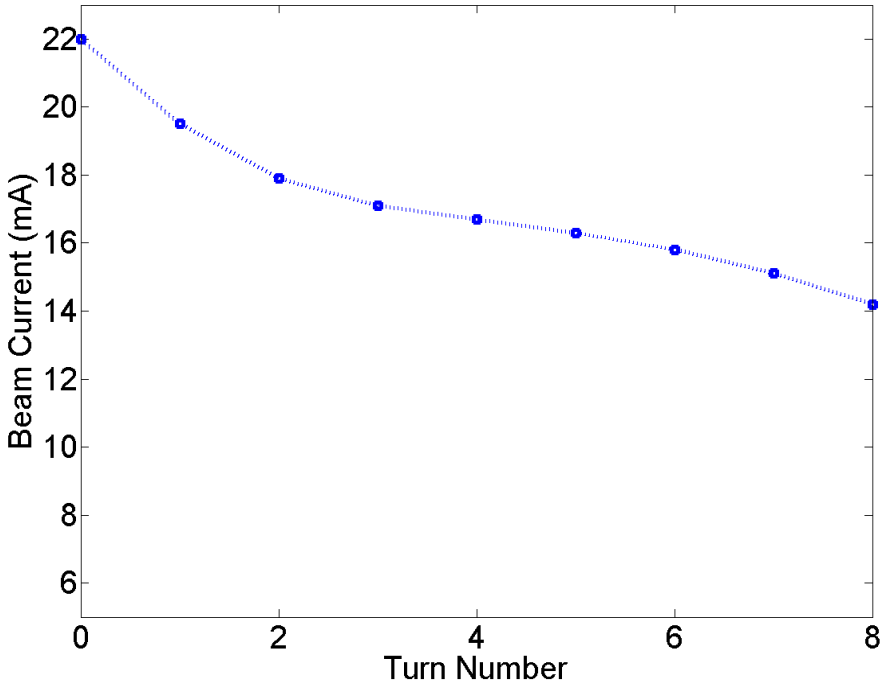

Figure 4.7: Beam current for each turn at wall current monitor (RC10), turn 0 represents the initial condition measured at Bergoz.

4.3 KdV Model Prediction and Comparison with Experiments

Based on the discussion in Chapter 2, we are able to predict the beam evolution by theory using the KdV model. Its comparison with experimental data is key to show what we observe are KdV-type solitons.

With the normalization defined in Sec. 2.4,

$$\eta = \frac{\lambda - \lambda_0}{\lambda_0}\ ,\ U = \frac{v}{v_{b0}}\ ,\ T = \frac{v_{b0}^2}{v_{b2}}\frac{t}{r_w}\ ,\ Z = \frac{v_{b0}}{v_{b2}}\frac{z}{r_w}$$

Take a 22mA beam, with 25% perturbation and 5.4 ns width pulse for example [Fig. 4.8].

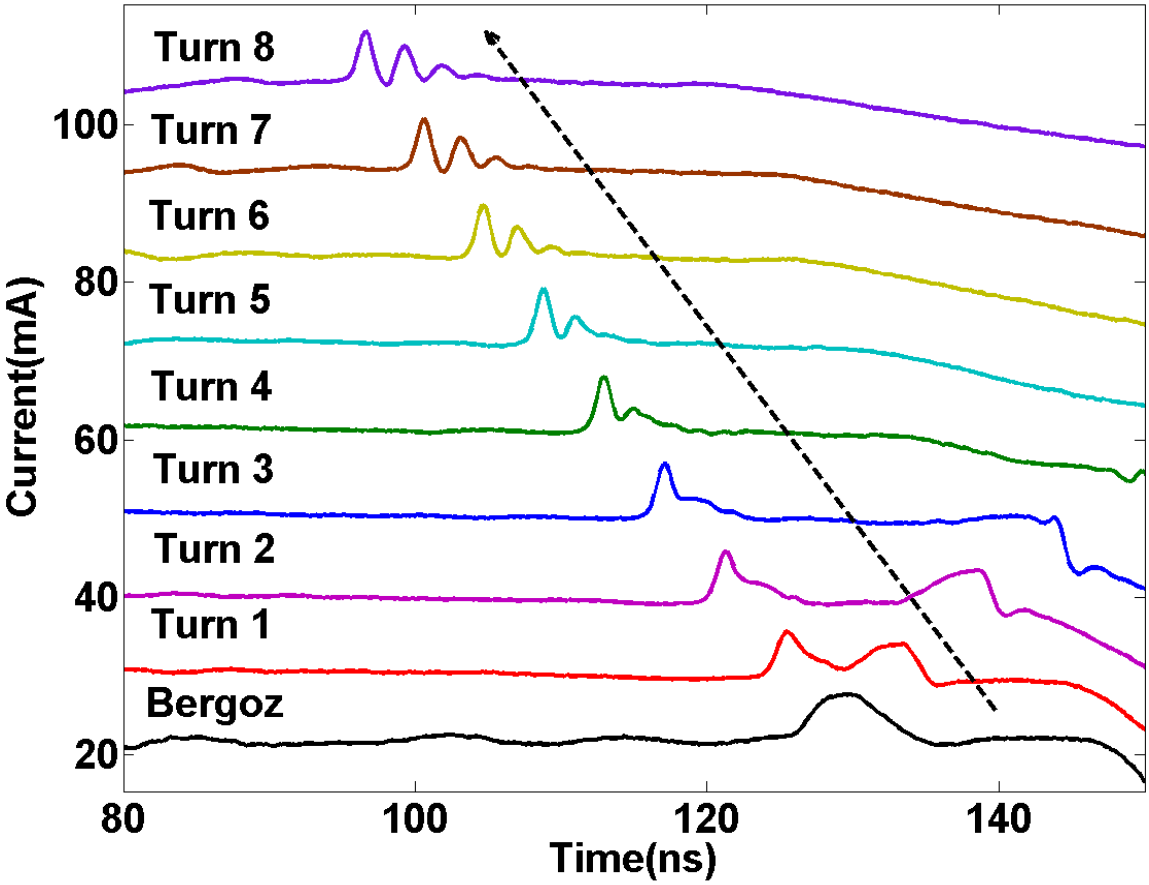

Figure 4.8: Beam evolution for 22mA, 25% perturbation turn by turn.

Then η becomes a perturbation profile with peak amplitude of 0.25, i.e., the ε defined in Eqn. 2.48 is about 0.25.

Assuming the beam radius r_w~1cm, for space charge dominated beam,

$$g_0 = 2\ln\left(\frac{r_w}{r_b}\right) \approx 2\ln\left(\frac{1}{2.54}\right) = 1.86,$$

From [38],

$$g_2 = \frac{1}{8}\left[4\left(1-\frac{r_b^2}{r_w^2}\right)-3\frac{r_b^2}{r_w^2}\ln\left(\frac{r_w^2}{r_b^2}\right)\right] \tag{4.1}$$

Therefore, $g_2 \approx \frac{1}{8}\left[4\left(1-\frac{1}{2.54^2}\right)-3\times\frac{1}{2.54^2}\ln\left(2.54^2\right)\right] = 0.31$

Sound speed $v_{b0} = \sqrt{\frac{\mathrm{q}g_0\lambda_0}{4\pi\varepsilon_0\gamma_0^5\mathrm{m}}} \approx 1\times10^6 m/s$

From Sec. 2.4, we have $v_{b2} = v_{b0}\sqrt{\frac{g_2}{g_0}} = 4.08\times10^5 m/s$

Thus we have the normalized variables as

$$U = \frac{v}{v_{b0}} = \frac{v}{10^6 m/s},\ T = \frac{v_{b0}^2}{v_{b2}}\frac{t}{r_w} = \frac{t}{10.4ns}\ ,\ Z = \frac{v_{b0}}{v_{b2}}\frac{z}{r_w} = \frac{z}{1.04cm} \tag{4.2}$$

The pulse width 5.4 ns (32.4cm):

$$\Delta Z = 32.4/1.04 = 31.15 \tag{4.3}$$

$$\xi = \varepsilon^{1/2}\left(Z-T\right) = 0.5\left(\frac{z}{1.04cm}-\frac{t}{10.4ns}\right) \tag{4.4}$$

$$\tau = \varepsilon^{3/2}T = 0.125\times\frac{t}{10.4ns} = \frac{t}{83.2ns} \tag{4.5}$$

Applying the KdV integration code in Appendix C, we observe the beam propagation under Eqn. 2.57 from distance $\zeta \in (-\pi,\pi)$ within a time duration τ of 0.01 with the initial condition in Fig.4.9.a, which can be scaled to the Bergoz profile in Fig. 4.8.

As shown in Fig. 4.9.a, the perturbation pulse is scaled to a peak amplitude of $\eta^{(1)} = 140$, and width of $\Delta\xi = 1.324$.

Based on the scaling method in Eqn. (2.59): $\xi = a*\xi$; $\tau = b*\tilde{}$; $\eta = c*\eta$

where $a^2 c = 1$ and $(\frac{b}{a^3}) = 1$

Since $\eta = \varepsilon\eta^{(1)} = 0.25$, $\eta^{(1)} = 1$. Therefore, $c = \eta^{(1)} / \eta^{(1)} = 140$

Pulse width $\Delta\zeta = 0.5\Delta Z = 15.58$, then **a=1.324/15.58=0.085**, which satisfies $a^2c=1$. Otherwise, modify either $\eta^{(1)}$ or $\Delta\xi$ in the integration code accordingly. Meanwhile, **b=a^3=0.00061**

Therefore, we can compare the soliton formation between the experimental results and the KdV model for the same turn. The distance from the cathode to RC10 (wall current monitor) is 0.64m+7.67m=8.31m, equaling time 8.31/6e7=1.385e-7 s=138.5 ns for the first turn, and it takes 197 ns per turn thereafter.

The KdV equation integration results are shown in Fig. 4.9.b and 4.9.c. After scaling the parameters, the soliton amplitude and width are compared with the experimental results in Table 4.1. Meanwhile, a direct comparison of the soliton wave train plots is shown in Fig. 4.10.

A reasonable agreement is achieved. The discrepancy could be caused by the beam loss that is not counted in the KdV equation integration (It's counted in the final data process as shown in Note 5 of Table 4.1 though). The g_2 factor also plays a role in the longitudinal dynamics. When the beam perturbation steepens and narrows down, g_2 no longer stays a constant and thus affects the beam normalization (Eqn. 4.2). The dispersion effect grows as the pulse narrows down, then the 1st and the 2nd sub-pulses separate faster, while during the KdV equation integration, there's no modification of the dispersion term, which leads to a slower sub-pulses separation rate, as demonstrated in Fig. 4.10. Other than that, the soliton widths and amplitudes are almost perfectly matched between theory and experiment.

Table 4.1: Compare experimental results with KdV model for the 5th and 7th turn

Turn # n	Experiment					KdV Model (Simulation)					KdV Model w/ Units (Derivation)			
	Time t (ns)	Amplitude n		Width (ns)		Time τ	Amplitude $\eta^{(1)}$		Width Δξ		Amplitude η'		Width Δξ' (ns)	
		1st	2nd	1st	2nd		1st	2nd	1st	2nd	1st	2nd	1st	2nd
5	926.5	44%	22%	1.137	N/A	0.0068	226.8	140.3	0.27	N/A	33%	21%	1.1	N/A
7	1320.5	**43%**	**26%**	**1.086**	**1.2**	0.0097	241.2	161.3	0.23	0.27	**38%**	**25%**	**0.94**	**1.1**

Note:

1. Time in experiment t=138.5+(n-1)*197;
2. Time in KdV model τ=t/83.2*b=t*7.33e-6;
3. 1st and 2nd represent the two subpulses in the soliton wave train;
4. Initial fast wave pulse amplitude in experiment n=ε/2~15%. The initial profile splits into fast wave and slow wave, with each slightly above half of the initial condition (25%) due to the pulse widening from the cathode to Bergoz [Fig. 5.3.a];
5. Amplitude in KdV model w/ units $\eta^{(1)} = c\eta^{(1)} = c\frac{\eta'}{0.15}$, considering beam loss, $\eta' = 0.15 \times \frac{\eta^{(1)}}{c} \times \frac{I_0}{I_n}$, where I_0=22mA, I_n is the curent of the Nth turn;
6. Pulse width in KdV model w/ units Δξ=0.5* Δξ'*6/1.04*a=0.245* Δξ' therefore Δξ' = Δξ/0.245

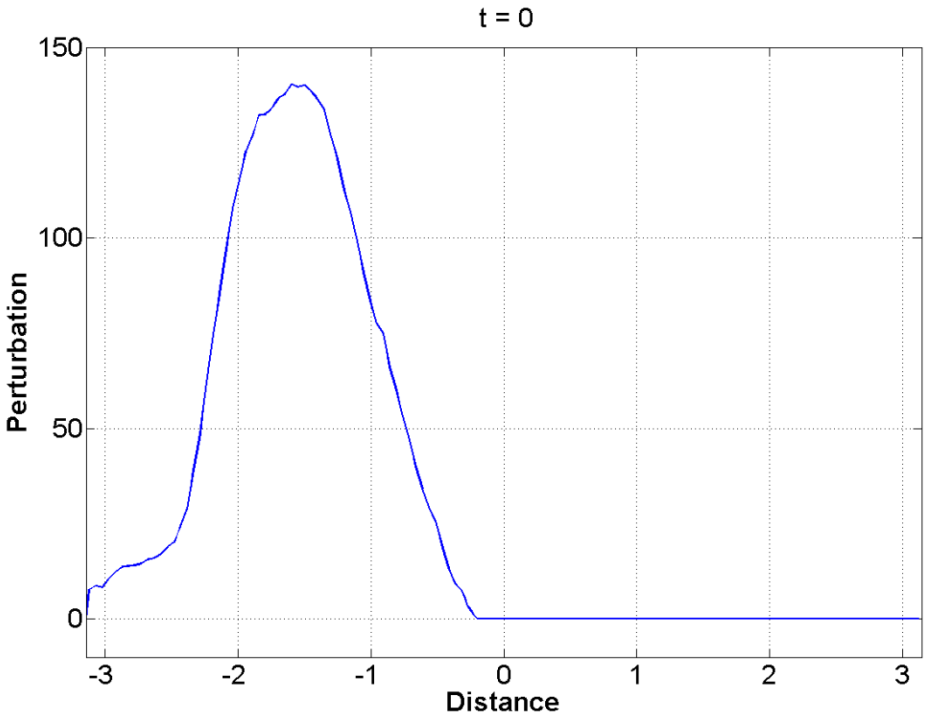

Figure 4.9.a: Intial condition imported in the KdV model before scaling to lab parameters.

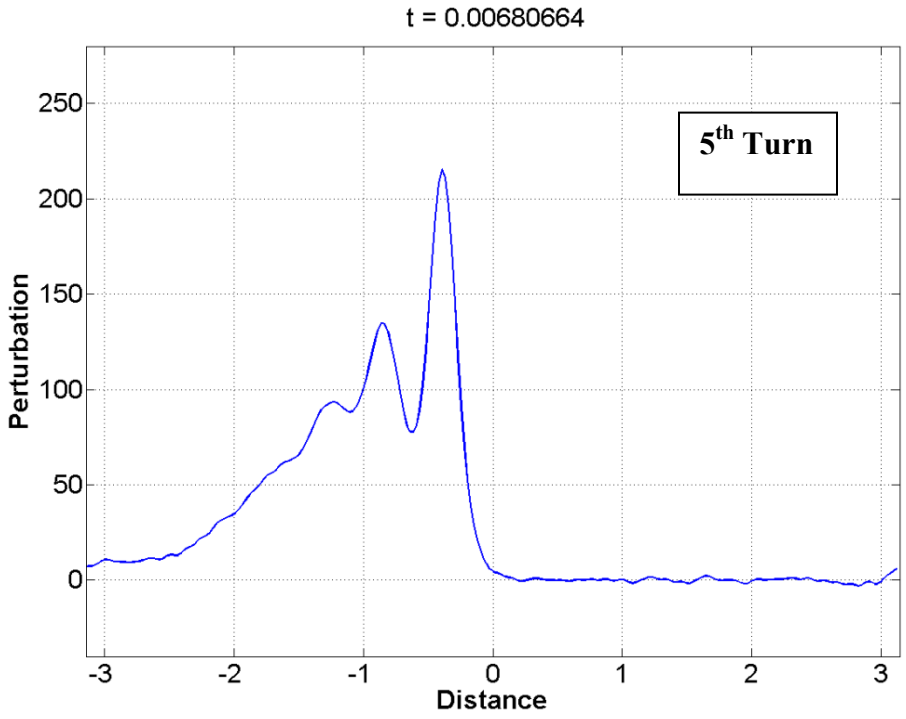

Figure 4.9.b: Beam profile at the 5th turn in the KdV model before scaling to lab parameters.

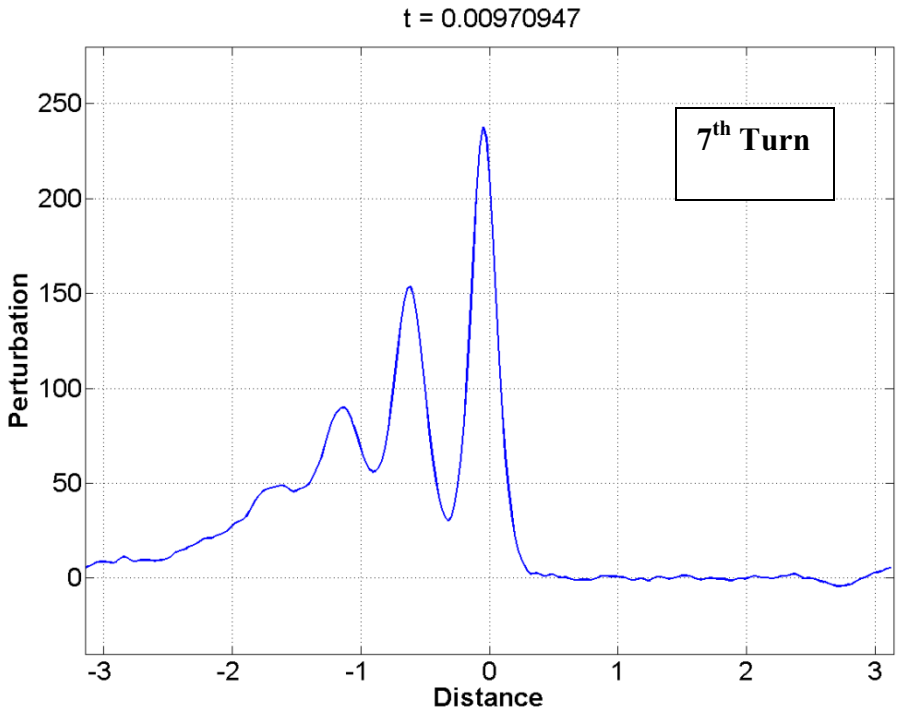

Figure 4.9.c: Beam profile at the 7th turn in the KdV model before scaling to lab parameters.

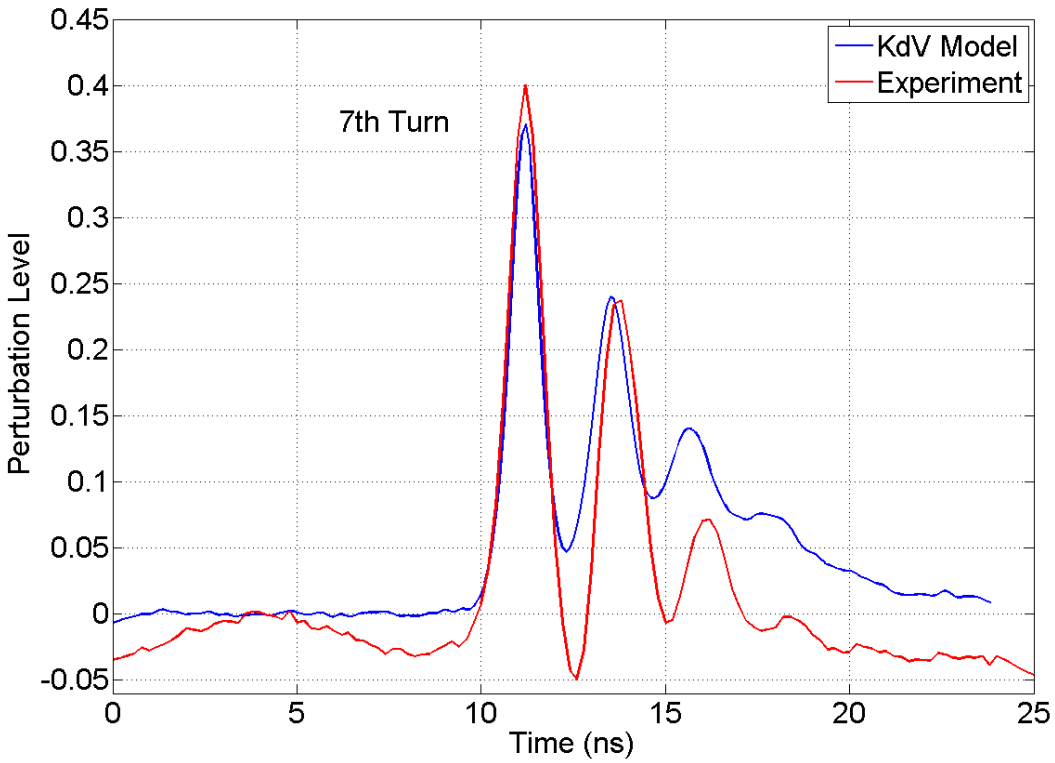

Figure 4.10: Soliton wave train comparison between experiments and theory for the 7th turn.

4.4 Soliton Dependence on Beam Parameters

In this section, we are interested in addressing the conditions under which solitary waves will be generated and how their evolution depends on beam parameters. We therefore systematically vary the beam current, perturbation strength and width.

In Fig. 4.11, we compare solitary waves for two different beam currents, 23mA vs. 30mA, keeping the same pulse width (about 5 ns) and relative perturbation level (20%). The 30 mA pulse steepens faster and more sub-pulses are generated. We expect the faster propagation, since, from the linear theory at least, the sound speed is proportional to the square root of the line charge density (see Eqn. 2.6). We observed that, if the beam current is below certain threshold value (around 20 mA in UMER), then no solitons could be generated.

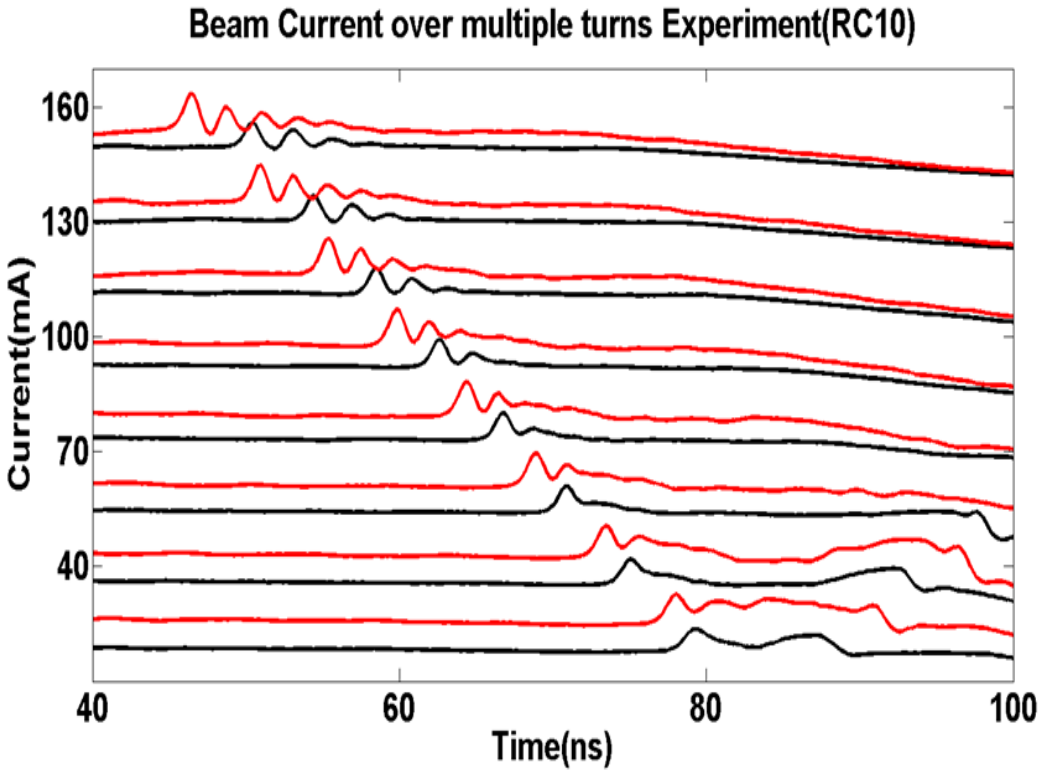

Figure 4.11: Turn-by-turn plot comparison between 23 mA beam (black) and 30 mA beam (red), both with 20% perturbation and 5 ns width.

Next, we studied the perturbation amplitude dependence. As can be seen from Fig. 4.12, different perturbation levels affect the result. The 50% perturbation case propagates faster and gives many more sub-pulses compared with the 20% perturbation case. It is consistent with the relation that a stronger pulse leads to a faster propagation speed.

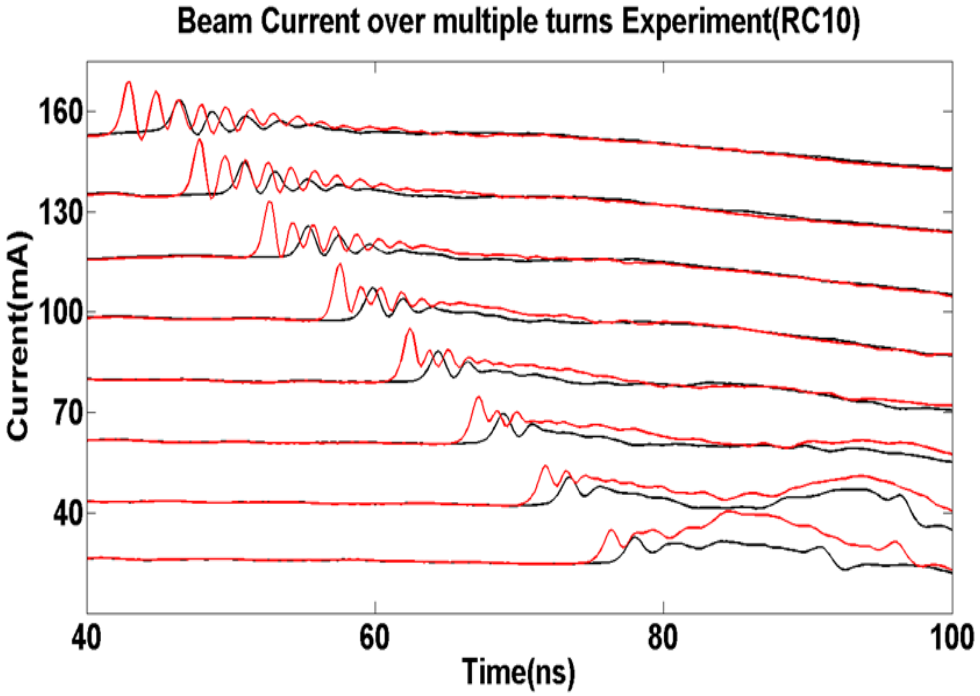

Figure 4.12: Turn-by-turn plot comparison between a 20% perturbation (black) and a 50% perturbation (red), both with 30mA main beam and 8 ns width.

In Fig. 4.13, we show different perturbation pulse widths, one 5.6 ns, the other 7.6 ns. Since they have the same beam current and perturbation level, their sound speed is very close. However, the wider pulse results in more sub-pulses, which can be explained by a diminished dispersive effect. Also, each of the sub-pulses generated from the wider pulse are stronger than the ones from the narrower pulse.

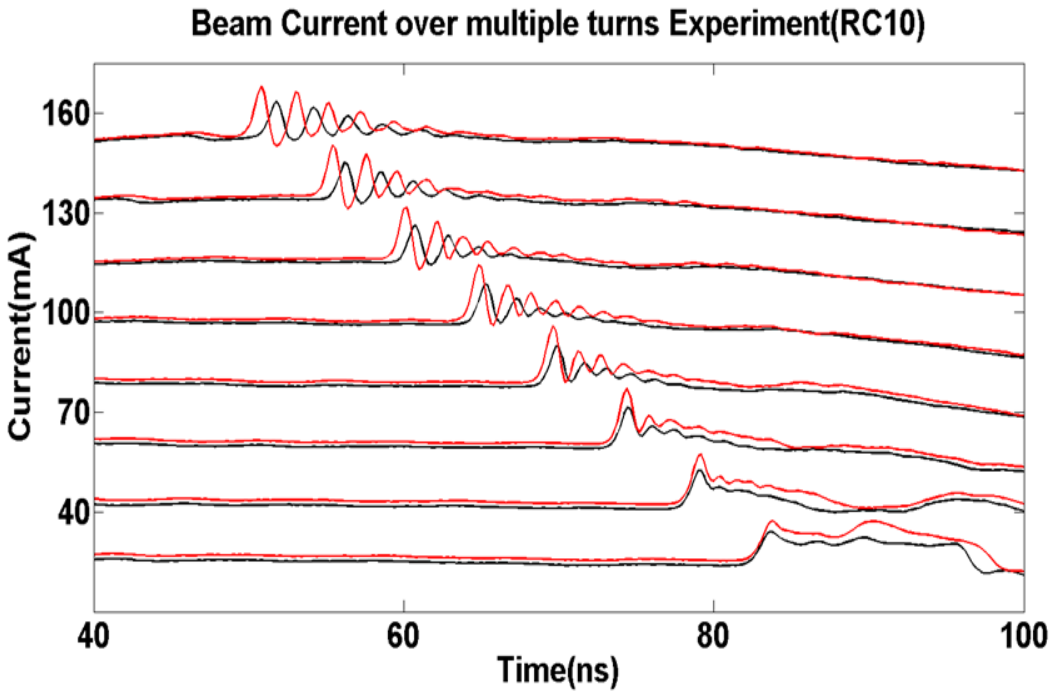

Figure 4.13: Turn-by-turn plot comparison between a 6 ns wide perturbation (black) and an 8 ns wide perturbation (red), both with a 30 mA beam and a 50% perturbation amplitude.

All the results of the soliton dependence experiments agree qualitatively with the theory. Additional studies are needed in the future to permit a more quantitative analysis.

4.5 Soliton Interactions and Two-Perturbation Experiments

In the previous discussion, we have shown that the large amplitude waves we generated satisfy the properties of a solitary wave. In order to demonstrate that they are solitons, we need to further show that they behave like particles, i.e., they retain their properties after mutual interactions, or "collisions", except for a phase shift [50]. Experiments with two perturbations are conducted. I use two lasers to generate perturbations on both sides of the beam, and let the fast wave from one perturbation approach the slow wave from the other and interact with it [Fig. 4.14]. To allow enough time for the two perturbations to propagate and break before they collide, I extend the beam duration from 100 to 140 ns.

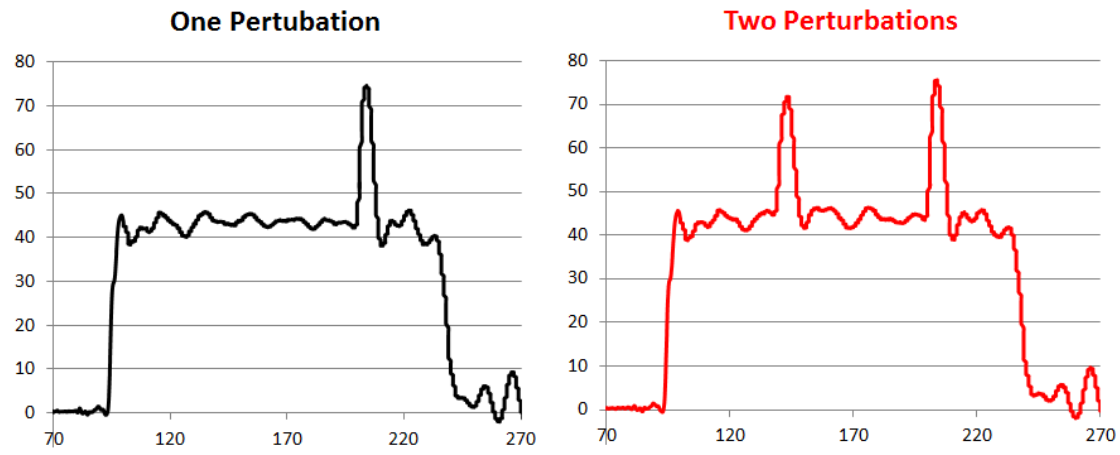

Fig. 4.14: The initial conditions for one perturbation (left) and two perturbations (right), with identical beam background (40 mA), and a same perturbation on the right edge.

Fig. 4.15 illustrates the evolution of two cases: a single 50% perturbation on a 30 mA beam (black), and the same perturbation on the same beam with the addition of another 50% perturbation on the opposite side (red). The black curve shows the fast wave of the perturbation on the right steepening and forming a soliton wave train, as above. The red curve shows the same soliton wave train going through the wave train formed by the slow wave of the perturbation initially on the left. The fact that the two curves are nearly identical for the fast wave past the interaction point is strong evidence that it is a soliton.

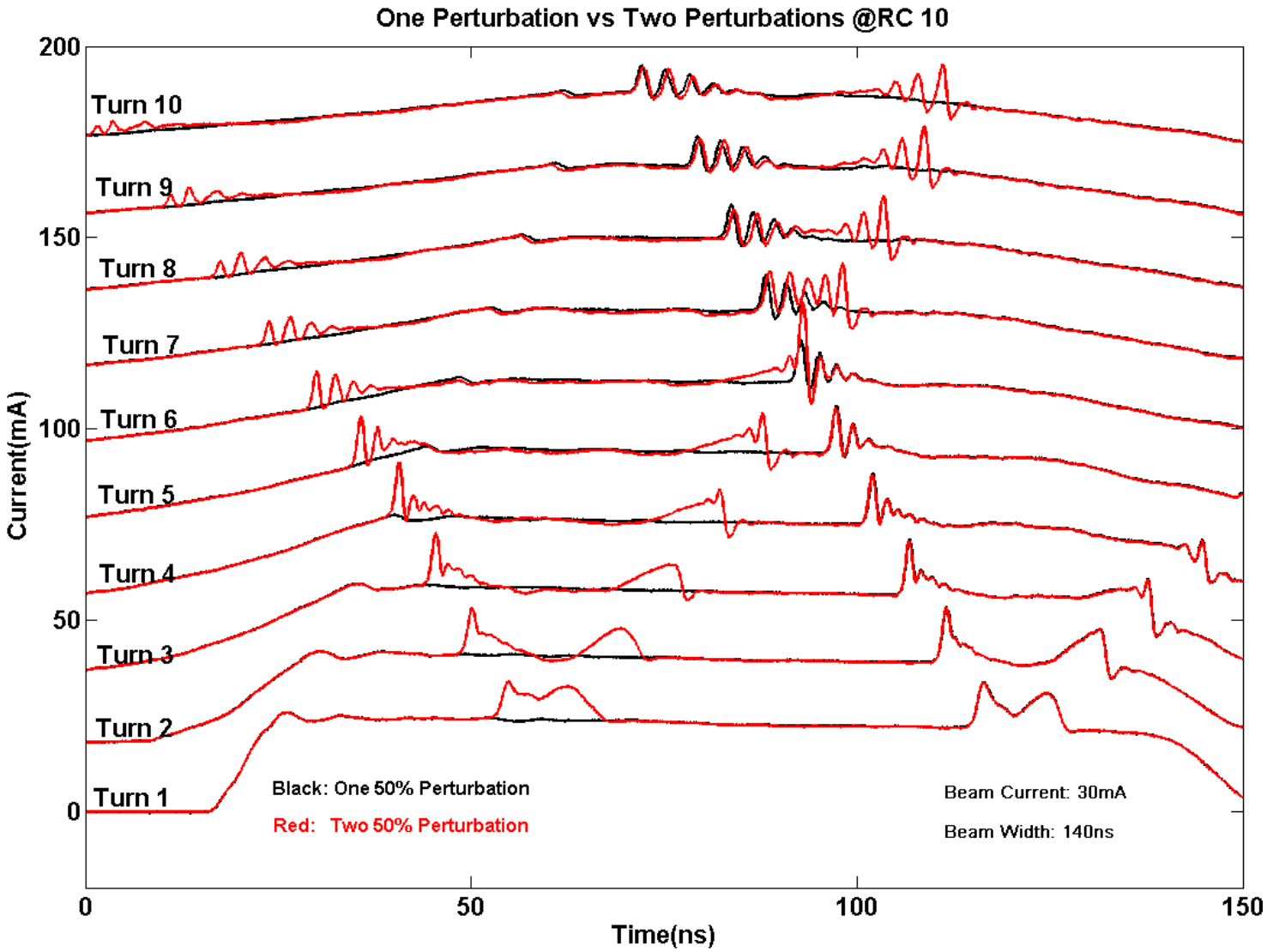

Fig. 4.15: Comparison of two-perturbation experiment and one-perturbation experiment. The fast wave of the right perturbation interact with the slow wave of the left perturbation (red), is compared with the fast wave propagation of the one perturbation case (black).

Another two-pertubation experiment is to introduce the two perturbations on the same edge of the beam, and observe the solitons travel in the same direction. A stronger sub-pulse could catch up with a soliton with shorter amplitude and then interact. This experiment provides an opportunity to investigate soliton interaction for a longer period compared with two solitons passing through each other in opposite direction. However, it requires a much longer beam medium for soliton propagation in such an experiment. Unfortunately, the setup in UMER doesn't provide a long enough thermionic beam and the perturbations would step off the beam edge before the soltions recover from the interaction. Simulation using Particle-in-Cell code WARP is performed for this experiment in Sec. 5.2 in Chapter 5.

4.6 Improved Beam Injection and Steering Solution

The thermionic beam use for the soliton experiments (~30mA beam in temperature limited mode, through 80 mA aperture) suffers the problem of beam loss as shown in Fig. 4.7, which complicates the longitudinal beam dynamics. The UMER lab has been consistently working on producing beams with less loss and longer propagation distance.

A major improvement is tracing the short term beam losses to Eddy currents from the pulsed injection quadrupole [51]. This problem is not discovered until 2013 since UMER started its operation. We fix this by delaying injection of the beam until the Eddy currents have died down. The beam loss is significantly reduced after the injection. See the comparison between Fig. 4.16.a and 4.16.b. The 10% beam loss in the first turn is completely gone.

The beam steering solution is also crucial to beam optimization. A steering solution for the 30 mA beam in temperature limited mode is calculated using the response matrix technique

[52], and the beam orbit is optimized. The beam loss control for the first two turns is greatly improved.

The other major factor causing beam loss is the beam mismatch. It is more difficult to match the beam in the temperature limited mode, where we observe a random transverse beam distribution. The optimized matching solution from [53] is applied, however some assumptions made on beam radius and emittance may not be accurate.

Under the same initial condition (23mA, 50% perturbation), with improved beam injection and steering solutions, we almost eliminate the beam loss in the first two turns, while there is almost 20% in the old experiment. However, the beam loss increases dramatically from the 3rd turn and the beam currents in the two experiments are at similar level after 6 turns in the ring.

The beam loss requires further investigation. It could be due to the beam matching solution since a small mismatch can result in large-amplitude envelope oscillations (then beam scraping) in later turns while it doesn't build up in early turns [27].

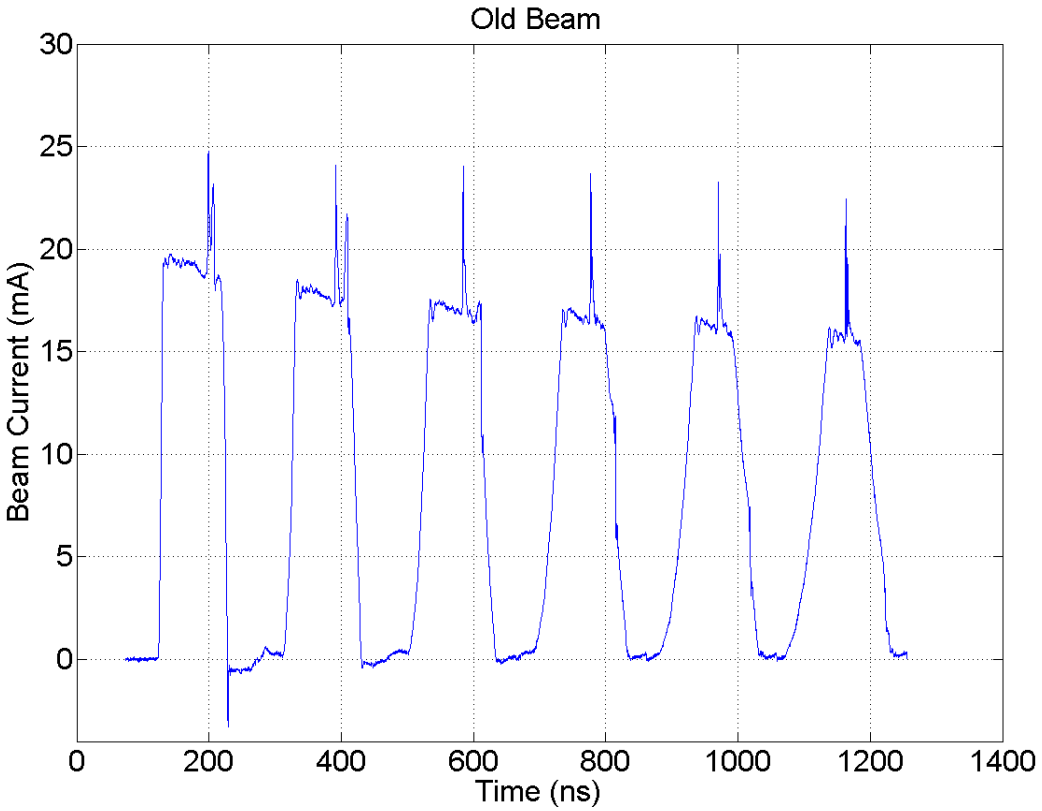

Figure 4.16.a: The 22mA initial beam pulse evolution for 6 turns with old beam solution.

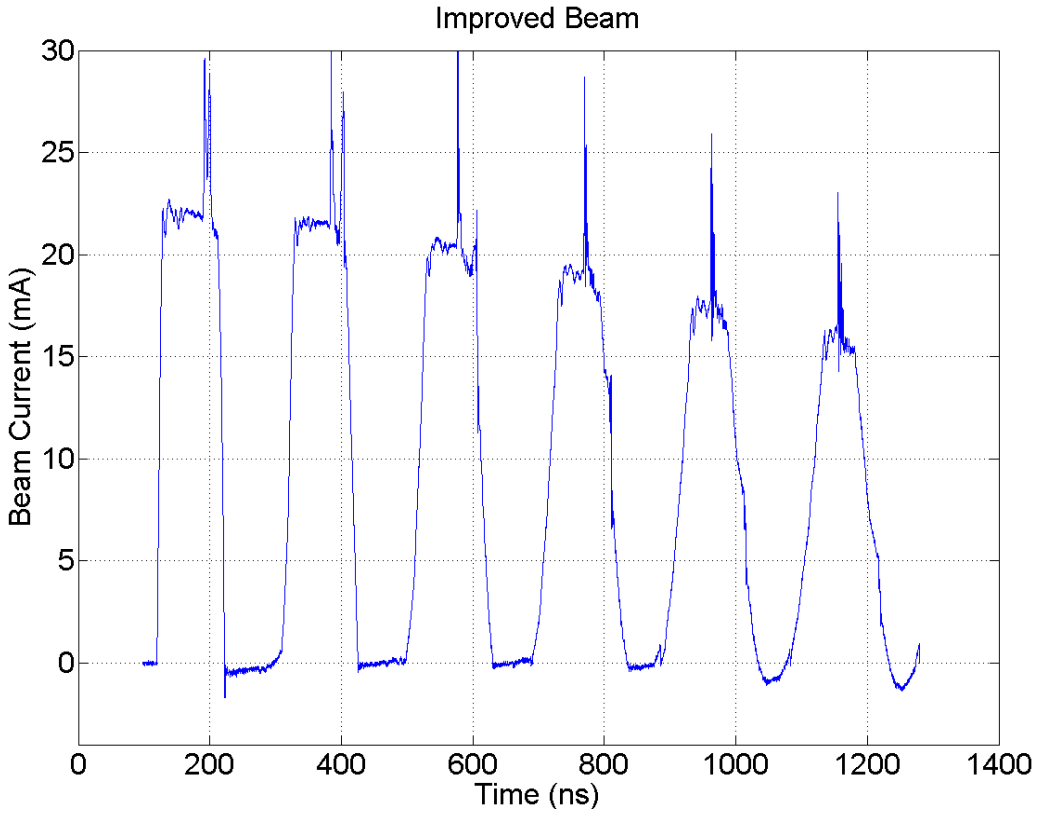

Figure 4.16.b: The 22mA initial beam pulse evolution for 6 turns with improved beam solution.

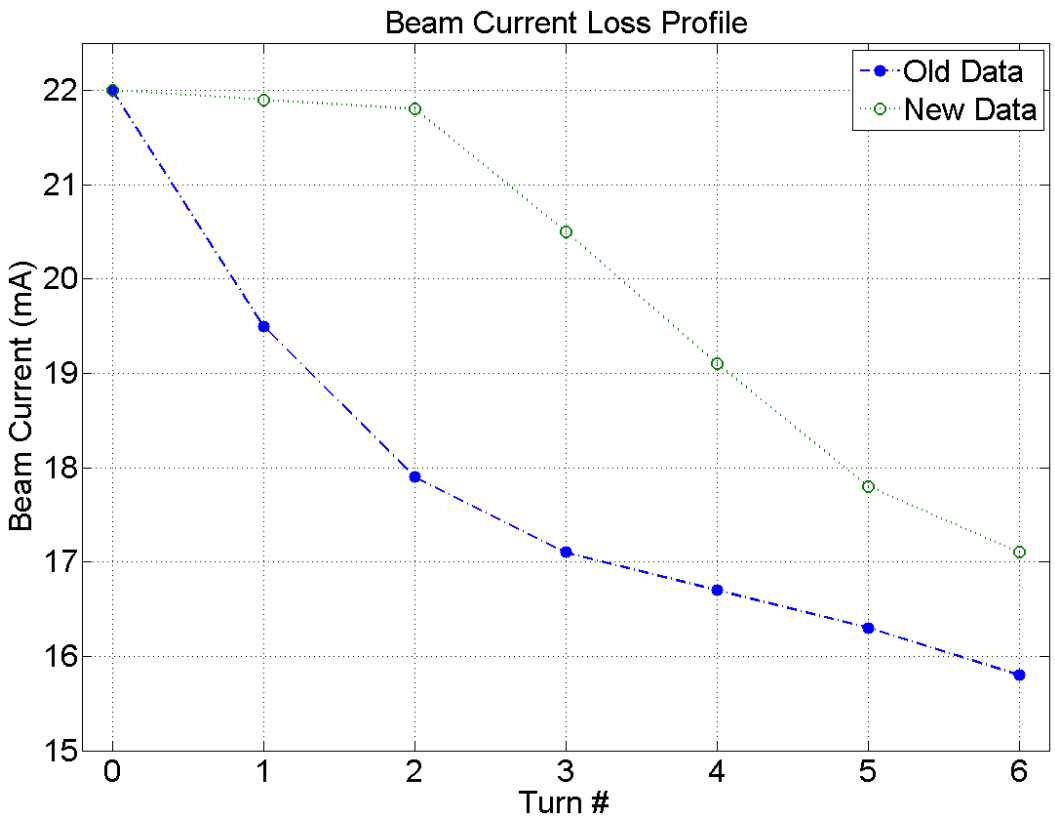

Figure 4.17: Comparison of beam loss profiles before and after beam improvement.

4.7 Solitons from Velocity Perturbation

As shown in chapter 3, the induction cell module can introduce velocity perturbations on the thermionic beam bunch and then generate space charge waves. The fast wave and slow wave have a different polarity [Fig. 3.13]. With larger velocity perturbations, we also observed soliton formation from the 7^{th} turn as shown in Figure 4.18. Two soliton wave trains are of opposite polarity.

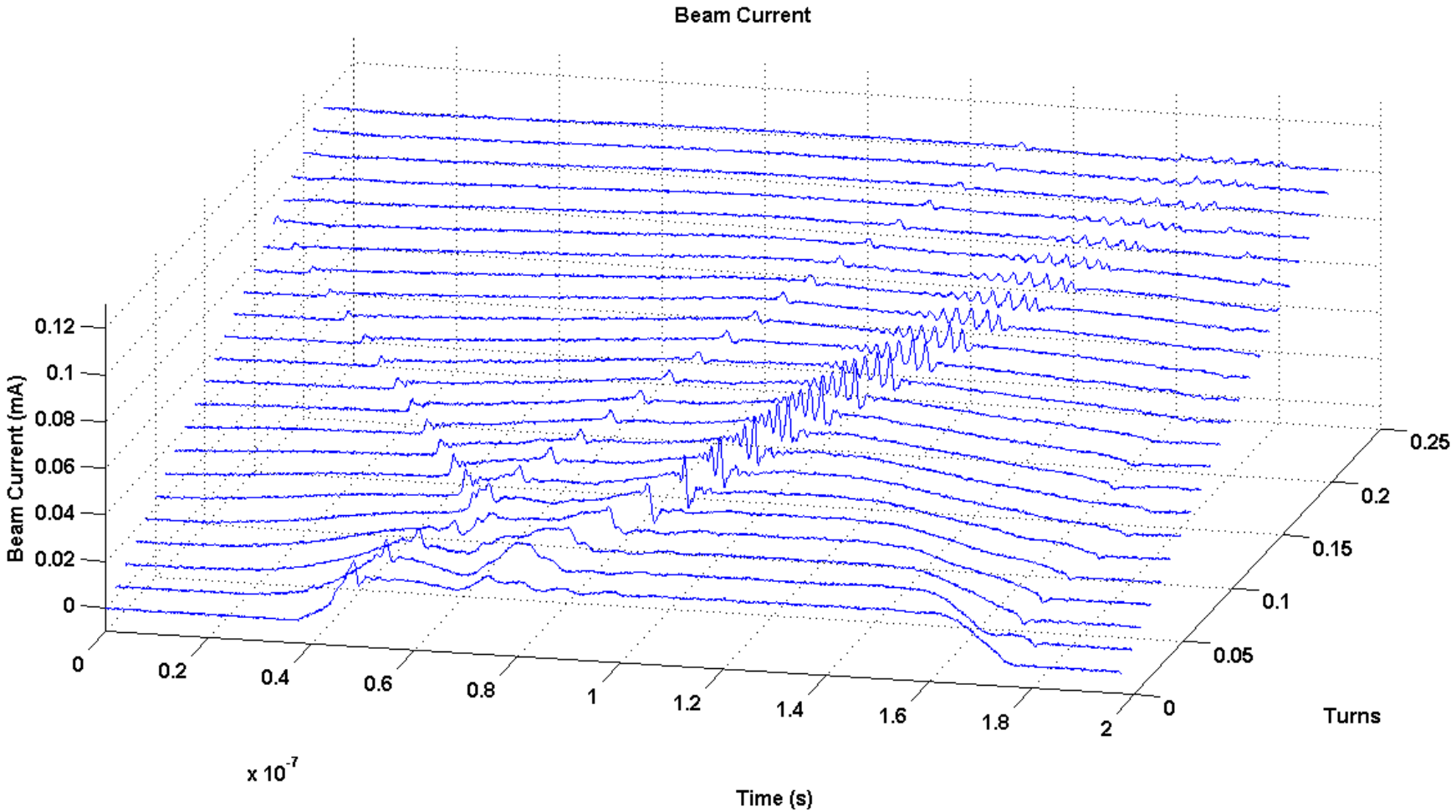

Fig. 4.18: Soliton wave train formation from a large initial velocity perturbation generated by induction cell, courtesy to B. Beaudoin.

The induction cell not only provides an alternative for generating solitons on electron beam, but also a technique for improving the soliton experiment. From Sec.4.6, we learn the difficulties for an optimized solution for a temperature-limited mode beam. The induction cell can modulate the beam in space charge dominated mode since the perturbation is introduced inside the ring, while for photoemission by laser, occurring at the cathode beam source, has to be operated in the temperature limited mode due to the current limitation by the Child-Langmiur law. The perturbation level can be easily modified by the electric pulse from the induction cell. The beam steering and matching is easier to optimize in space charge dominated region so that we can achieve less beam loss. Meanwhile, there is less beam noise compared with the temperature limited mode where the cathode has a triode I-V characteristic [21].

In addition, we can generate multiple velocity perturbations, and they can occur even at different turns respectively, which enable us to study more complicated longitudinal beam dynamics.

The induction cell technique is limited by the perturbation width. The minimum width we can obtain is ~8 ns, while the perturbation width from photoemission be can less than 5 ns. To narrow down the velocity perturbation width, a broader amplification band for the induction cell is needed.

4.8 Summary

We have shown the formation of soliton wave trains in electron beam, by both experiments and theory. The data analysis is consistent with soliton properties. We also explored the soliton dependence on beam current, perturbation strength and width. Improved beam injection and steering solutions are discussed. Compared to the density soliton formation, velocity solitons are also achievable by modulations from the induction cell module.

Chapter 5: Simulation of Soliton Formation and Spacing

In this chapter, we show the simulation results of solitons in electron beams. First we simulate the same beam with large perturbations as the experiments in Chapter 3, and perform a detailed comparison and data analysis. Then we do beam simulations that are difficult to investigate by experiments, such as two-soliton interaction with same propagation direction. We also study the dependence of soliton spacing, a potential topic for new radiation sources, by changing beam parameters which are hard to modify in experiments.

5.1 Soliton Simulation and Comparison with Experiments

In this section, we present the results of simulations and compare them with the experiments. We use the R-Z model of the WARP particle-in-cell (PIC) code [54] to simulate the evolution of the beam, including the perturbation. Take the 22mA 25% perturbation case for example. We use uniform transverse focusing to represent the FODO lattice, choosing a focusing strength $\kappa = 13.33m^{-2}$ to give us the same phase advance per period (see Table 3.1). We load an initial distribution with the same measured current profile at the Bergoz. Transversely, we use a semi-Gaussian distribution, which is uniform in space and Gaussian in velocity space with uniform temperature. The initial transverse beam radius is chosen to be 9.5 mm with zero slope so it will be matched to the lattice for the beam parameters. The kinetic energy is 10 keV with a longitudinal thermal spread of 5e4 m/s. The thermal spread used is somewhat higher than what we expect for the UMER beam, mostly for the purpose of suppressing the gridding instability. However it cannot be too high or else the thermal spread will

wash out the soliton structure. We found the simulation converges for the following numerical settings 4,000,000 macroparticles; a time step of 1 ns; 64 cells in R direction and 2048 cells in z direction. The grid size is 0.0254 m in R and 11.52 m in z.

Due to the beam loss in experiment, the sound speed becomes slower and so is the edge erosion rate, which has to be counted in simulation. Variable top.pgoup.sw describes the species weight (# of real particles per simulation particle). A beam loss is set by decreasing top.pgoup.sw uniformly turn by turn. When doing the calculation of beam loss from experimental data, we need to count in the inductance compensation for the current. Check ref. [55] for details. Otherwise, there will be more beam loss than it actually is.

For more numerical settings and a description of the WARP code, see ref. [56].

The initial condition (beam density profile) is rather tricky. We start with the beam current profile (assuming velocity profile uniform, thus density $\propto$ current since $I = v\lambda$) measured at Bergoz, and barely get any agreement on the pulse propagation. As can been seen in fig. 5.1-5.2, with the same initial profile, the fast and slow wave in experiment (red) is much stronger than those in simulation (blue), and there's discrepancy on the right beam edge.

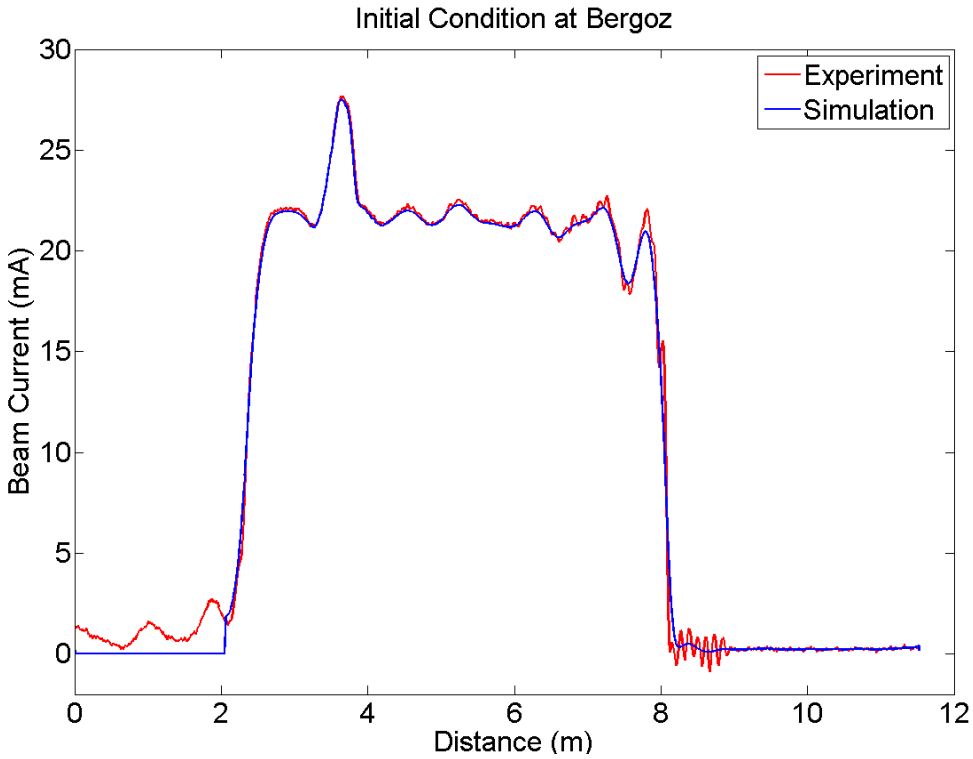

Fig. 5.1: the measured initial condition at Bergoz (red) and its smoothed profile that's imported into simulation (blue).

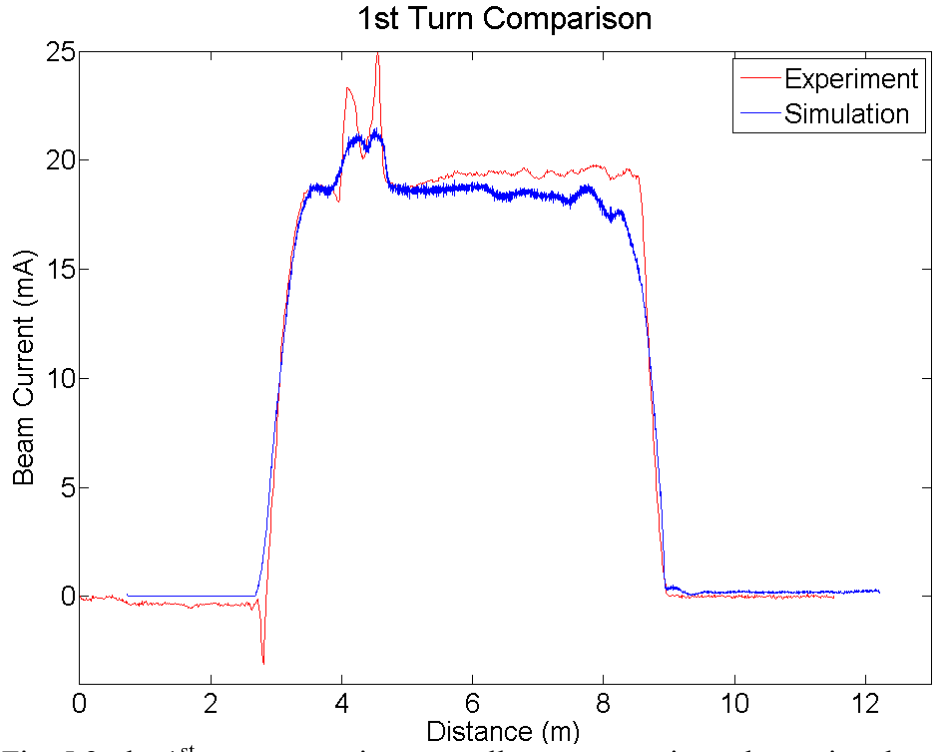

Fig. 5.2: the 1st turn comparison at wall current monitor when using the measured Bergoz current profile as the input for simulation at cathode.

Therefore, it's NOT accurate to use the Bergoz current profile as the beam right out of cathode, which could be explained from two aspects. First, there's Pulse widening during 64cm propagation. According to eqn (3.4) of [19],

$$Cs = \frac{\delta t}{2\Delta z} v^2 \tag{5.1}$$

Where Cs is the sound speed, δt is the time difference between the fast and slow wave, Δz is the distance the beam travelled in lab frame, and v is beam velocity.

Then we obtain $\delta t = \frac{2\Delta z Cs}{v^2} \sim$ 2*0.64*1.25e6/(6e7)^2=0.44ns, which means that the pulse widens about 0.44ns from cathode to Bergoz.

Secondly, after 64cm propagation, there comes a velocity modulation on the beam, which also contributes to the current profile, and makes it even wider. In other words, the density profile for simulation input at the cathode should be narrower. Fig. 5.3 (a-d) gives a numerical example of how energy (velocity) perturbation affects the beam pulse.

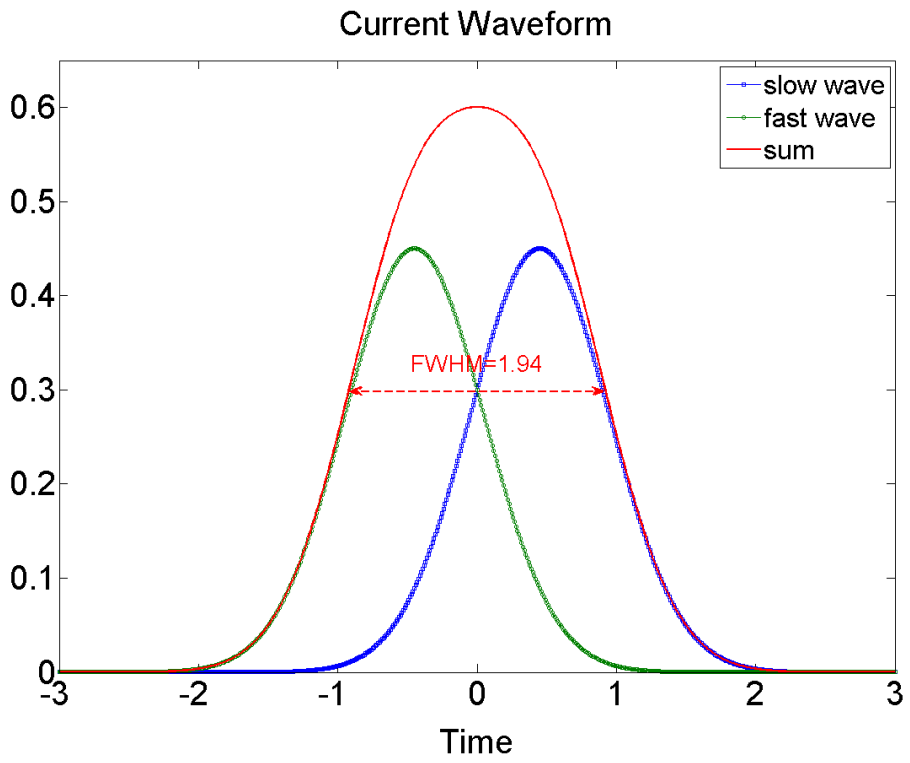

Fig. 5.3.a: A numerical example of two current waveforms of Gaussian and their sum at Bergoz.

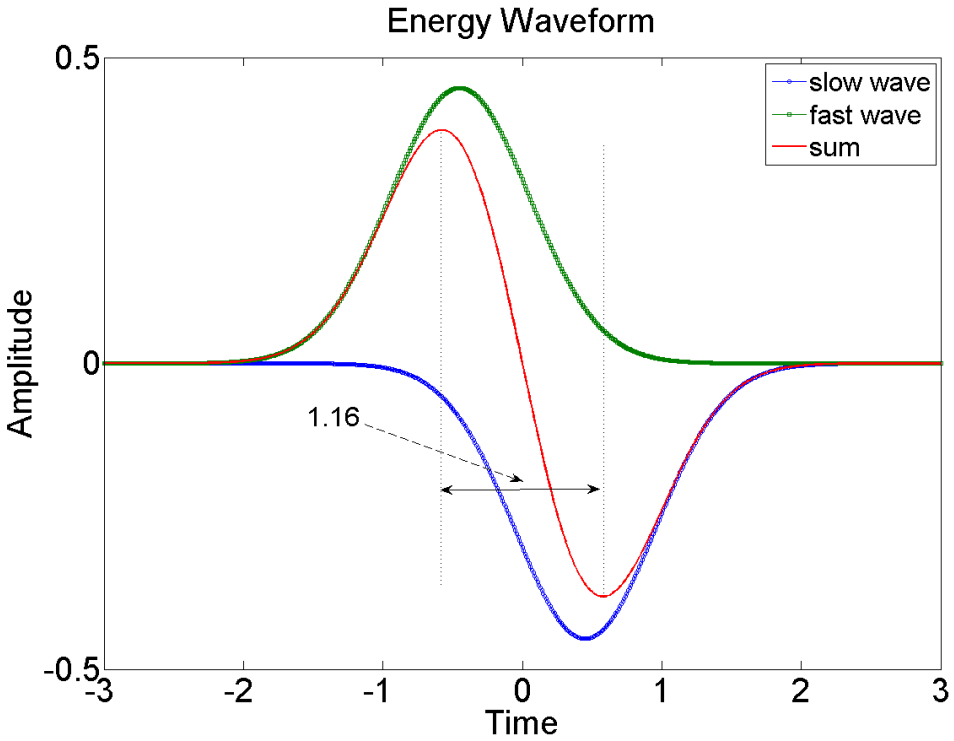

Fig. 5.3.b: Switch the polarity of the slow wave, to get the energy waveforms at Bergoz.

Adjust the base level of the current and energy waveform. Say we have 20% current perturbation, set the base beam at 3 since the beam peak is 0.6 (arbitrary unit) in Fig. 5.3. Increase the energy profile amplitude by a factor of 10, we get 4% energy perturbation (2% velocity perturbation). Dividing the current waveform by the energy waveform, we get the density profile [Fig. 5.3.c-d]. Compared with Fig. 5.3.a, the density profile is narrower than the current profile. Also, the more energy perturbation is, the narrower the width of the density profile.

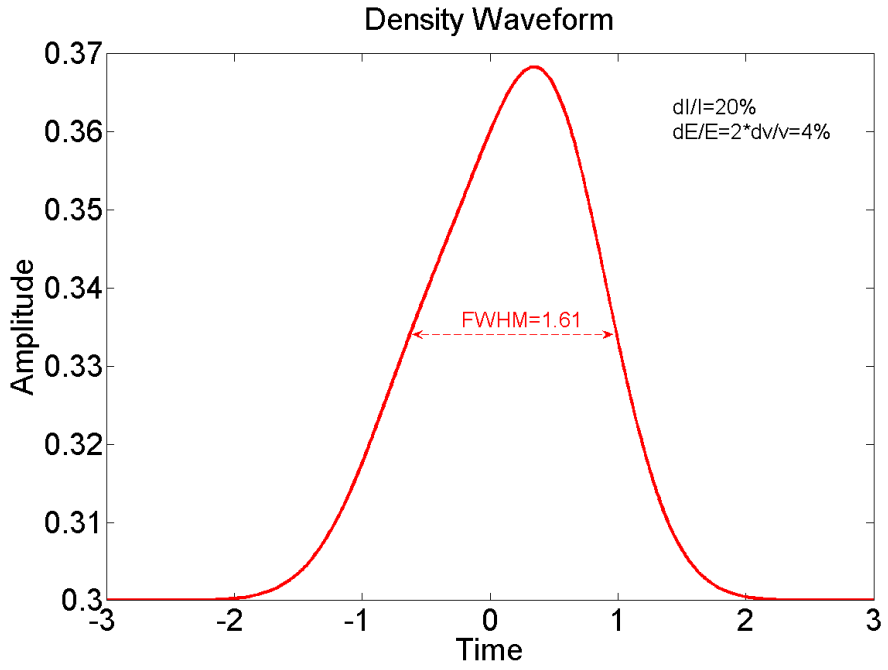

Fig. 5.3.c: A numerical example of the density profile when dI/I=20%, dv/v=2%.

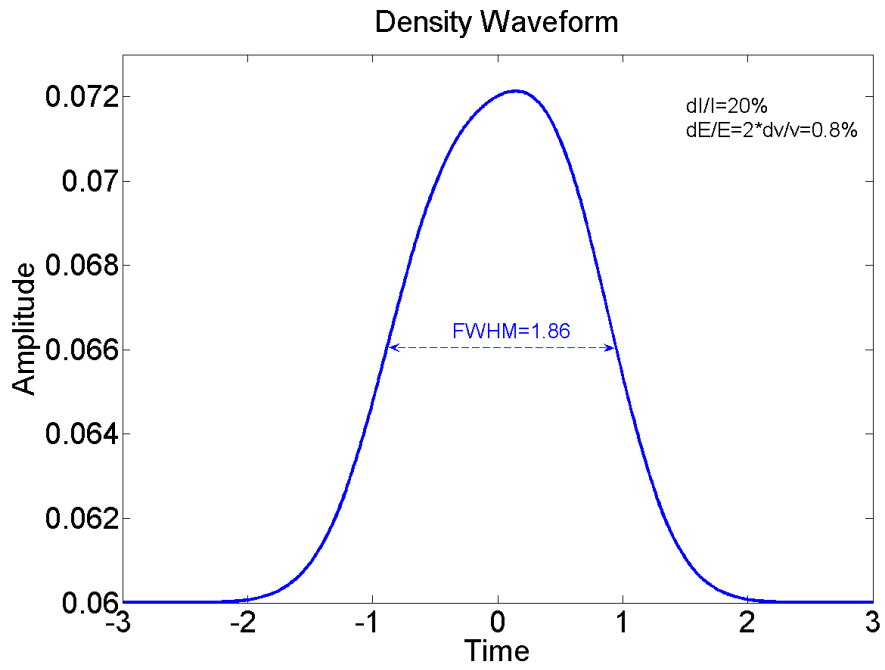

Fig. 5.3.d: A numerical example of the density profile when dI/I=20%, dv/v=0.4%.

Therefore, we should either change the initial profile into some stronger/narrower perturbations, or still use the Bergoz profile, but add the velocity modulation into the code. We resort to starting the simulation from the cathode with an adjusted current profile (see Fig. 5.4).

In Fig. 5.4, the initial condition is assumed to be a rectangular beam with a 11mA 3.7ns wide pulse atop, compared with ~6mA 5ns perturbation in Bergoz. The intial condition adjustment leads to a good agreement between simulation and experiment at the wall current monitor. Fig. 5.5 shows the 1^{st}, 2^{nd}, 5^{th} and 8^{th} turns comparison.

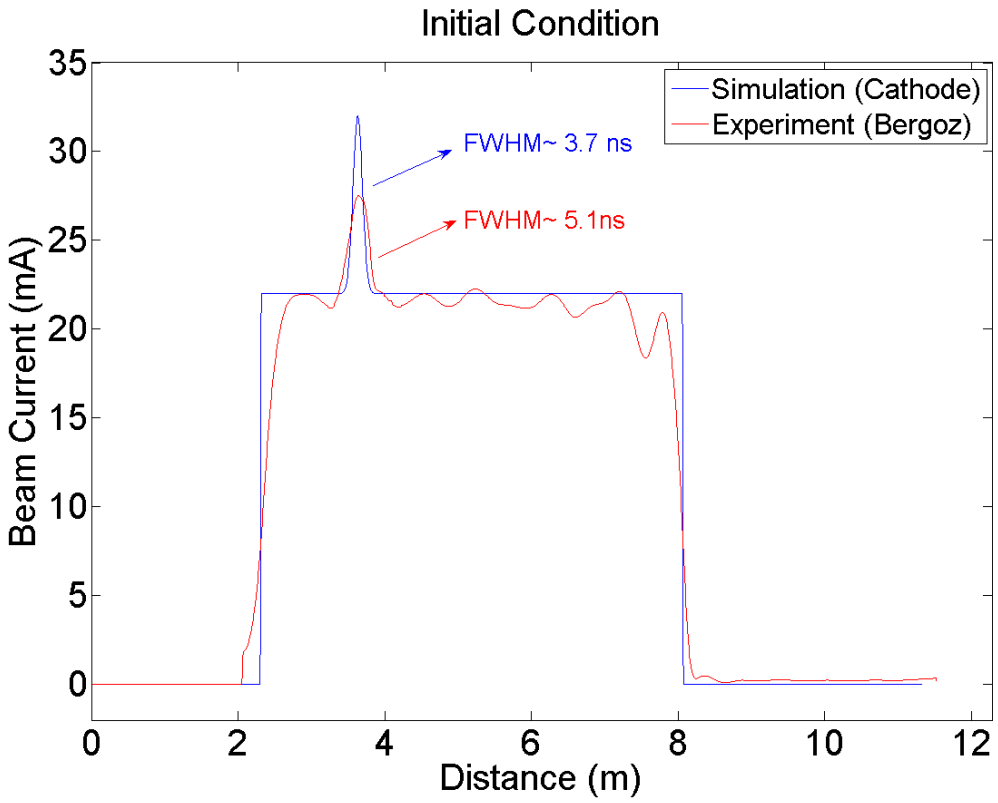

Fig. 5.4: Initial condition measured at Bergoz (red) and the modified profile (blue) imported into the cathode, for the 22 mA and 25% perturbation experiment at Bergoz.

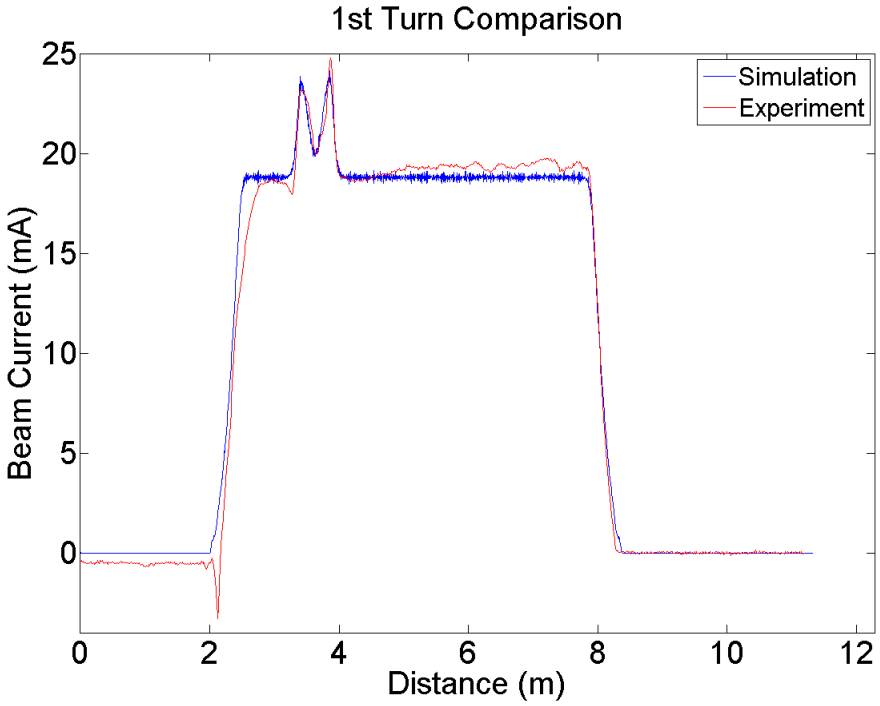

Fig. 5.5 (a): Beam current comparison between experiment (red) and simulation (blue) for the 1st turn at wall current monitor (RC10).

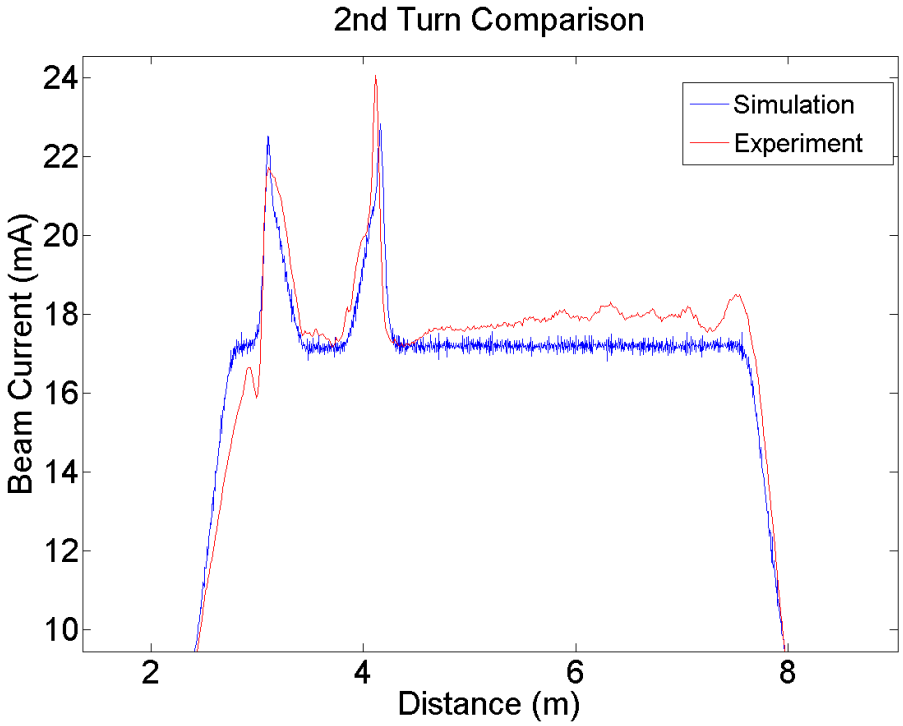

Fig. 5.5 (b): Beam current comparison between experiment (red) and simulation (blue) for the 2nd turn at wall current monitor (RC10).

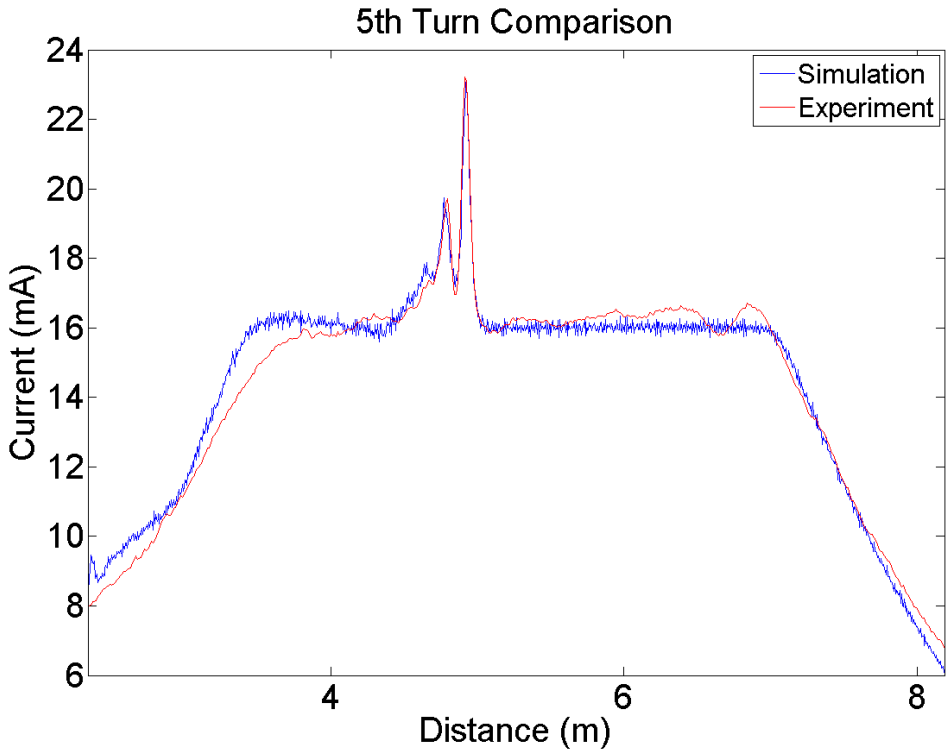

Fig. 5.5 (c): Beam current comparison between experiment (red) and simulation (blue) for the 8th turn at wall current monitor (RC10).

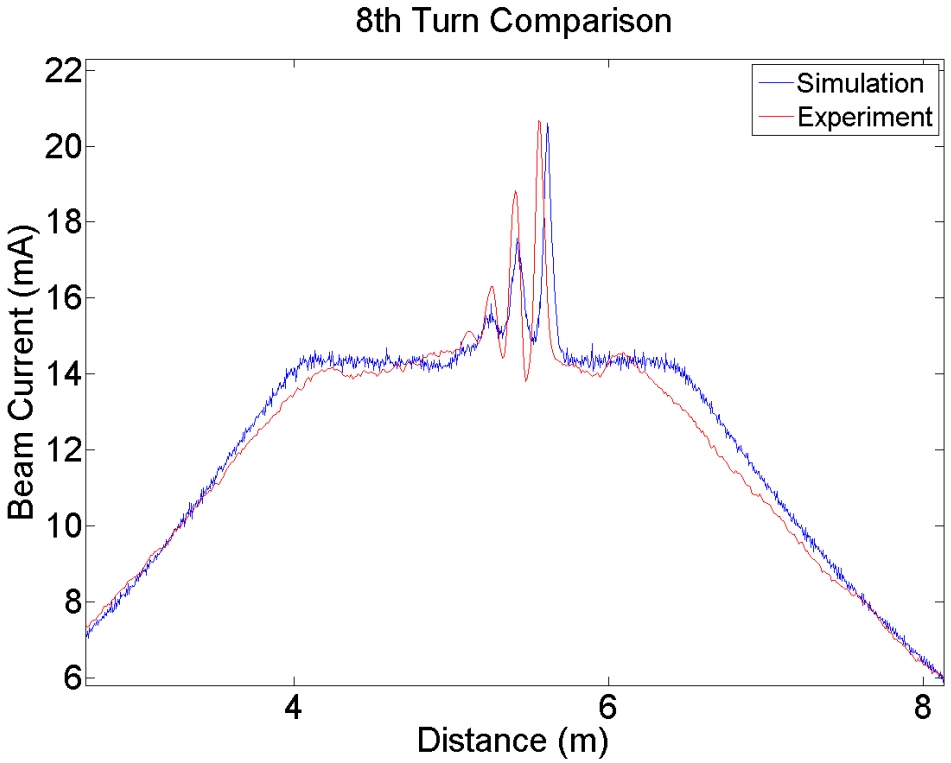

Fig. 5.5 (d): Beam current comparison between experiment (red) and simulation (blue) for the 8th turn at wall current monitor (RC10).

The agreement is not perfect and it depends on several aspects. First, the initial beam could not be ideally rectangular due to a response time at the thermionic dispenser, which results in a little discrepancy on the edge erosion, as shown in Fig. 5.5 (c). Secondly, the initial perturbation pulse is not necessarily Gaussian, and the profile difference may lead to a slight disagreement on the amplitude and width of the sub-pulses in the soliton wave train. Thirdly, the beam loss affects the longitudinal dynamics a lot, which we assume to be uniform in simulation but might not be the case in experiment, especially right after the injection due to the initial beam mismatch; In addition, there are also parameters like beam radius and emittance that we made a reasonable guess based on the experimental data taken at different chambers of the alternating-gradient ring, while we assume uniform focusing in simulation. Despite all those factors above, the overall agreement between simulation and experiment is reasonable.

For better guidance in future simulations, a table describing the beam variables' sensitivity to longitudinal dynamics is shown in Table 5.1.

Table 5.1 Variable sensitivity to beam dynamics in WARP

Variables	Sensitive or not	Affect
Beam current	Yes	erosion rate, soliton speed
Average Beam radius	Yes	erosion rate, soliton speed
Perturbation shape	Yes	soliton speed, wave train form
Emittance	No	N/A
Long. Thermal Spread	No	numerical stability
Env. radi as function of dist.	No	N/A

5.2. Soliton Propagation in Same Direction

As mentioned in Sec. 4.5, we want to investigate solitons interaction with same propagation direction. In this circumstance, the relative velocity between two soliton pulses is small ($\Delta v \sim 1e5$ m/s) and there is much longer interaction period compared with two solitons propagating face-to-face ($\Delta v \sim 2e6$ m/s). We can fully observe the beam amplitude when one soliton interacts with another. Nonlinear waves do not follow linear superposition [57], the overlap of two waves could lead to a total amplitude which is even less than one single pulse before the interaction. Fig. 5.6 demonstrates this nonlinear process theoretically. The two pulses are solutions of KdV equation.

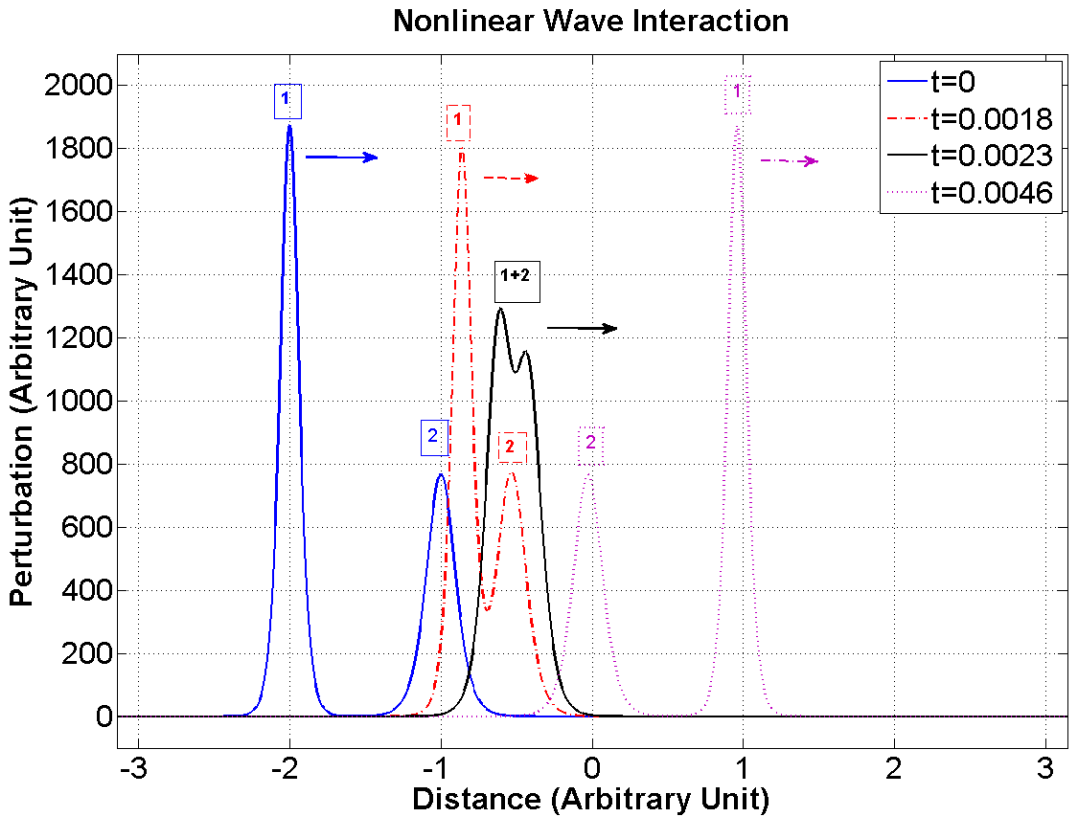

Fig. 5.6: Nonlinear wave interaction process at different time instants. The combination of the two pulses has smaller amplitude than pulse # 1 alone.

To show this nonlinear wave property in simulation, the thermionic beam bunch length is set to be unlimited so that the perturbation doesn't step off the beam edge. The ring circumference is set as 46.05 m.

The simulation result is shown in Fig.5.7. As can be seen, two different initial perturbations are introduced, with the stronger pulse in the back. Both perturbations steepen and develop into a soliton wave train. The 1st sub pulses of each wave trains are marked as "1" (for the stronger one) and "2" (for the weaker one). Pulse 1 catches up with 2 in the 26th turn and emerges from the interaction in 31st turn. Each plot is moved upward by 15mA for better comparison. The other wave train without marks is the slow wave train, which is ignored.

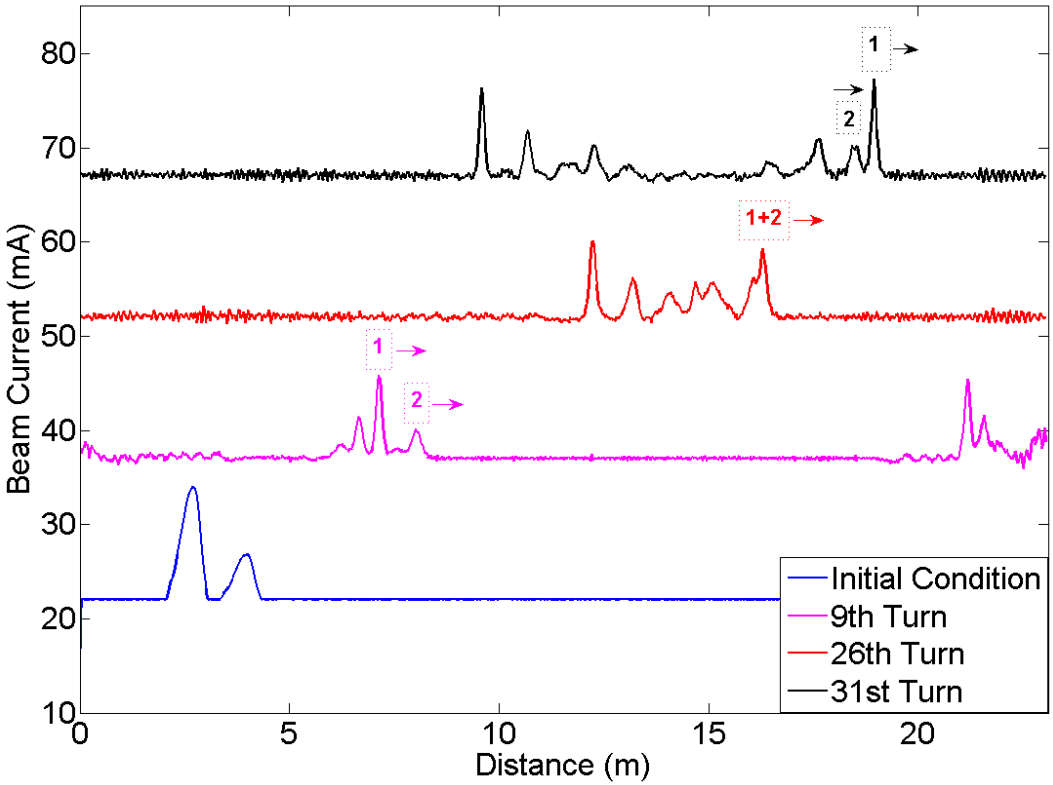

Fig. 5.7: Simulation for two large perturbations propagating in same direction.

In Fig. 5.8, we extract the data for the fast wave trains and plot them at different turns on the current level. Both the two perturbation and single perturbation cases are plotted. The single perturbation plot is moved down ward by 15 mA for better comparison. At turn 15 (black), the sum of pulse #1 and #2 can be observed, which appears to be a smaller pulse than # 1 alone. Fig. 5.9 overlaps the two plots on the same current level.

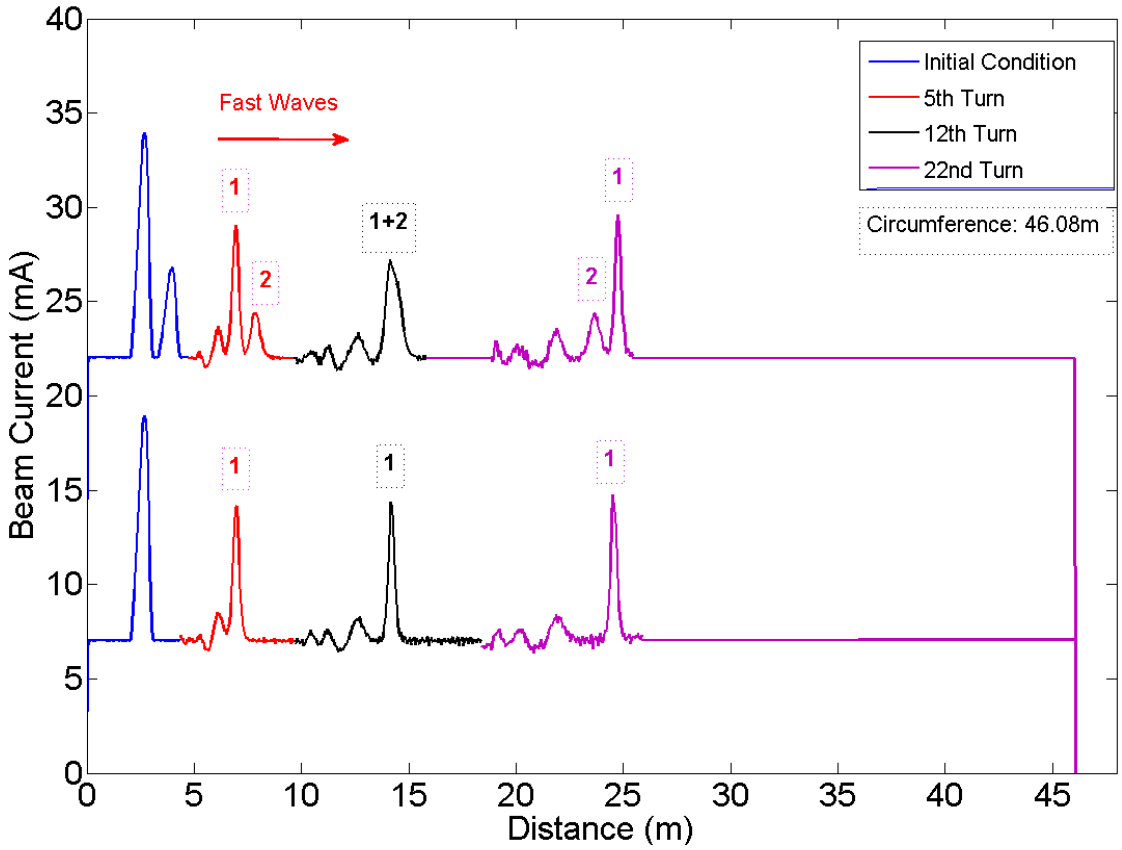

Fig. 5.8: Comparison between simulations of two perturbations and one perturbation.

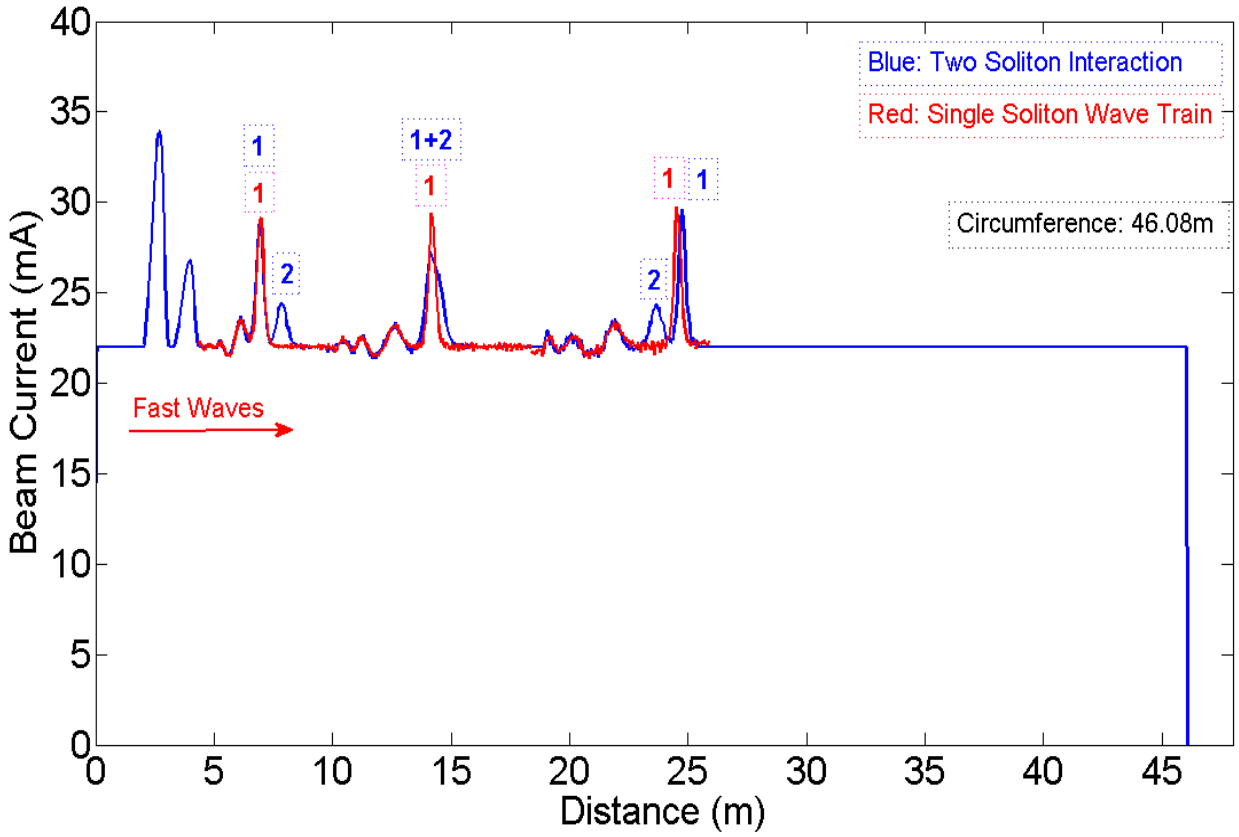

Fig. 5.9: Comparison between simulations of two perturbations and one perturbation, overlap the two results for better comparison.

5.3 Study of Soliton Pulse Spacing

The soliton wave train generated by large perturbations is a controllable, reproducible nonlinear process according to the experiments in Chapter 3. The spacing between the soliton pulses is also of particular interest. It is known that in synchrotron radiation and free electron lasers (FELs), the radiation wavelength depends on the electron bunch wavelength [58], which can be modified by wigglers and undulators. With UMER's controllable beam soliton density modulation technique, we can potentially offer an alternative of radiation source at much lower cost without the requirement of wigglers/undulators.

In this section, we investigate what determines the spacing between the peaks of the soliton wave train by simulation. The major variables are pipe radius, g-factor, sound speed and plasma frequency. We run multiple simulations to get an intuition about the soliton spacing dependence on these parameters. The results can be extrapolated to other accelerators.

For better reference, the variables are expressed as follows:

$$g = 2\ln\left(\frac{r_w}{r_b}\right); \quad \lambda = \pi r_b^2 n; \quad I = \lambda v,$$

$$\mathrm{C}_s^2 = \frac{\mathrm{qg}\lambda}{4\pi\varepsilon_0\gamma_0^5\mathrm{m}} \propto \mathrm{g}\lambda \propto g r_b^2 n \tag{5.2}$$

$$\omega_p^2 = \frac{ne^2}{\varepsilon_0 m} \propto n \tag{5.3}$$

5.3.1 Dependence on Pipe Radius

With different beam pipe radii, and all other parameters the same, a comparison between the soltion wave trains is made in Fig. 5.10-11. The initial condition is 22mA beam with 12mA perturbation. An immediate conclusion can be made that a greater pipe radius leads to wider soliton pulse spacing. It is reasonable since the dispersion effect increases with the pipe radius, therefore, the sub-pulses expand faster.

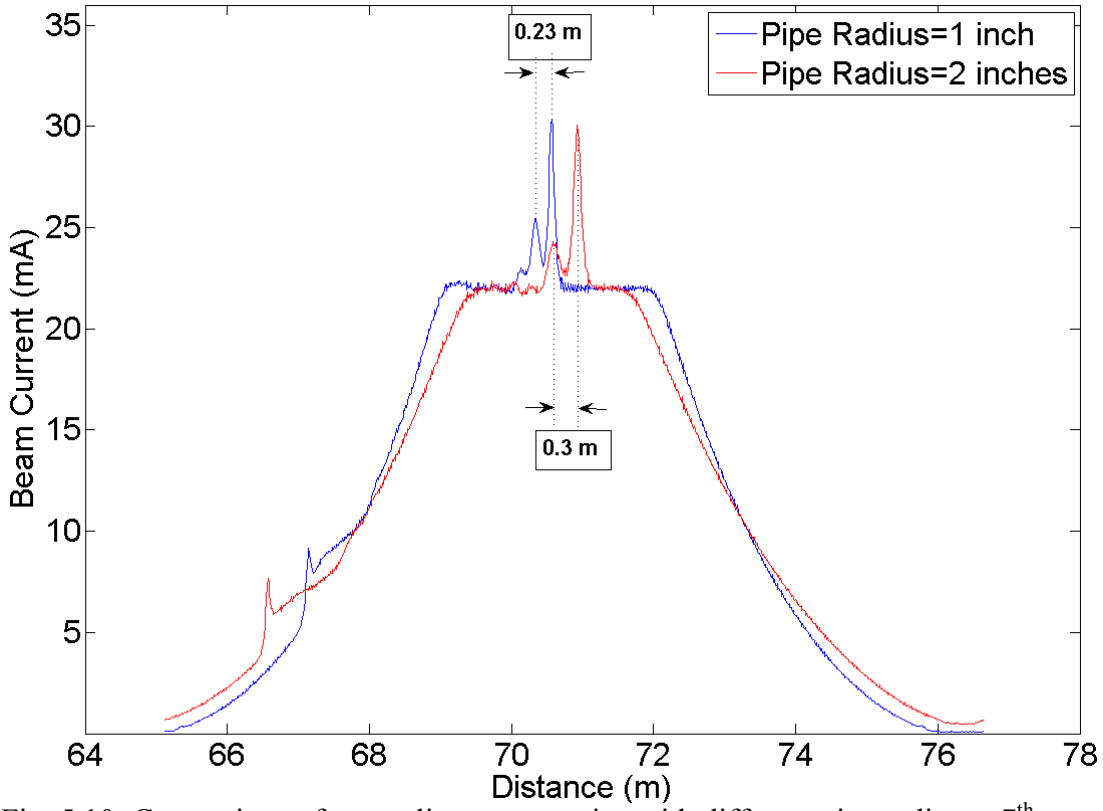

Fig. 5.10: Comparison of two soliton wave trains with different pipe radius at 7th turn.

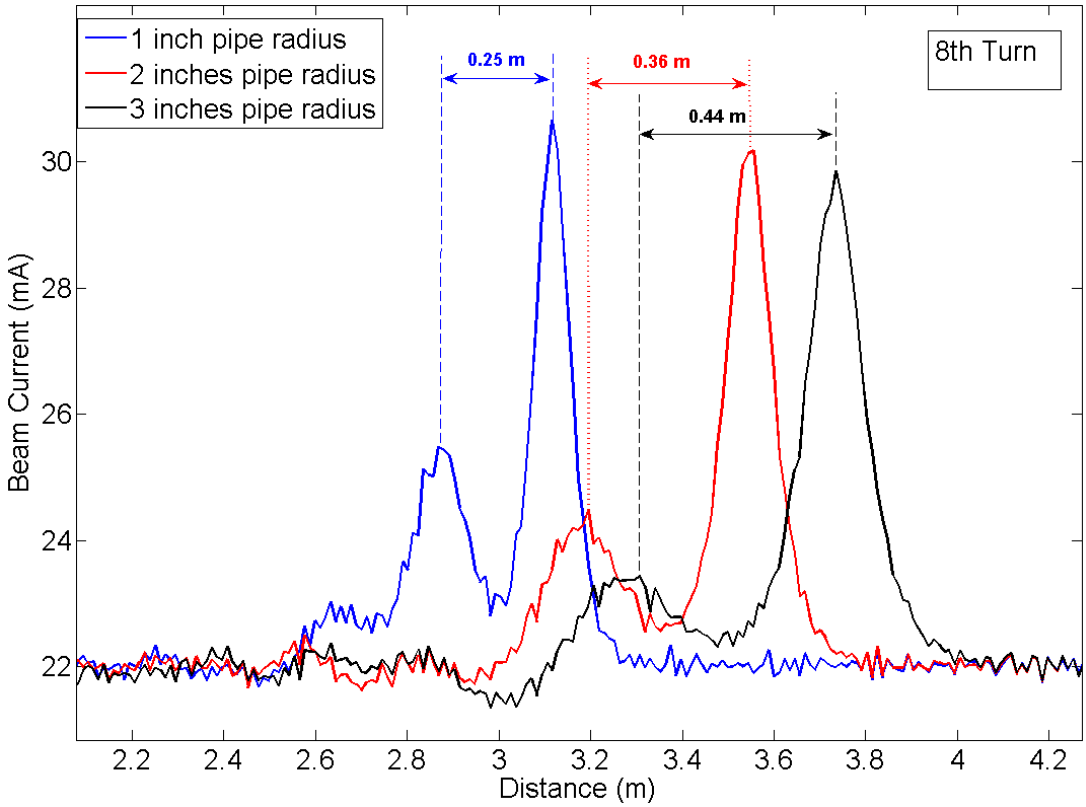

Fig. 5.11: Comparison of three soliton wave trains with different pipe radius at 8th turn.

The g-factor changes with the pipe radius, and then modifies the wave velocity Cs. By setting the beam radius and current according to Eqn (5.3-5.4), we reach the same wave velocity and align the first solitons [Fig. 5.12]. The pulses spacing increases with the g-factor. Fig. 5.13 summaries the pulse spacing frequency VS g-factor relation for two beams with different perturbation witdth.

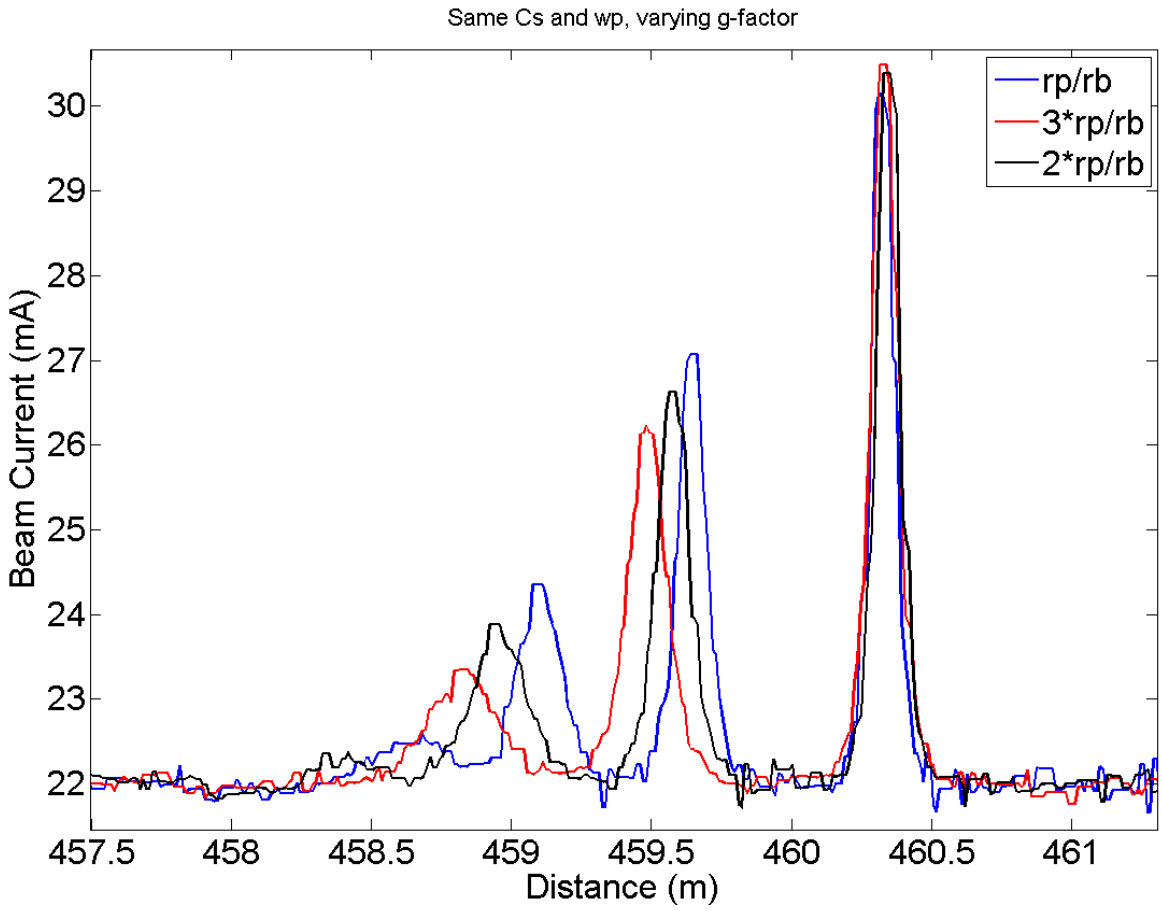

Fig. 5.12: Soliton spacing for different g-factors, whie with same wave velocity and plasma frequency. The pipe radius and beam radius are represented by rp and rb, respectively.

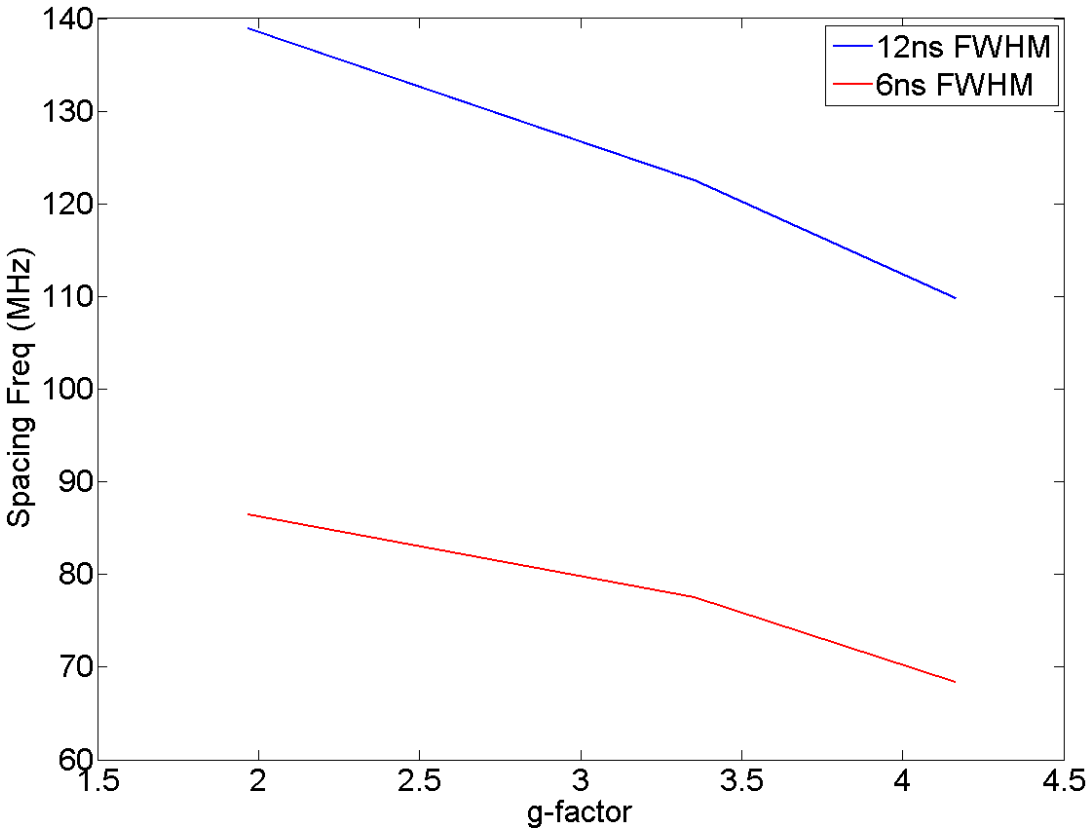

Fig. 5.13: Soliton spacing frequency VS g-factor, for 6 ns (red) and 12 ns (blue) wide perturbations at the 20th turn, with 23.05m per turn.

5.3.2 Dependence on Plasma Frequency

Tobin [22] pointed out that the soliton pulse spacing is related to the beam plasma frequency. By setting the beam with a same g-factorsand sound speed Cs, and change the plasma frequency in simulation by douling the pipe radius and beam radius:

$r_p \to 2r_p$, $r_b \to 2r_b$, then g-factor remain the same, $C_s \propto \sqrt{g\lambda}$ also stays the same;

while $n \propto \frac{1}{r_b^2} \to \frac{1}{4}n$, therefore $\omega_p \propto \sqrt{n} \to \frac{1}{2}\omega_p$

The comparison of two waves trains at different turns is shown in Fig. 5.14. A wider soliton spacing is observed for the beam with smaller plasma frequency (red). Meanwhile, it's also consistent with the spacing VS pipe radius relation. A more

sophiscated comparison is shown in Fig. 5.15, which covers a beam plasma frequency range from 10 MHz-60 MHz, for two different initial conditions.

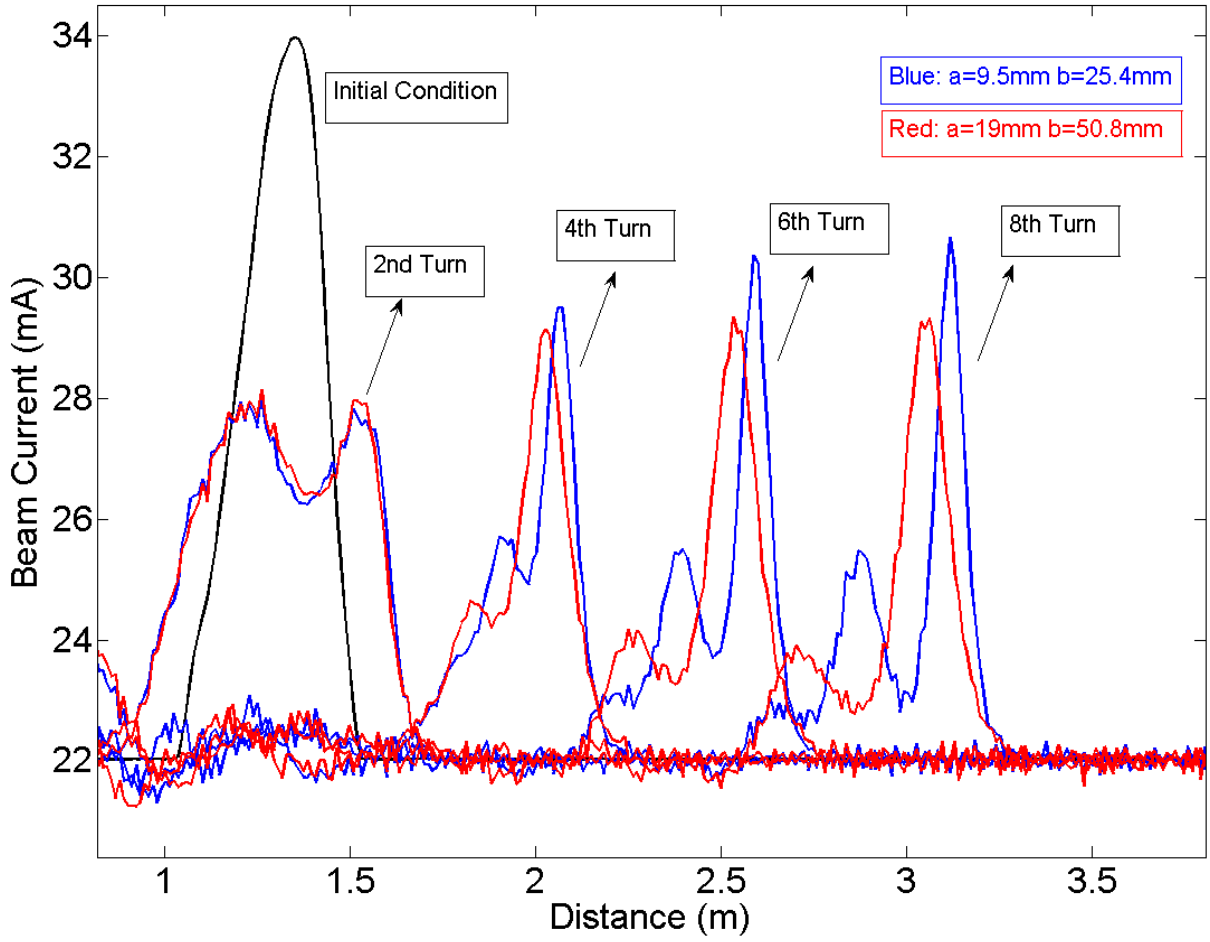

Fig. 5.14: Comparison of soliton wave train evolution for different plasma frequency, with the same wave velocity and g-factor. The pipe radius and beam radius are represented by b and a, respectively.

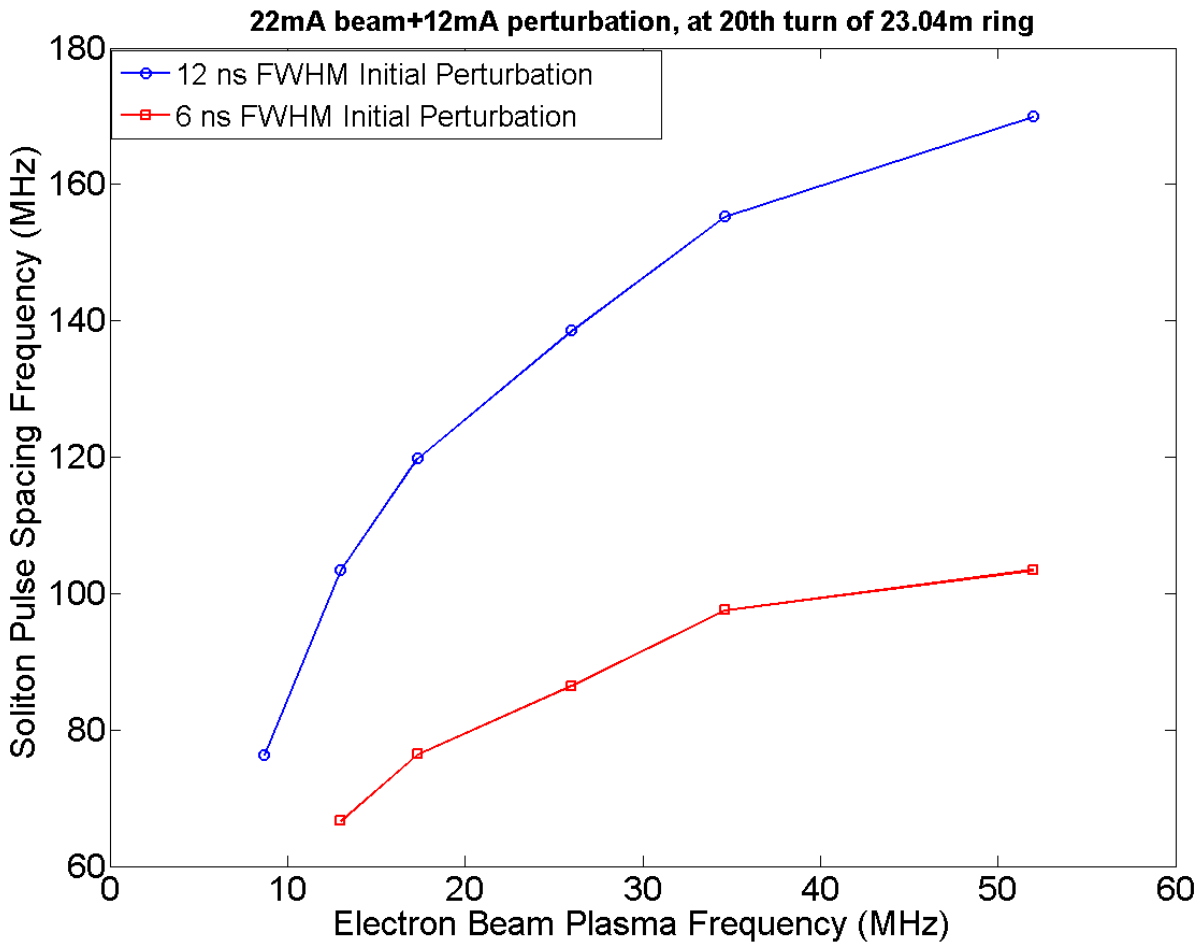

Fig. 5.15: Soliton pulse spacing frequency vs Plasma frequency for perturbations with 6ns width (red) and 12ns width (blue).

5.4 Summary

We simulated the large perturbation experiment with Particle-in-Cell code WARP, and compared with the results in Chapter 3. A good agreement between simulation and experiment is achieved. More simulation work on two soliton interaction in same propagation direction is also shown, which provides more evidence for this nonlinear process. We also investigated the soliton pulse spacing dependence on pipe radius and beam plasma frequency to explore research opportunities in new radiation sources.

Chapter 6: Conclusion and Future Plans

6.1 Summary

To sum up, I report in this dissertation a thorough study of solitons in electron beams including theory, experiment and simulation. A one-dimensional cold fluid model is applied for both linear and nonlinear perturbations. The generalized g-factor model and dispersion effect are discussed, from which the Korteweg-de Vries (KdV) equation is derived when the perturbation is nonlinear and in the long wavelength limit.

The experiment approach is by deliberately introducing large-amplitude perturbations on intense electron beams. The perturbation can be either density modulations with photoemission on the cathode, or velocity perturbations using the induction cell inside the ring. In addition to demonstrating that the observed waves are solitons, I find that, to generate solitons, the main conditions are a sufficiently high beam space charge intensity, a large perturbation amplitude (usually >20%), a long enough propagation distance (~10 times the perturbation length in the beam frame), and a relatively wide perturbation pulse (a few times of the pipe radius). An advantage of studying solitons on particle beams in UMER is the ability to generate solitons over a wide range of parameters, to control the propagation precisely and track them for a long distance. The experimental data is scaled to the normalized KdV model and good agreement is achieved. I complete the first soliton characterization by modifying beam current, perturbation strength and width.

I also simulate the nonlinear perturbation pulse evolution in a space charge dominated beam and compare with the experiments turn by turn. With the beam loss

counted and initial condition modified, the comparison discrepancy is mostly eliminated. Some experiments, which are difficult to realize due to the beam restrictions in UMER, are also simulated in Particle-in-Cell code WARP. The simulation of two soliton interaction in same propagation direction demonstrates the nonlinear wave property. The reproducible soliton wave train approach provides an alternative for a tunable, coherent radiation sources without wigglers/undulators. The soliton pulse spacing is therefore investigated, which is found dependent on the pipe radius (g-factor) and beam plasma frequency. The bunch spacing can be varied with a velocity tilt or a chicane.

Overall, the results agree reasonably well between theory, experiments and simulation, though it is not perfect. We expect the results to improve as ongoing efforts to optimize the UMER steering and beam matching result with reduced beam loss. The results are scalable to larger accelerators, provided the relative strengths of space charge to external forces are the same.

6.2 Future Plans

Worthwhile future investigations can be: systematic soliton experiments using velocity perturbation since the thermionic beam is more controllable in space charge dominated regime. Performing the soliton experiments with longitudinal focusing should lead to better agreement with theory/simulation due to less beam loss from the edge erosion [59]. Both experiments require an upgrade of the induction cell module to overcome current equipment limitations.

The beam dispersion effect study is also a worthwhile topic but active/passive q-switch equipment is required for pulse slicing since the current perturbation pulse is too wide compared with the pipe radius. The dispersion effect is directly related to the pulse

width, which affects the g-factor in the short wavelength limit, then determines the beam normalization and the dispersion term in KdV model.

Meanwhile, since the transverse beam distribution can be modified by a DMD mirror [60], we can investigate the longitudinal dynamics coupling with the transverse beam dynamics. The kinetic model (Sec. 2.3) relates the g-factor with the transverse beam distribution and thus enables us to do the theory-experiment comparison. The semi-Gaussian beam distribution in simulation can also be modified to other functions in WARP, while the beam matching and some initial settings needs to be specified, which can be complex [61].

The resistive wall effect has been studied by theory [8, 62], but never implanted in UMER ring. Mo and Beaudoin initiated experiments by installing a potentiometer in the induction cell module and observed a slight change of the beam circulation frequency. It will be worthwhile to study how the space charge waves are affected by the pipe impedance.

Finally, more theoretic/experimental/simulation work on soliton pulse spacing is definitely worthwhile and it offers a robust, reproducible and cost-effective technique for coherent, tunable radiation sources.

Appendix A: Laser Alignment Procedure

This appendix gives the key procedures for doing the laser alignment in the beam perturbation experiment using photoemission.

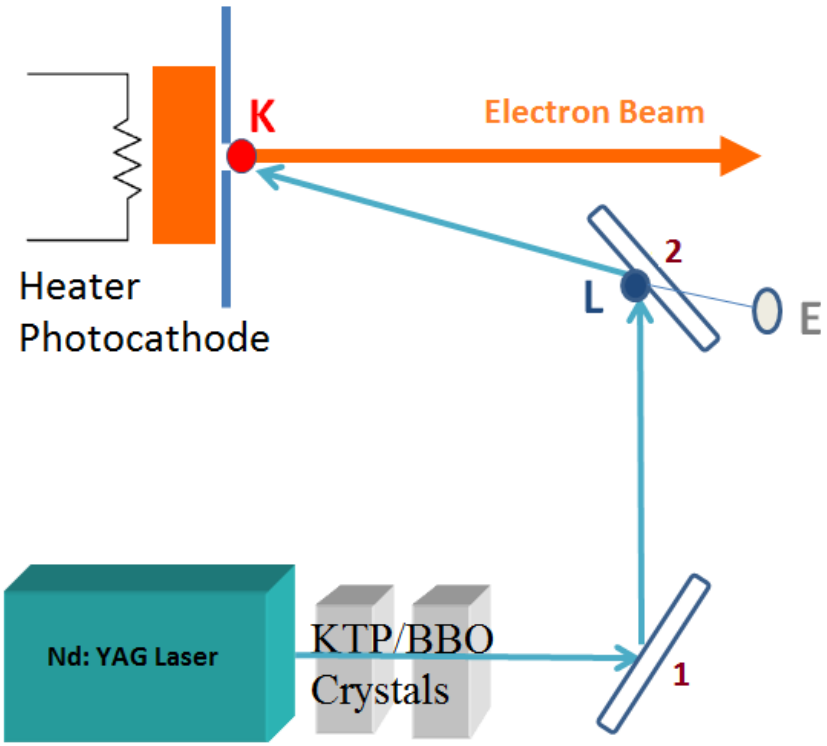

1. Adjust dielectric mirror 2, make sure the eye (E) could see the cathode (K) through the center (roughly) of the mirror;
2. Adjust dielectric mirror 1, reflect the laser to hit around the center (L) of mirror 1, and make the 2nd reflection toward the cathode(K) as close as possible by fine adjustment of mirror 1;
3. Do fine adjustment of mirror 2, make E, L, and K on the same line, which ensures that the laser hits right at the cathode.

Appendix B: Matlab Code for Heater Voltage Feedback Control

```
% File: heaterRegulate.m
function heaterRegulate()
global heater_voltage;

beam_set = 0.03; %set beam current to 30 mA
step_size =0.5;
BCerr = 0.003;  % 3 mA error
port=3035;
ip='192.168.1.3';
t=tcpip(ip,port);
fopen(t);
display('Running Heater Regulate...');

fprintf(t,['ReadVoltage,Heater']);
heater_voltage = str2num(fscanf(t));
bpm_number = 1;
GPIB_addr = 16;
[scope]=initialize_scope(GPIB_addr);
wait_period = 3;    % seconds

 while (abs(I-beam_set) > BCerr)
    [scope_data]=read_scope(bpm_number,scope);
    %plot(scope_data(:,1),0.8*scope_data(:,2));
    beam_current = 0.8*scope_data(:,2);
    I = HCpeak(beam_current) %peak current of beam bunch

    if (I<beam_set) %how to read beam_current from oscilloscope?
       display('sum')
       heater_voltage = heater_voltage+step_size
   else %  if(I>beam_set) %how to read beam_current from oscilloscope?
       display('diff')
       heater_voltage = heater_voltage-step_size
   end
   if (heater_voltage<73)
       fprintf(t,['SetVoltage,Heater,',num2str(heater_voltage)]);
   else
       display('Error setting heater voltage')
   end
   %fprintf(t,['ReadVoltage,Oscilloscope']);
   %beam_current = str2num(fscanf(t));
   pause(wait_period);
end
```

```
% File: read_scope.m
%#####################################################################
% Returns scope data at given bpm.
%#####################################################################
 function [scope_data]=read_scope(bpm_number,scope)

%BPM MUX Initiallization and selection
ni_mux_controller(num2str(bpm_number));

%Delay used to pause scope before it samples
pause(1)

%Retrieve sample from scope
[scope.yData1, scope.xData1, scope.yUnits1, scope.xUnits1] =
invoke(scope.waveformObj1, 'readwaveform', scope.channelObj1.name);
[scope.yData2, scope.xData2, scope.yUnits2, scope.xUnits2] =
invoke(scope.waveformObj2, 'readwaveform', scope.channelObj2.name);
[scope.yData3, scope.xData3, scope.yUnits3, scope.xUnits3] =
invoke(scope.waveformObj3, 'readwaveform', scope.channelObj3.name);
[scope.yData4, scope.xData4, scope.yUnits4, scope.xUnits4] =
invoke(scope.waveformObj4, 'readwaveform', scope.channelObj4.name);

scope_data(:,1)=transpose(scope.xData1); % these conver the data into 5 columns: t, ch1,
ch2, ch3, ch4
scope_data(:,2)=transpose(scope.yData1); % by 25,000 lines of data.
scope_data(:,3)=transpose(scope.yData2);
scope_data(:,4)=transpose(scope.yData3);
scope_data(:,5)=transpose(scope.yData4);

%Clear all variables
clear scope.yData1 scope.yData2 scope.yData3 scope.yData4 scope.xData1 scope.xData2
scope.xData3 scope.xData4
clear scope.yUnits1 scope.yUnits2 scope.yUnits3 scope.yUnits4 scope.xUnits1
scope.xUnits2 scope.xUnits3 scope.xUnits4
```

```
% File: integration_KdV.m
%Calculate peak current of the beam profile from the oscilloscope

function I=HCpeak(X)

I0=mean(X);
len=length(X);
j=0;
sum=0;

for i=1:len
   if(X(i)>I0)
      sum=sum+X(i);
      j=j+1;
   end
end

I=sum/j
```

Appendix C: Matlab Code for Integrating KdV Equation

```
% File: integration_KdV.m
% Descripton: Script to solve the gKdV eq.
% u_t + 3/2*u * u_x +1/2 *u_xxx = 0 on [-pi,pi] pseudo-spectrally by the integrating
factor method.

N = 256;
dt = .02/N^2;
x = (2*pi/N)*(-N/2:N/2-1)';

k = [0:N/2 -N/2+1:-1]';
ik3 = 0.5i*k.^3;                    %coefficient of u_xxx is 1/2

% import measured initial condition profile
u = zeros(length(x),1);
u(1:120)=xlsread('C:\Users\ycmo\Desktop\Old_D_drive\Yichao Mo\UMER
Lab\Aug_1_2011_Yichao\22mA Beam_Bergoz_25% Perturb','I2:I121');
u=500*u;

dtanim = 1e-4;
tmax = .012;

v = fft(u);

filter = true;

if filter
   v(N/4+1:3*N/4+1)=0.0;
%   v = ps_filter_cubic(v);
end

nmax = round(tmax/dt);
udata = u;
tdata = 0;
tlast = 0.0;


g = -0.75i*k;   %coefficient of u * u_x is 3/2=2*0.75

E = exp(dt*ik3/2);
E2 = E.^2;

for n = 1:nmax
```

```
    t = n * dt;

    a = g.*fft(real( ifft(     v    ) ).^2);

    if filter
       a(N/4+1:3*N/4+1)=0.0;
%      a = ps_filter_cubic(a);
    end

    b = (1./E) .* g.*fft(real( ifft(E.*(v + .5 * dt * a)) ).^2);

    if filter
       b(N/4+1:3*N/4+1)=0.0;
%      b = ps_filter_cubic(b);
    end

    c = (1./E) .*g.*fft(real( ifft(E .* (v + .5 * dt * b)) ).^2);

    if filter
       c(N/4+1:3*N/4+1)=0.0;
%      c = ps_filter_cubic(c);
    end


    d = (1./E2) .* g.*fft(real( ifft(E2.* (v + dt * c)) ).^2);

    if filter
       d(N/4+1:3*N/4+1)=0.0;
%      d = ps_filter_cubic(d);
    end

    v = v + dt * ( a + 2* (b+c) +d)/6;

    v = E2.*v;


    if t > tlast + dtanim
       u = real(ifft(v));
       udata = [udata u];
       tdata = [tdata t];
       tlast = t;
    end

end
```

```
% File: animate_kdv_real_manual.m
%
% Description: Animate the solution of the KdV equation in real space.
%

figure;

h = plot(x, udata(:,1), 'LineWidth',2);
title(sprintf(' t = %g', tdata(1)));
%xlabel('x');
xlabel('Distance',...
  'FontSize',16,...
  'FontWeight','bold');
%ylabel('u');
ylabel('Perturbation',...
  'FontSize',16,...
  'FontWeight','bold');
grid on;
xlim([-pi, pi]);
pause;
ylim([-100,2000]);
set(gca,'FontSize',16)

for n = 2:length(tdata)
    set(h,'ydata',udata(:,n));
    title(sprintf(' t = %g', tdata(n)), 'FontSize',16);
    drawnow;
    pause;
end
```

Appendix D: WARP Code for Soliton Simulation

```
comment  =  """ Soliton Train - 22+11 mA """
from warp import *         # --- import warp
from lwplots import *      # --- import laboratory frame window plots
from  monitor import *     # --- import ability to change run at execution
import string

# createmonitor(passwd="mo$job", port = 50008) # --- used for real time monitor
setup(runcomments=comment, cgmlog=0)

beam_curr     = 0.022
pert_curr       = 0.011


top.ekin         = 10000      # beam energy in volts
top.ibeam       = 0.033     # not actually used except fort matching
top.a0           = 0.0095635933729712099  # matched value for dedr at 22mA+11mA
top.b0          = top.a0
#top.dedr      = -271976.137 # caculated value for tune=6.67
top.dedr        = -115576.36079661094
top.emit        = 35.0e-06
top.ap0         =  0.
top.bp0         =  0.
top.zion        =  1.0e0             # use positive electrons for simplicity
top.aion        =  top.emass/top.amu  # electron mass
top.lrelativ    =  false             # nonrelativistic (in beam frame.)
w3d.xmmax       =  0.0254            # System size in x (actually r)
w3d.ymmax       =  w3d.xmmax
top.rwall       =  w3d.xmmax         # Pipe radius
w3d.solvergeom =  w3d.RZgeom         # Set solver to R-Z gemetry

#  --- calculate beam velocity to set length use same algorithm as in code
if (top.lrelativ):
   kk           = top.jperev*top.ekin/(top.aion*top.amu*top.clight**2)
   gg           =  1.e0 + kk
   v_beam       =  clight * sqrt((2*kk+kk**2)/gg**2)
else:
   v_beam       =  sqrt( (2.e0*top.ekin*top.jperev/top.aion)/top.amu )

# --- Calculate beam length for a 100ns beam

beamlen         =  100e-09*v_beam
###############################################################################
#####
```

```
# --- Use envelope integrator to calculate the matched solution.
# --- Set dedr, the uniform focusing electric field (in the Larmor frame)
# --- for a matched beam

top.tunelen    =  2*beamlen
env.zl         =  -0.0
env.zu         =  3.0*beamlen
env.dzenv      =  0.001

derivqty()

package("env")
generate()
step()


#winon()                # --- turns on plot window when running interaticely

plg(env.aenv,env.zenv)

#raise()
fma()

#top.dedr=top.dedr*(1+3.*env.deltaa/top.a0);top.dedr;
#top.a0=top.a0*(1+0.5*env.deltaa/top.a0);top.b0=top.a0;top.a0;
#generate();step();fma();plg(env.aenv,env.zenv)


###############################################################################

#top.dt         =  0.1/v_beam    # Set timestep to beam propagating 1 cm
top.dt         =  1*ns          # Round number convenient for analysis
w3d.zmmax      =  11.52     # Set max in z
w3d.zmmin      =  0.            # Set min in z
top.zimin      =  0 #2.62           # Left edge of beam
top.zimax      =  11.52 #8.26     # Right edge of beam (Set to whole system

w3d.nx         =  64          # no of cells in R
w3d.ny         =  1           # note that y direction is not used.
w3d.nz         =  2048        # no of cells in z

#setup for vzbar vs z plot
top.nzmmnt     =  w3d.nz
top.zmmntmax   =  w3d.zmmax
top.zmmntmin   =  w3d.zmmin
```

```
#  --- Set parameters for loading Particles

top.npmax      =  4000000    # Number of particles in the simulation
w3d.distrbtn   =  "semigauss"
w3d.ldprfile   =  "polar"
w3d.vtrandom   =  "pseudo"
w3d.vzrandom   =  "pseudo"

# --- Longitudinal thermal spread.
top.vthz = 0.5e05              # This number is a guess

# --- this section used only when beam length is less than system length
#w3d.cigarld=1
#w3d.distr_l = "gaussian"
#top.straight = 0.95


#  --- Set input current waveform (importing data)- code will automatically load beam in
z


ff = open("initialcondition.csv",'r')
text = ff.readlines()
ff.close()

length_=2048

current = []   #Bergoz coil Current.

no_lines = 0

for line in text:
  no_lines = no_lines + 1
  items = string.split(line, ",")
  current.append(float(items[0]))

current = array(current)


w3d.nzdist = length_
gchange("InPart3d")
w3d.zdist  = current



# --- Set boundary conditions on particles and fields
```

```
top.pbound0    = periodic
top.pboundnz   = periodic
top.pboundxy   = absorb
w3d.bound0     = periodic
w3d.boundnz    = periodic

top.nhist = 1
top.iflabwn  = 1
top.itlabwn  = 1
top.nlabwn   = 1
top.zlw      = 12.67 #0.5*w3d.zmmax
print(top.zlw)
#top.lgridqnt = 1

package("w3d")
generate()


pzcurr()               # --- plot initial beam-frame current
fma()
#savetxt('initial.dat', (top.curr[:,0]))

#plg(top.vzbarz[:,0],top.zmntmesh)
#fma()

##STOP SIMULATION HERE IF YOU WANT TO TEST INITIAL LOADING
#kjsdkjskdjk


iiimax  = 8


#  --- Set up array to hold output currents and zmesh

currents = zeros((w3d.nz+1,iiimax+1),'d')
meshes   = zeros((w3d.nz+1,iiimax+1),'d')



#ppzx(color='density',chopped=0.1)
#fma()   # moved before the main loop, after the envelope radius setting

jjjwcm  = 7.67/(top.dt*top.vbeam)-1
jjjmax  = w3d.zmmax/(top.dt*top.vbeam)-1
```

```
sw_save = top.pgroup.sw[0]
sw0=0.9   #right out of Bergoz, a lot of loss due to mismatch?!
sw1=0.838 #1st turn at RC10
sw2=0.7773 #2nd turn at RC10
sw3=0.7091 #6th turn at RC10
sw4=0.6727 #7th turn at RC10
sw5=0.65 #8nd turn at RC10

t0=0.24/v_beam
t1=(7.67+0.64)/v_beam
t2=(19.19+0.64)/v_beam
t3=(65.27+0.64)/v_beam
t4=(76.79+0.64)/v_beam
t5=(88.31+0.64)/v_beam


iii=0

currents[:,iii] = top.curr[:,0]
meshes[:,iii]  = top.zlmesh[:]+top.zbeam

top.ncolor = 10           # 10 colors in the phase space plots


#  --- Simple program to put smoothing into field calculation
def update_bndrz():
   g = frz.basegrid
   f=g.phi
#  --- Hardwire in periodic
#   if g.izlbnd==dirichlet:f[:,0]=2.*f[:,1]-f[:,2]
#   if g.izlbnd==neumann:f[:,0]=f[:,2]
#   if g.izlbnd==periodic:f[:,0]=f[:,-2]
   f[:,0]=f[:,-2]
#   if g.izrbnd==dirichlet:f[:,-1]=2.*f[:,-2]-f[:,-3]
#   if g.izrbnd==neumann:f[:,-1]=f[:,-3]
   f[:,-1]=f[:,1]
#   if g.izrbnd==periodic:f[:,-1]=f[:,1]
# w3d.phi[:,0]=w3d.phi[:,-2]
# w3d.phi[:,-1]=w3d.phi[:,1]

def smoothz():
   s=0.5
   n=3
   ff = frz.basegrid.phi
   for i in range(n):
      ff[:,1:-1] = s*ff[:,1:-1]+(1.-0.5)*s*(ff[:,:-2]+ff[:,2:])
```

```
# w3d.phi[:,1:-1] = s*w3d.phi[:,1:-1]+(1.-0.5)*s*(w3d.phi[:,:-2]+w3d.phi[:,2:])
    update_bndrz()

#  --- force use of phi to calculate fields so that smoothing works
frz.l_get_fields_on_grid=false

installafterfs(smoothz)


#  ---  Set initial envelope radius (not uniform due to the perturbation)

jj=0

while jj < top.npmax-1:
      a=(top.pgroup.zp[jj]-top.zimin)/((top.zimax-top.zimin)/length_)
      top.pgroup.xp[jj] = top.pgroup.xp[jj] * sqrt(w3d.zdist[a]/beam_curr)
      top.pgroup.yp[jj] = top.pgroup.xp[jj]
      jj=jj+1

ppzx(color='density',chopped=0.1)
fma()




# --- Main Loop

while iii < iiimax :
  iii = iii+1
  jjj = 0
  if iii == 1:
    while jjj < jjjwcm :
     jjj = jjj + 1
     step()
     if 0<top.time < t0:
       top.pgroup.sw =  (1. - (1.-sw0)*top.time/t0)*sw_save
     if t0 < top.time < t1:
       top.pgroup.sw = (1. - ((1.-sw1/sw0)*(top.time-t0))/(t1-t0))*sw0*sw_save
    if top.zbeam > top.zlw: top.zlw = top.zlw + w3d.zmmax
  if iii > 1:
    while jjj < jjjmax :
     jjj = jjj + 1
     step()
     if 0<top.time < t0:
       top.pgroup.sw = (1. - (1.-sw0)*top.time/t0)*sw_save
```

```
      if t0 < top.time < t1:
        top.pgroup.sw = (1. - ((1.-sw1/sw0)*(top.time-t0))/(t1-t0))*sw0*sw_save
      if t1 < top.time < t2:
        top.pgroup.sw = (1. - ((1.-sw2/sw1)*(top.time-t1))/(t2-t1))*sw1*sw_save
      if t2 < top.time < t3:
        top.pgroup.sw = (1. - ((1.-sw3/sw2)*(top.time-t2))/(t3-t2))*sw2*sw_save
      if t3 < top.time < t4:
        top.pgroup.sw = (1. - ((1.-sw4/sw3)*(top.time-t3))/(t4-t3))*sw3*sw_save
      if t4 < top.time < t5:
        top.pgroup.sw = (1. - ((1.-sw5/sw4)*(top.time-t4))/(t5-t4))*sw4*sw_save
      if top.zbeam > top.zlw: top.zlw = top.zlw + w3d.zmmax

  fma()
  pzcurr()
  fma()
  pzcurr()
  limits(top.zbeam+0.66*beamlen,top.zbeam+1.33*beamlen,'e','e')
  fma()
  ppzx(color='density',chopped=0.1)  # , contours=10)   # Uncomment if you get only 5
colors
  fma()
  ppzvz(color='density',chopped=0.1)
  currents[:,iii] = top.curr[:,0]
  meshes[:,iii]  = top.zlmesh[:]+top.zbeam
  fma()
  pcurrlw(ilw=0)
fma()

# --- Text output
runid = arraytostr(top.runid)
ff1 = open(runid+".currout.txt", "w")
ff2 = open(runid+".meshout.txt", "w")
for iii in range(0, currents.shape[0]):
    for jjj in range(0, currents.shape[1]):
        print >> ff1, '%8.6f'%(currents[iii, jjj],),
        print >> ff2, '%8.6f'%(meshes[iii, jjj],),
    print >> ff1
    print >> ff2
ff1.close()
ff2.close()

savetxt('currlw.dat', (top.currlw))
savetxt('timelw.dat', (top.timelw))
savetxt('vzbarz.dat', (top.vzbarz))
```

Bibliography

[1] L. Evans. The Large Hadron Collider. *New J. Phys*, 9:335, 2007.

[2] R. R. Wilson. The Tevatron. *Phys. Today*, 10:23–30, 1977.

[3] P. Emma. The Stanford Linear Collider. *Proc. of PAC95*, **1**, 1995: 609-610.

[4] H. Winick. Fourth Generation Light Source. *Proc. of SLAC-PUB*, 1997: 37-41.

[5] T. C. Marshall, *Free Electron Laser* (Macmillan Publishing Co., New York, 1985).

[6] J. Wei et al., *Proc. of. IPAC*, Portland, OR, 2003, p. 571.

[7] T. Shaftan, and Z. Huang, Phys. Rev. ST-AB, 7, 080702 (2004).

[8] J.G. Wang, M. Reiser, W.M. Guo, and D.X. Wang, *Part. Accel.* **37-38**, 181 (1991)

[9] J. G. Wang, D. X. Wang, and M. Reiser, Phys. Rev. Lett. **71**, 1836 (1993).

[10] K. Tian, R. A. Kishek, I. Haber, M. Reiser, and P. G. O'Shea, Phys. Rev. ST-AB,13, 034201 (2010).

[11] J. Bisognano, I. Haber, L. Smith, and A. Sternlieb, IEEE Trans. on Nucl. Sci. 28, 2513 (1981).

[12] R. Davidson, Phys. Rev. ST-AB, **7**, 054402 (2004).

[13] S. Ramo, Physical Review, **56**, 276, (1939).

[14] W. C. Hahn, Gen. Elec. Rev., **42**, 258, (1939).

[15] C. Birdsall and J. Whinnery, Journal of Applied Physics, Vol. **24**, 3, 314, (1953).

[16] D.X. Wang, J.G. Wang, and M. Reiser, Phys. Rev. Lett., **73**, 66, (1994).

[17] H. Suk, J. G. Wang, and M. Reiser, Phys. Plasmas **3** (2), 669 (1995)

[18] Y. Zou, Ph.D. Dissertation, University of Maryland, (2000).

[19] K. Tian, Ph.D. Dissertation, University of Maryland, (2008).

[20] Y. Huo, Masters Thesis, University of Maryland, (2004).

[21] J.R. Harris, J.G. Neumann and P.G. O'Shea, Journal of Applied Physics, 99, 093306, (2006).

[22] J. C. T. Thangaraj, Ph.D. Dissertation, University of Maryland, (2009).

[23] B. Beaudoin, Ph.D. Dissertation, University of Maryland, (2011).

[24] Scott Russell, J., *"Report on waves"*. Fourteenth meeting of the British Association for the Advancement of Science. (1844)

[25] N. J. Zabusky and M. D. Kruskal, Phys. Rev. Lett. **15**, 240 (1993).

[26] H. Ikezi, R. J. Taylor and D. R. Baker, Phys. Rev. Lett., **25**,11-14 (1970)

[27] M. Reiser, *Theory and Design of Charged Particle Beams* 2nd Ed. (Wiley-VCH Inc., Weinheim Germany, 2008).

[28] J. Bisognano, *"Solitons and Particle Beams"*. High-Brightness Beams for Advanced Accelerator Application, Particles and Fields **47**, AIP, p.42 (1992)

[29] H. Suk, J. G. Wang, and M. Reiser, Phys. Plasmas **3** (2), 669 (1995)

[30] R. Davidson, E. Startsev, and Hong Qin, in *Proc. PAC07, Albuquerque, New Mexico*, p. 4291.

[31] T.P. Hughes, E. Ott, Physics of Fluids, vol. **23**, Nov. 1980, p. 2265-2269.

[32] H. Schamel, Phys. Rev. Let. **79**, 2811 (1997)

[33] O. Boine-Frankenheim and I. Hofmann, Phys. Rev. ST-AB, **3**, 104202 (2000).

[34] M. Blaskiewicz, and J. Wei, Phys. Rev. ST-AB, **7**, 044402 (2004).

[35] S. Koscielniak, S. Hancock and M. Lindroos, Phys. Rev. ST-AB, **4**, 044201 (2004).

[36] Y. C. Mo, R. A. Kishek, D. Feldman, I. Haber, B. Beaudoin, P. G. O'Shea, and J. C. T. Thangaraj, Phys. Rev. Lett. **110**, 084802 (2013).

[37] J. G.Wang, H. Suk, D. X.Wang, and M. Reiser, Phys. Rev. Lett. **72**, 2029 (1994).

[38] R. Davidson and E. Startsev, Phys. Rev. ST-AB, **7**, 024401 (2004).

[39] P. S. Lomdahl, S. P. Layne and I. J. Bigio, Los Alamos Sci. **10**, 2 (1984).

[40] R.C. Davidson, *Methods in Nonlinear Plasma Theory* (Academic Press, New York, 1972)

[41] J. Harris, Ph.D. Dissertation, University of Maryland, (2005).

[42] Technical Note, UMER-2011-0215-YM

[43] Tech. Note: UMER-2012-1214-YM, BB

[44] User Manual of Nd:YAG Laser, Minitlite and PIV, Continuum.

[45] B. Beaudoin, I. Haber, R.A. Kishek, S. Bernal, T. Koeth, D. Sutter, P.G. O'Shea, and M. Reiser, Physics of Plasmas, 013104, (2011).

[46] ENEE 686 Class Notes, Kishek, 2011.

[47] Texas Instruments Inc. DMD Discovery 1100 Controller Board and Starter Kit, 2005.

[48] H. Zhang, M.S. Thesis, University of Maryland, (2011)

[49] Hao Zhang, private communication, 2012.

[50] P. G. Drazin and R. S. Johnson*, Solitons: An Introduction* (Cambridge University Press, Cambridge, England, 1989), 2nd ed.

[51] Technical Note, UMER-2013-0107-BBHZTK.

[52] Kamal Rezaei, private communication, 2013.

[53] Hao Zhang, private communication, 2013.

[54] D.P. Grote, A. Friedman, I. Haber, S. Yu, Fusion Eng. Des 32-33, 193-200, (1996).

[55] Technical note, UMER-2012-0112-IH, BB, TPK

[56] Technical note, UMER-2012-0712-YM

[57] E. Hecht, *Optics*, 4th Ed. (Addison Wesley, San Francisco, 2002)

[58] C. A. Brau, *Modern Problems in Classical Electrodynamics* (Oxford University Press, New York, 2004)

[59] B. Beaudoin, S. Bernal, K. Fiuza, I. Haber, R.A. Kishek, T. Koeth, M. Reiser, D. Sutter, P.G. O'Shea, in *Proc. PAC11, New York, New York*, p. 85.

[60] H. Zhang, R. Fiorito, A. Shkvarunets, R. Kishek, C. Welsch. Phys. Rev. ST-AB, **15**, 072803 (2012).

[61] Irving Haber, private communication, 2013.

[62] J.G. Wang, M. Raiser, Phys. Fluids B, **5**, 2286 (1993).